UNIVERSITAT POLITÈCNICA DE CATALUNYA
BARCELONATECH
Escola Superior d'Enginyeries Industrial,
Aeroespacial i Audiovisual de Terrassa

STUDY: AN ASSESSMENT ON THE REQUIREMENTS FOR DEEP SPACE OPTICAL COMMUNICATIONS

MASTER THESIS

MSc IN AEROSPACE ENGINEERING

SCHOOL OF INDUSTRIAL, AEROSPACE AND AUDIOVISUAL

ENGINEERING OF TERRASSA

21st June 2021

Submitted by:
Marc Casanovas Ventura

Directed by:
Jordi Gutiérrez Cabello

Co-Director:
Manel Soria Guerrero

Declaration of Honor

I declare that,

- The work in this Master Thesis is completely my own work,
- No part of this Master Thesis is taken from other people's work without giving them credit,
- All references have been clearly cited,
- I am authorised to make use of the data sources from open sources I am providing in this document.

I understand that an infringement of this declaration leaves me subject to the foreseen disciplinary actions by The Universitat Politècnica de Catalunya.

Marc Casanovas Ventura		**21st June 2021**
Student Name	*Signature*	*Date*

Title of the Thesis: **Study: An assessment on the requirements for deep space optical communications**

Foremost, I would like to express my sincere gratitude to my advisor professor Jordi Gutiérrez for the continuous support, enthusiasm and immense knowledge, especially for introducing me to the passionate field of astronomical observation.

I would like to thank Manel Soria for his support and guidance at the beginning of the thesis and above all for introducing me to SPICE, an indispensable tool to discover deeply the solar system particularities.

Special thanks to Paula Betriu for sharing her enormous work which has allowed me to unravel, more easily, the vast documentation of SPICE.

Finally, to my dear family and friends for your support in this unfortunate time we have had to live through.

Contents

List of Figures

List of Tables

Glossary

Abbreviations

ADCS	Attitude Determination Control System
APD	Avalanche Photo-Diode
AU	Astronomic Unit
BER	Bit Error Rate
BWG	Beam Wave Guide
CCSDS	Consultative Committee for Space Data Systems
COTS	Commercial Off-The-Shelf
DLR	Deutsches Zentrum fur Luft - und Raumfahrt
DOT	Deep space Optical Terminals
DSOC	Deep Space Optical Communications
DSN	Deep Space Network
EDRS	European Data Relay System
ESA	European Space Agency
FLT	Flight Laser Transceiver
FOV	Field Of View
FY	Fiscal Year
FSO	Free space optical
GEO	Geostationary Earth Orbit
HAP	High Altitude platforms
HD	High Definition
IRT	Index of Refraction Turbulence
ITU	International Telecommunications Union
JAXA	Japan Aerospace Exploration Agency
JPL	Jet Propulsion Laboratory
KSAT	Kongsberg Satellite Services
LDOS	Linear Distributed Optical Subnet
LEO	Low Earth Orbit
LLCD	Lunar Laser Communication Demonstration
LN	Log Normal
LPD	Low Probability of Detection
LPI	Low Probability of Intercept
MAVEN	Mars Atmospheric & Volatile EvolutioN
MLCD	Mars Laser Communication Demonstrator
NEN	MCLD Lasercom Terminal
MICE	SPICE with MATLAB
MODIS	Moderate Resolution Imaging Spectroradiometer
MRN	Mars Relay Network
MRO	Mars Reconnaissance orbiter
NAIF	Navigation & Ancilliary inforamtion facility

NASA National Aeronautics and Space Administration
NBF Narrow Band Filter
NEN Near Earth Network
ODSN Optical Deep Space Network
OGS Optical Ground Station
OMA OptoMechanical Assembly
OOK On Off Keying modulation
PAT Pointing Acquisition and Tracking
PDF Probability Density Function
PIF Point Induced Fade
PPM Pulse Position Modulation
RMS Root Mean Square
Rx Receiver
S/C Spacecraft Navigation
SCaN Space Communications and Navigation
SEP Solar-Earth-Probe
SPE Solar-Probe-Earth
SDS Scientific DataSets
SNR Signal-to-Noise Ratio
SOMD Space Operations Mission Directorate
SPICE Spacecraft Planet Instrument C-matrix Events
SSC Swedish Space Corporation
SWaP Size, weight, and Power
TEM Transverse Electromagnetic Mode
TBL To Be Launched
TDMM Two Decades Mean Matrix
TMF Table Mountain Facility
TRL Technology Readiness Levels
TGO Trace Gas Orbiter
Tx Transmitter
UAV Unmanned aerial vehicles
UHF Ultra-High Frequency
WFE Wafe Front Error

Symbols

a	Primary mirror radius
alb	Albedo
A_{eff}	Effective Area
b	Secondary mirror radius
B	Bandwidth
C	Cost
C_{PPM}	Capacity in PPM
C_n^2	Refractive Index Structure Parameter
d	Photo detector size
D	Diameter
D_{Rx}	Receiver diameter
D_{Tx}	Transmitter diameter
DR	Data Rate
E_λ	Energy per photon
f	Transmittance frequency
f_d	Focal length
F	Correction factor
g_R	Antenna receiver efficiency factor
g_T	Antenna transmitter efficiency factor
G_{Rx}	Receiver Gain
G_{Tx}	Transmitter Gain
G'_{Rx}	Modified Receiver Gain
G'_{Tx}	Modified Transmitter Gain
h	Altitude
h_0	Initial altitude of the transmitter/ receiver
h_p	Planck's constant
h_s	Turbulence scale height
H	Final altitude of the receiver/ transmitter
HV_{57}	Hufnagel-Valley 5-7 model
I	Irradiance
$I(\lambda)$	Irradiance from Mars incident to Earth
k	Wavenumber
L_{abs}	Absorption loss
L_{atm}	Atmospheric loss
L_{pol}	Polarization loss
L_{SR}	Strehl loss
L_{turb}	Turbulence loss
$L(\lambda)$	Sky radiance
M	Alphabet size
p_{th}	Threshold probability
P_b	Background received power
P_{min}	Minimun power

P_{Rx}	Signal power received
P_s	Minimum detectable signal power
P_{Tx}	Signal power transmitted
r	Scatter size
r_0	Fried parameter
R	Range
S	Space Loss
SR	Strehl Ratio
T	Transmittance
v_{radial}	radial velocity
v_{trans}	transverse velocity
w	rms wind speed (pseudowind)
x	dependent variable
x'	Wave front error
X	Off-axis dimensionless parameter
Z	Earth-Mars distance
α	Beamwidth to aperture ratio
α_a	Absorption coefficient (aerosols)
α_{clear_air}	Attenuation under adverse weather conditions
α_e	Extinction coefficient
α_{excess}	Attenuation under clear sky conditions
α_m	Molecular absorption coefficient
β	Near field and defocusing effects dimensionless parameter
β_a	Mie scattering coefficient
β_m	Rayleigh scattering coefficient
γ_{rx}	Obscuration ratio at the receiver
γ_{tx}	Obscuration ratio at the transmitter
δ	Critical error angle
Δf_d	Frequency Doppler shift
$\Delta\lambda_d$	Wavelength Doppler shift
$\Delta\lambda$	NBF bandwidth
η_A	Aperture illumination efficiency
η_{det}	Quantum detector efficiency
η_{RP}	Receiver pointing efficiency
$\eta_{RP}(\theta_1)$	Instantaneous pointing loss
η_{Rx}	Receiver efficiency
η^*_{Rx}	Modified receiver efficiency
η_{TP}	Transmitter pointing efficiency
η_{Tx}	Transmitter efficiency
η_λ	NBF efficiency
θ	Elevation angle
θ_0	Isoplanatic angle
θ_1	Mispointing angle
θ_{1x}	x-axis mispointing angle contribution
θ_{1y}	y-axis mispointing angle contribution

θ_{FOV}	Field of view angle
Θ	Point ahead angle
ϑ_{Tx}	Jitter (Variance in rice distribution probability function)
ϑ_x	x-axis jitter contribution
ϑ_y	y-axis jitter contribution
λ	Wavelength
λ_b	Background noise flux
λ_s	Signal flux
Λ	Aperture averaging
μ_{LD}^2	Log-normal distribution mean
ν	Mean in Rice distribution probability function
ξ	Normalised distance variable
ρ_I	Speckle size
σ	RMS Wavefront error
σ_I^2	Scintillation index (normalised irradiance variance)
σ_{lnI}^2	Variance of log-irradiance
σ_{LD}^2	Log-normal distribution variance
σ_P^2	Power scintillation index
σ_{RD}^2	Variance in Rice distribution probability function
τ_s	Slot time
φ	Zenit angle
χ_{Rx}	Bias error in pointing accuracy at the receiver
χ_{Tx}	Bias error in pointing accuracy at the transmitter
χ_x	x-axis bias error in pointing accuracy
χ_y	y-axis bias error in pointing accuracy
ω	$1/e^2$ radius Gaussian beam
Ω_{FOV}	Receiver FOV solid angle
Ω_S	Noise source solid angle

Resum

En l'última dècada, termes con el *Big data* o l'*IoT* han passat a formar part del vocabulari més quotidià, a mesura que el temps avança, cada vegada més sistemes recopilen majors quantitats de dades amb la finalitat d'oferir nous serveis o millorar-ne la qualitat, en aquest sentit, l'àmbit aeroespacial no és una excepció. Les sondes i ròvers espacials, que en el seus inicis en comunicaven amb les estacions terrenes mitjançant la banda S, han anat transitant cap a freqüències més elevades per tal de poder transmetre més d'informació per unitat de temps. Al augmentar la freqüència del sistema, s'assoleix la banda òptica, ara fa 40 anys, va ser realitzat el primer experiment demostrador, en l'àmbit aeroespacial, de comunicació per làser, l'AFTS de l'anglès Airbone Flight Test System. Des d'aleshores s'han realitzat nombrosos esforços per a demostrar que les comunicacions òptiques són possibles. Al enviar una missió d'exploració, la comunitat científica maximitza les prestacions dels aparells atenent a múltiples criteris; Per exemple, es té en compte si l'aparell en concret ha estat testejat prèviament en l'espai i quines són les probabilitats de fallada. Per això l'ús de noves tecnologies requereix d'un procés de missions demostradores fins que finalment s'acabin assentant.

La present tesis fa una recopilació de l'estat de l'art, és a dir, del coneixement adquirit durant aquestes últimes quatre dècades, a més, s'engloben tres punts principals, les infraestructures terrestres, el terminal de vol i el mètode de comunicació entre les dues parts.

En el primer punt, l'estudi es centra en explicar el paràmetres que s'han de tenir en compte a l'hora de dissenyar una xarxa de estacions òptiques terrenes a nivell internacional, d'una manera equivalent a la seva homologa en la banda RF, les xarxes DSN de la NASA o l'ESTRACK de l'ESA entre d'altres. Una de les variables més rellevants i que determina la ubicació de les estacions terrenes són les condicions atmosfèriques, per aquest motiu s'han descarregat i processat de la base de dades LAADS DAAC de la NASA un seguit d'arxius que contenen informació sobre l'atmosfera del planeta.

En segon lloc, s'ha estudiat l'equació d'enllaç d'un senyal emès en banda òptica. Cada un dels termes que la formen es presenten detallats al llarg de diversos apartats, en especial es destaquen les pèrdues d'enfosquiment en antenes tipus Cassegrain , les pèrdues d'apuntat i les degudes a l'absorció i turbulència atmosfèriques.

Finalment s'han realitzat dos estudis pràctics on es pot veure com s'han aplicat les eines matemàtiques descrites en els capítols anteriors per a missions la qual finalitat és la comunicació per làser en l'espai profund. Per aconseguir això, la biblioteca i el kit d'eines del JPL anomenats SPICE s'ha utilitzat en una missió, fictícia però realista, en un enllaç descendent Mart-Terra. Gràcies a la gran fiabilitat de SPICE, s'ha pogut obtenir totes les dades vinculades a la mecànica orbital d'una missió espacial, que han estat contrastades, en ordre de magnitud, amb una missió anomenada Psyche i DSOC el qual llançament està previst l'Agost del 2022. Apart d'exemplificar de manera didàctica els termes de l'equació d'enllaç en una missió en concreta, també s'han obtingut elements claus com la capacitat o taxa de bits , que permeten extraure conclusions immediates a favor d'aquesta tecnologia i en conseqüència contribueixen a la seva consolidació en el camp de les comunicacions en l'espai profund.

Abstract

Over the last decade, terms such as big data and IoT have become part of our everyday vocabulary, and as time goes by, more and more systems are collecting larger amounts of data in order to provide new services or improve quality, and aerospace sector is not an exception. Space probes and rovers, which originally communicated with ground stations using S-band, have moved to higher frequencies in order to be able to transmit more information per unit of time. As the frequency of the system increases, the optical band is reached, 40 years ago, the first experiment in aerospace to demonstrate laser communication, the Airbone Flight Test System (AFTS), was conducted. Numerous efforts have been made to demonstrate that optical communications are possible. When sending an exploration mission, the scientific community maximises the performance of the instruments by taking into account multiple criteria, such as whether the particular device has been previously tested in space and the likelihood of failure. Therefore, the use of new technologies requires a process of multiple demonstration missions prior to be accepted.

This thesis compiles the state of the art, i.e. the knowledge acquired over the last four decades, and covers three main points: ground infrastructures, the flight terminal and the method of communication between both systems.

In the first point, the study focuses on explaining the parameters that must be taken into account when designing an international ground station network, equivalent to its counterpart in the RF band, NASA's DSN networks or ESA's ESTRACK, among others. One of the most relevant variables that determines the location of a ground stations are the atmospheric conditions. For this reason, a series of files containing information about the planet's atmosphere has been downloaded and processed from NASA's LAADS DAAC database.

Secondly, the link equation of a signal emitted in optical band has been studied. Each of the terms that make up the equation are presented in detail in several sections, in particular the obscuration losses in Cassegrain type antennas, the pointing losses and those due to atmospheric absorption and turbulence.

Finally, two practical studies have been carried out in which it is possible to see how the mathematics described in the previous chapters have been applied to execute missions whose purpose is to communicate in deep space. To achieve this, the JPL library and toolkit called SPICE has been used in a fictitious but realistic Mars-Earth downlink mission. Thanks to the high reliability of SPICE, all the data related to the orbital mechanics of a space mission has been obtained and compared, in order of magnitude, with a mission called Psyche and DSOC, scheduled for launch in August 2022. Apart from didactically exemplifying the terms of the link equation in a specific mission, key elements such as capacity or bit rate have also been retrieved, which allow immediate conclusions to be drawn in favour of this technology and thus contribute to its consolidation in the field of deep space communications.

1 Introduction

Communications is one of the most critical activities that must be undertaken by spacecrafts. After all, if a satellite performs flawlessly its mission but is not able to convey the results, it is of little use. Modern spacecraft, and their successors in the foreseeable future, have very demanding requirements for their communication subsystems. In fact, the amount of data relayed by modern satellites is orders of magnitude larger that the amounts generated by similar-lifespan satellites of just 20 years ago.

On February, 18^{th}, 2021, operations lead Swati Mohan at mission control at NASA's Jet Propulsion Laboratory (JPL) headquarters, confirmed the *Perseverance* rover's landing. It took eleven and a half minutes to attest the touchdown owing to delays in communications caused by the huge distance between Mars and the Earth. This is an insurmountable problem due to the finite velocity of electromagnetic waves.

Mars 2020 mission provided the first ever recorded sky crane maneuver as well as two images of the crane crash which took place approximately 700 m away from the rover after dropping it. This data can be transmitted to the Earth through a direct rover-Earth link or by Mars orbiters relay, it generally takes 5 to 20 minutes for a radio signal to travel between both planets. When using orbiters, a faster data transmission is achieved, because they are much closer to *Perseverance* than the Deep Space Network (DSN) antennas on Earth. One of the three antennas *Perseverance* is equipped with, consists of an ultra-high frequency (UHF) antenna (about 400 MHz) [16] to communicate with Earth. For this system, the data rate reaches up to 2 Mbps on the rover-to-orbiter relay link. As rover vehicle is constrained by mass and power, the orbiters use their much larger antennas and powerful transmitters to relay that data on the long-distance link back to Earth.

As with *Mars* 2020, space missions are being designed with ever more data demanding planetary probes. Early NASA spacecraft telecommunication systems relied on the S-band. Nearly twenty years later, X-band frequencies were implemented. Over twenty years later, deep space communications is moving to K_a-band. The goal of this migration to higher frequencies is to increase the available bandwidth, as the maximum theoretical data rate obtainable in a noisy link is given by the Shannon-Hartley theorem:

$$DR = B \ \log_2(1 + \mathrm{SNR}) \tag{1}$$

where B is the bandwidth (in [Hz]) and SNR is the signal-to-noise ratio.

Nevertheless, should this trend continue in the near future, the radio frequency (RF) bands would not be able to tackle the highly demanding missions requirements. Then, such an amount of data generated will force space communications to make a transition to the optical spectrum band (see figure 1.1). Alternatively, highly-efficient, loss-less data compression algorithms –yet to be designed!– might be necessary. However, these same putative algorithms would further improve communications were they used with an optical communications link.

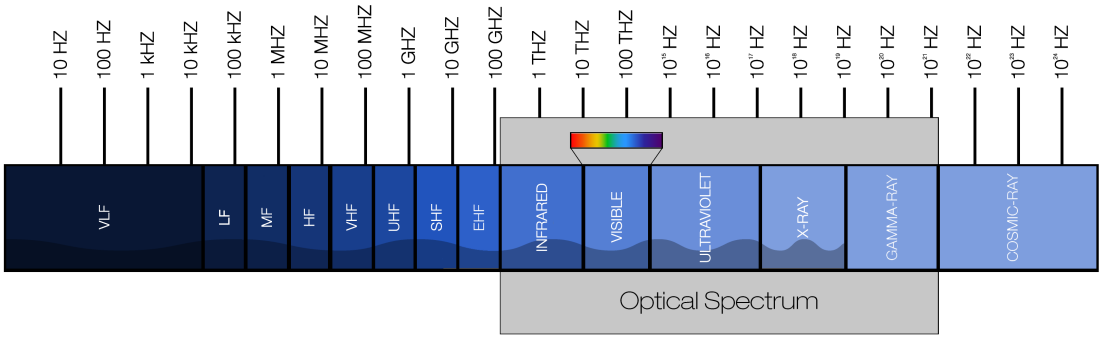

Figure 1.1: Light spectrum, emphasizing the optical spectrum [1]

Free space optical (FSO) communications, also known as optical wireless networks, increase data rates by one to two orders of magnitude over conventional RF links. Despite the fact that there has been been several space missions relying on opticalcom, the technology is still maturing demonstration in several near and deep space projects. A timeline of opticalcom missions is provided (see table 1.1) highlighting the most relevant successful missions, which have contributed nowadays to making opticalcom a convincing technology and taking the first steps to advance towards the implementation phase.

FSO systems may involve satellites, deep-space probes, ground stations, unmanned aerial vehicles (UAVs), high altitude platforms (HAPs), aircraft, and other communication assets with practical interest. For instance, the most notorious, regarding data rate, ground to ground successful optical link performed in November, 2016 by researchers at the German Aerospace Center (Deutsches Zentrum für Luft- und Raumfahrt; DLR) has demonstrated FSO data transmissions at 1.72 Tbps across a distance of 10.45 km. [17]

In contrast, concerning deep space communications –thesis scope of application– to date, no optical communications link has been closed beyond Earth-Moon distance (Lunar Laser Communication Demonstration, LLCD project; uplink: 20 Mbps, downlink: 622 Mbps) [18]. Notwithstanding the fact that the farthest communication ever achieved through FSO coms is below data rates in the order of ($\sim$ Gbps or Tbps), other missions or private companies such as ESA, EDRS or Mynaric have obtained very promising results (see Space laser communications (SLC) table 1.1).

However, not all that glitters is gold: despite deep space optical communications (DSOC) will provide 10$\times$ to 100$\times$ increased data returns over present RF space communications (as future advanced instruments will require live high definition (HD) video, tele-presence, and human exploration beyond cis-lunar space) extreme requirements for pointing, acquisition and tracking (PAT) accuracy must be fulfilled ($\sim$ μrad) because of the small optical beam divergences involved. This will have a huge impact on the spacecraft's Attitude Determination and Control System (ADCS). This challenge has to be addressed to fully exploit the benefits of optical links. Furthermore, long-haul optical links through the atmosphere suffer from fading as a result of index-of-refraction turbulence (IRT) and link blockage by obscuration such as clouds, snow and rain.

The multiple existing approaches for optical turbulence modeling in addition with the moderate Technology Readiness Levels (TRL[1]) status of optical communication devices result in DSOC network not to be nowadays still popularized and implemented, thus resulting in insufficient availability and reliability for planetary probes. For this reason, to date, there is no deep space communications network based on laser technology, as is the case with RF communications, the NASA's Deep Space Network (DSN). The DSN, over its 60 years of service, provides 24/7 coverage as well as outstanding performances. Throughout this time, it has supported multiple interplanetary spacecraft missions, as well as radio astronomy and radar observations for the exploration of the solar system and the universe.

NASA's Space Communications and Navigation (SCaN) programme has identified many fields related to optical communications requiring development. The FY2010 NASA SOMD/SCaN (FY: Fiscal Year; SOMD: Space Operations Mission Directorate) funded Deep space Optical Terminals (DOT) pre-phase-A project which identified four key technologies that need to be advanced from TRL 3 to TRL 6 in order to meet this increased performance goal while minimizing mass and power burdens on the host spacecraft. The four technologies are: a low mass spacecraft disturbance isolation assembly, a flight qualified photon counting detector array, a high efficiency flight laser amplifier and a high efficiency photon counting detector array for the ground-based receiver.

On the other hand, while it is true that a DSOC network (a.k.a ODSN, for Optical Deep Space Network) at international level is nowadays unavailable, the optical technology –to date– is reaching a significant level of maturity and consequently the Consultative Committee for Space Data Systems (CCSDS) will soon start to establish common protocols and regulations for optical spectrum frequencies on space environment. However, the existence of optical ground stations (OGS), telescopes/astronomical observatories indeed, which have served in the the previously mentioned projects (table 1.1) can be used to perform a preliminary study to serve as basis for a DSOC Network. Therefore, in the present work, only OGS which have already been employed in flown missions are considered. Even though, non-dependant astronomical ground infrastructure is lacking we will discuss which future ground assets that ODSN would be moved into in the next 50 years.

Currently, the most notorious laser communications space programme whose aim is to provide continuous coverage of satellites further to GEO (Geostationary Earth Orbit) to the edge of our solar system is the already cited SCaN. The missions that will commence to accomplish such purpose, acting as technical demonstrators, are shown in table 1.1 (LCRD, Psyche&DSOC, O2O). Figure 1.2 from [22], shows a futuristic architecture which combines RF and optical links.

[1]For a succinct explanation of the TRLs see `https://esto.nasa.gov/trl/`

STATUS	YEAR	PROJECT	LINK	MAX DATA RATE (Gbps)	Organization/ notes
DONE	1981	AFTS [19]	Airplane	N/A	McDonnell Douglas
DONE	1991	TALC	Plane-submarine	N/A	GTE
DONE	1992	GOPEX [20]	Ground to deep space	N/A	Laser beam pointing from ground to a satellite in deep space
DONE	1996	RME	Space relay	N/A	Ball Aerospace
DONE	1995	LCE/GOLD [21]	GEO-Ground	0.001	National Institute of Information and Comm Tech (NICT, Japan), JPL/NASA, Duplex links.
DONE	2001	GeoLITE	GEO-Ground	1	Lincoln Lab (USA). Duplex
DONE	2001	SILEX	LEO-GEO	0.05	European Space Agency. Duplex
DONE	2002	ALEX	GEO-Air	1	Lincoln Lab. Duplex links to GeoLITE
DONE	2005	LUCE	LEO-GEO LEO-Ground	0.05	JAXA (Japan), OICETS spacecraft
DONE	2006	LOLA	Air-GEO	0.05	France; Duplex links to SILEX
DONE	2008	LCTSX	LEO-LEO LEO-Ground	5.5	DLR/TESAT-Spacecom (Germany)Coherent detection
DONE	2011	HY-2	LEO-Earth	0.2-0.5	China's first satellite-to -earth laser communication experiment successfully conducted
DONE	2013	Alphasat	LEO-GEO	1.8	ESA
DONE	2013	LLCD	Moon-Earth	0.622	NASA/Lincoln Lab/JPL
DONE	2014	Sentinel-A	LEO-GEO	1.8	Operational use from satellites
DONE	2014	OPALS	LEO (ISS) -Earth	0.175	NASA/JPL
DONE	2014	SOTA	LEO-Earth	0.01	NICT
DONE	2016	EDRS-A	LEO-GEO	1.8	ESA
DONE	2016	OSIRISV2	LEO-Earth	1.0	DLR
DONE	2017	Sentinel-2	LEO-GEO	1.8	ESA
DONE	2017	OCSD	LEO-Earth	0.05	NASA
DONE	2020	JDRS-I	GEO-Earth	1.8	JAXA/ LUCAS
DONE	2020	CONDOR	Earth- HAP/LEO	10-20	Mynaric
DONE	2021	Starlink	LEO-LEO	N/A	SpaceX
PLANNED	2021	LCRD	GEO-Earth Earth-GEO	1.244	NASA Goddard Space Flight Center (SCaN)
PLANNED	2022	ILLUMA-T	ISS-Earth	N/A	NASA (SCaN)
PLANNED	2022	Psyche and DSOC [14]	Earth-Psyche asteroid Psyche asteroid-Earth	1.6k/0.2Mbps	NASA (SCaN)
PLANNED	2023	O2O (LEMNOS)	Earth - Orion S/C	0.08	Provide laser communications services to NASA's Orion vehicle (SCaN)
PLANNED	2020-2030	HydRON (scylight)	Earth global network	∼1000	ESA

Table 1.1: SLC timeline

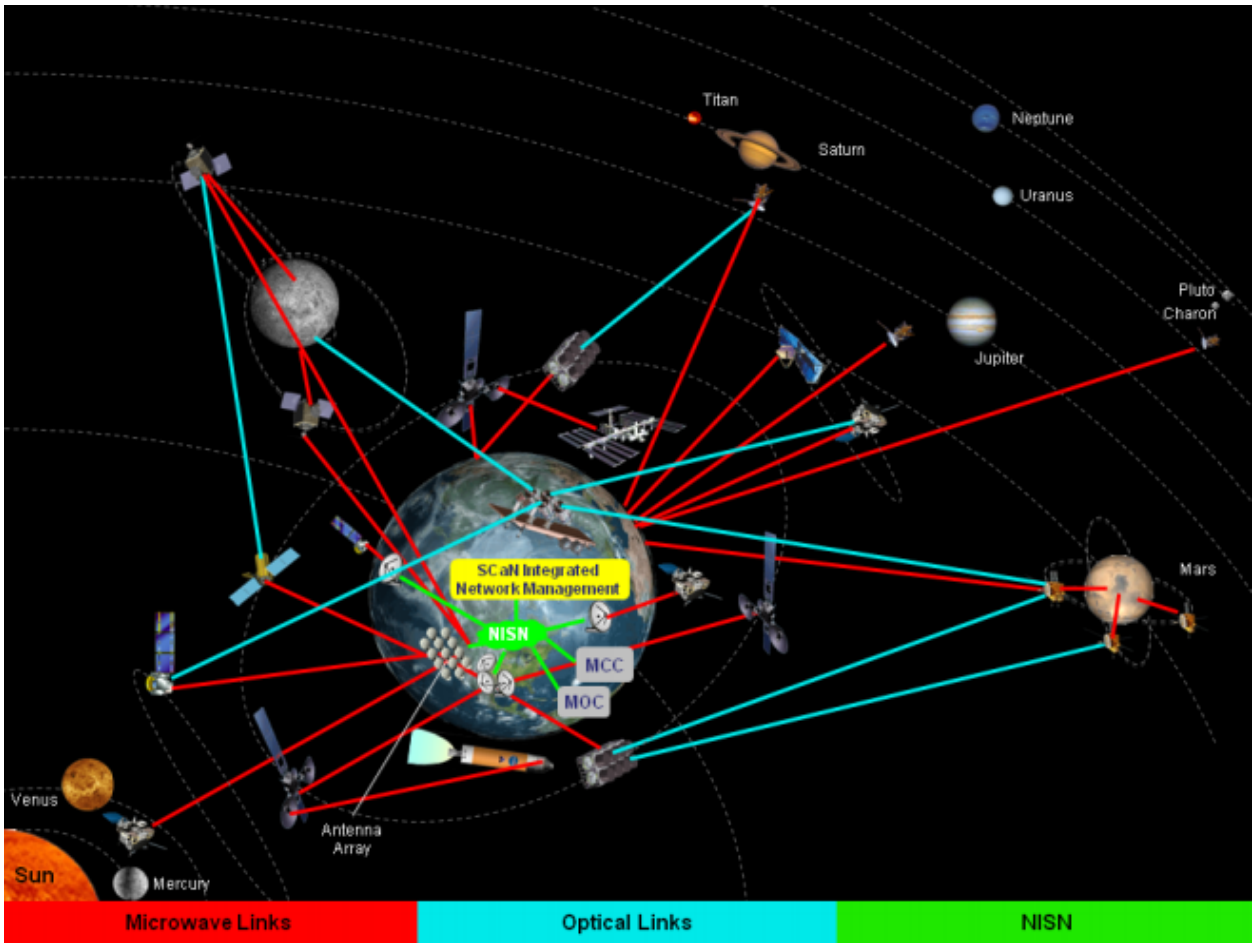

Figure 1.2: SCaN Notional Integrated Network Architecture

Advantages and drawbacks between radio and optical wireless communications are found in literature (for instance in [12, 23, 24]), and are summarised in the following sections.

1.1 Lasercom advantages

- Higher data rates can be achieved with lasercom, and with lower link losses owing to lower beam divergence. Lasercom beam widths are three to four orders of magnitude narrower than RF communication beams. Thus, the transmitted signal can be delivered to the receiver (Rx) with far higher gains. This fact implies a reduced SWaP (Size, Weight, and Power consumption).

  Although a deep space optical transceiver providing a link 10× higher than current RF links could be built with existing technologies, the mass and power performance for the data rate provided would not be competitive with existing RF telecommunications systems. Examples of benefits include frequency reuse, which allows using the same wavelength for multiple links, improved channel security, reduced mass, power consumption and size, ability to track and communicate with the sun within the field of

view, multi-functionality with other electro-optic instruments, and precision ranging.

- The optical spectrum is license-free. Therefore, there is no need to obtain a license to use the optical channels yet; considerable spectrum licensing fees can be saved comparing to other wireless RF based technologies.
- Benefits tactical applications, relative to RF systems, as lasercom systems are difficult to intercept and jam. Due to narrow beam and point-to-point transmission properties, spacial optical links have the desirable LPI/LPD (Low Probability of Intercept/Detection) properties.
- Lasercom links efficiently leverage the huge and continuous investment that has gone into the fiber optics industry to support the huge demand posed by the exponential growth of the Internet globally.
- Energetic optical photons allow for a high and even noiseless single-photon detection probability; a phenomenon that is not possible with RF communications, making possible unique communications architectures such as photon-starved regimes.

1.2 Lasercom drawbacks

However, some problems have hindered the practical deployment of wireless optical networks.

- The atmospheric turbulence, which makes link quality erratic. Atmospheric turbulence affects the propagation of optical signals, leading to degraded performance directly under various metrics such as SNR (Signal-to-Noise Ratio), BER (Bit per Error Rate), outage frequency, and so on. As [25] indicates, clouds, snow, fog affect the connectivity quality of FSO networks. For applications such as Internet delivery requiring high link availability - three nines (≥ 99.9 %), use of lasercom for through-atmosphere downlink from and uplink to the satellite may be impractical. But in applications where timely delivery of data is not critical, such as links with Earth-observation satellites, it can be used effectively.
- PAT (Pointing, Acquisition, and Tracking) techniques, which is extremely important in FSO systems because of its unguided narrow beam propagation through free space, must experience a substantial improvement. FSO systems are often designed with a divergence of a few milliradians or less in order to concentrate the optical energy at the receiver.
- Optical photons are more energetic than radio, micro and millimeter waves so higher energy per bit at optical is achieved in comparison with RF communication frequencies; this fact implies an increase of quantum noise in the optical receiver. That is, optical detectors (detecting the signal's intensity) are quantum noise limited with power detection threshold of $\sim 5 \times 10^{-19}$ W, while RF receivers (detecting the signal's field) are thermal noise limited with power detection capability of $\sim 10^{-21}$ W [24]. Given this limitation, unlike RF communications, wide-beam-divergence (especially omni-directional

transmitters) transmission of optical beams is very power inefficient.

- Lack of commercial off-the-shelf (COTS) subsystems qualified for use in space and lack of extensive ground infrastructure drive costs and development time.

1.3 Justification of the thesis

This study is based on what it has just been presented: The need to create an ODSN will be a reality in the near future. This work provides an overview of the problem and its solutions. It departures from other studies and aims to be a suitable example for others; to do so, the terms that make up the linking equation, are organised and compiled in a didactic way, either theoretically and with case studies.

1.4 Objectives

The main objective of this project is to provide an overview on the requirements to allow deep space optical communications. To do so, the thesis is divided into three main topics that account for the ground segment, the link power budget equation and two case studies in which the effects of locating the flight terminal at a huge distance, such as in deep space, are exposed. It should be noted that the term deep space concerns distances beyond cis-lunar environment.

Then, the first topic objective is to analyse feasible locations of OGS that may contribute to establish an ODSN. With the purpose of doing this, an atmospheric detailed study is presented as well as some notions of its economic viability.

The second topic objective is to break the power link budget equation terms down and analyse one by one in a systematic manner. Whereas the objective of the third topic is to provide an environment of application of such equation taking into account fictitious but realistic laser communications scenario and real technology demonstrator projects enclosed in SCaN NASA's programme.

In this framework, the thesis presents other parameters that come up when transmitting information in large distances and with terminals in motion, such as the point ahead angle or Doppler effect.

1.5 Scope

The scope of the project covers:

- A literature review on lasercoms.
- A definition of the drawbacks lasercoms have to face before being consolidated.
- A definition of the link power budget equation.
- The implementation of the link capacity model with a fictitious Mars mission.

- The validation of the link capacity model throught a real SCaN programme mission (Psyche & DSOC).
- Discussion of results and inference of conclusions.
- Analysis on the future work direction.

1.6 Requirements

First of all, in order to obtain the meteorological Earth data we have used the MODIS-LAADS DAC database [26], and for processing this data, scripts are implemented using MATLAB.

Secondly, for the analysis of the link power budget equation and thus the capacity model is also implemented in MATLAB, but with an extension of SPICE [27] applications, so-called MICE when it is used in MATLAB environment.

Finally for obtaining some key parameters concerning the link equation, as stated on this work, we have made use of the MODTRAN [28] web application.

2 Deep Space opticalcoms state of the art

2.1 Ground segment: ODSN

As stated before, ground infrastructure for deep space optical communications is lacking, but plenty of OGS are spread all over the world. However, it must be taken into account that astronomical assets are not the right answer beyond technological demonstrations, but as the objective of the thesis (obtaining the deep space optical link requirements) can be fulfilled through technical demonstrations, these assets are therefore a proper consideration. This fact can be understood because a DSN must supply 24/7 coverage and so, an optical DSN (ODSN) cannot be based by booking connectivity time-slots in astronomical research telescopes. Otherwise, astronomical observatories, progressively, are increasing the primary mirror diameter (D) which opens up the door to consider already existing barely used, or fallen in disuse, astronomical observatories($D < 2m$), (typically $D \sim 2$ m, $D \sim 5-12$ m in Tx and Rx respectively would suffice) and retrofitting them in order to meet the requirements for opticalcoms. Note that for signal reception, which implies telescopes sizing from 5 to 12m it would be necessary to establish an agreement with astronomic institutions due to its considerable demand.

In this chapter, it is presented the state of the art of the ground infrastructure that nowadays allows humankind to connect with space probes through RF and optical bands. Furthermore, it is discussed and analyzed the latest explored solutions, besought in [29], that opt to fulfill ODSN requirements, with low investment, and in a relatively short period of time.

OGS candidates for a ODSN:

In figure 2.1, according to [30], the most suitable OGS candidates for architecting the ground segment of an optical space communication network to serve Low Earth Orbit (LEO) spacecraft (S/C) are shown.

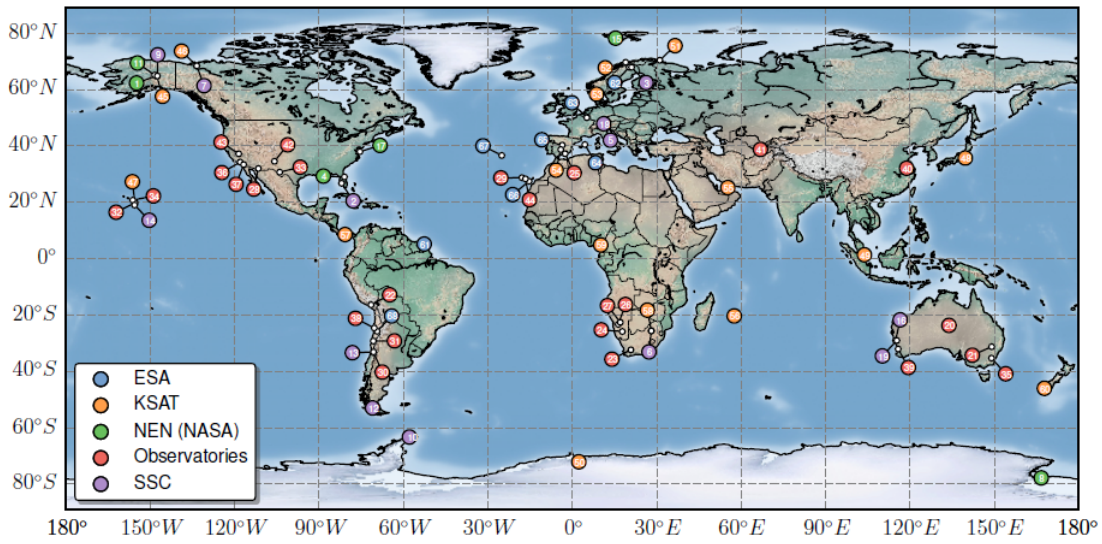

Figure 2.1: OGS candidates for an optical space communication network.

In spite of the study referring to an optical LEO network, some of the selected OGS (see table 2.1) have been part in or are contemplated to participate in deep space SCaN program (see table 2.2).

ID	Name	Latitude	Longitude	Altitude (m)	Country	Category
34	Haleakala	20.72	-156.26	2109	USA	Observatories
37	Palomar	33.36	-116.84	1780	USA	Observatories
43	Table Mountain	37.19	-118.58	2719	USA	Observatories
44	Teide	28.27	-16.64	2340	Spain	Observatories

Table 2.1: OGS which have are planned to take part in SCaN programme.

Status	Technology	Experiment	OGS	Organization	Site
DONE	Deep Space Lasercom	LLCD	ESA -OGS (Tenerife, Izaña)	ESA	El Teide (Tenerife)
			LLGT (Lunar lasercomm ground terminal)	NASA	White Sands Complex-New Mexico
			OCTL (Opt. Comm. Telescope Lab) (OGS-I)	JPL-NASA	Table Mountain Facility California (Wrightwood)
PLANNED	GEO Lasercom	LCRD (Laser Com. Relay Demo.)	OCTL (Opt. Comm. Telescope Lab) (OGS-I)	JPL-NASA	Table Mountain Facility California (Wrightwood)
			Optical Ground Station 2 (OGS-2)	NASA	Haleakala, Hawai
PLANNED	Deep Space Lasercom	Psyche & DSOC [14]	GLR (Ground laser reciever 5m-Hale Telescope)	NASA- CIT -NAOA	Palomar mountain, CA
			OCTL (Opt. Comm. Telescope Lab) (OGS-I)	JPL-NASA	Table Mountain Facility California (Wrightwood)
PLANNED	Deep Space Lasercom	O2O	-	NASA	-
CANCELLED	Deep Space Lasercom	MLCD (Mars Laser communications demonstration) [31]	-	JPL-NASA	-
CANCELLED	Deep Space Lasercom	AIM (Asteroid Impact Mission)	-	ESA	-

Table 2.2: Downlink and Uplink deep Space lasercom experiments. LCRD mission cannot be considered deep space (distance $>$ 385.000km), however O2O mission (cis-lunar border) may operate with same OGS [15]. GOPEX is not included due to only uplink was performed.

DSN based on RF band:

Analogously to astronomical observatories, a global community of DSN is spread all over the globe. Multiple space agencies such as NASA, ESA, JAXA among others are endowed by its own DSN. In figure 2.2 are shown the location of the majority of the antennas excluding the Soviet and the Chinese DSN. Despite existing multiple DSN, space agencies may cooperate among them. *Mars* 2020, is a mission example in which this international collaboration was produced, as [32, 33] indicate, the Mars Relay Network (MRN) (*Mars express*, *Mars odyssey*, TGO, *MAVEN* & MRO) connects ESA, Roscosmos and NASA's DSN to Martian ground explorers.

RF deep space communications under SCaN programme is carried out through NASA's DSN antennas which are shown in figure 2.2. This network is owned by the JPL and operated by Caltech and its main –70 m– antennas are located in Goldstone, USA; Madrid, Spain; Canberra, Australia.

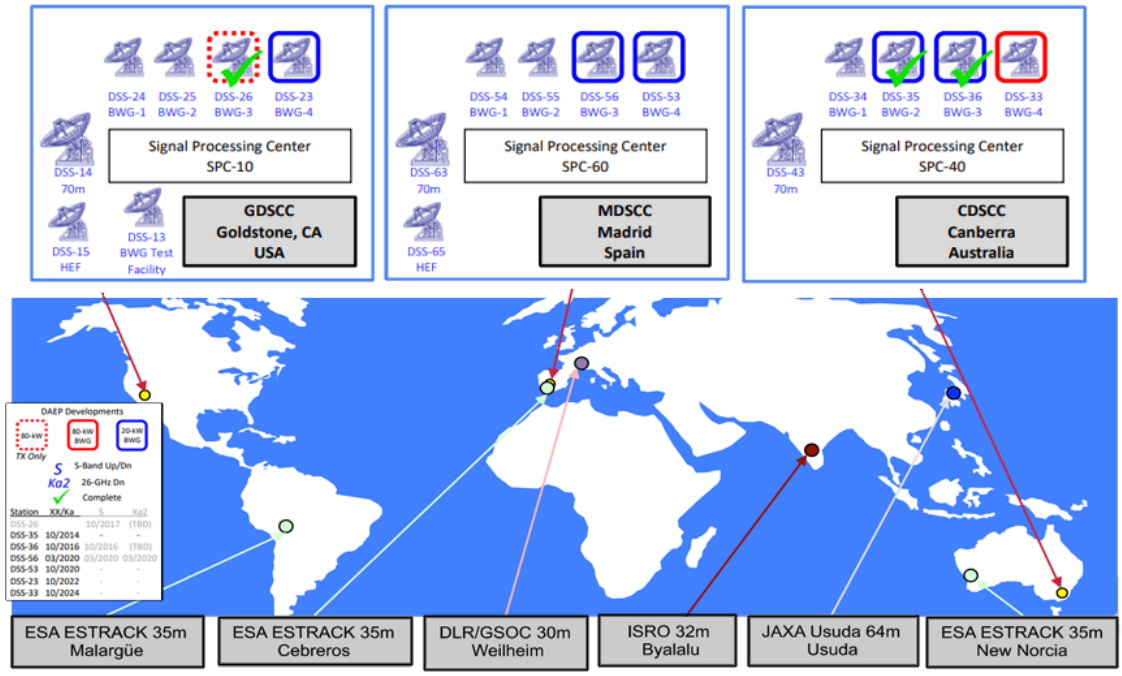

Figure 2.2: Global community of DSN (RF-antennas, Date:2021)

With current infrastructure, as expected with the LCRD and Pysche & DSOC missions, the following link model will be deployed (see Figure 2.3). As soon as deep space lasercom missions demonstrator will be successfully proven, the idea of implementing an ODNS will gain momentum.

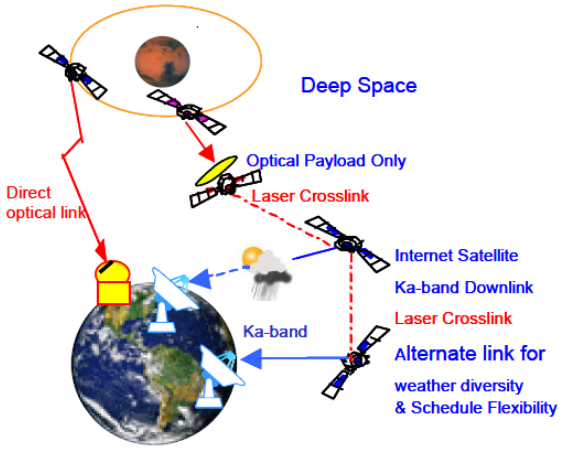

Figure 2.3: Hybrid architecture for RF/Optic ODSN [2]

In the following thesis it is presented a trade off analysis whose aim is to bring up the matter for establishing a deep space laser link configuration as function as its sun-probe conjunction and weather situation.

Up to this point, some of the intricacies that surround DSOC have been identified, in the following subsection some solutions regarding permanent optical ground infrastructure and atmospheric interference are presented.

2.1.1 ODSN implementation proposals

One of the essential characteristics of an ODSN is that its ground-based infrastructure is dedicated 24/7 to the reception of data from space probes, and therefore such a network can be established in three manners:

- METHOD A: OGS are constructed from scratch, taking into account cluster or linear ODSN configuration, as [2] suggest.
- METHOD B: OGS that are currently exploited for astronomical research are absorbed by a ODSN and retrofitted in accordance with the requirements of the moment.
- METHOD C: Current DSN antennas are retrofitted, [3, 29, 34], in order to allow hybrid ground stations (optical and RF operation bands).

For Method A, cost becomes one of the drivers of the ODSN erection. Thus, a short analysis of the cost associated to telescope design and construction seems indispensable.

According to [12, 35–37] telescope cost (C) increases exponentially with the aperture diameter (D). The cost-aperture power law is defined as following:

$$C \propto D^x \tag{2}$$

Where exponent x has a value between 2.4 and 2.8. In a detailed study [36] multiple OGS construction costs were analysed, the results are illustrated in figure 2.4. The cost is adjusted

to 2000 epoch, taking into account that 1 USD in 2000 is equivalent in purchasing power to about 1.54 USD today, an increase of 0.54 USD over 21 years. The dollar has had an average inflation rate of 2.07% per year between 2000 and today, producing a cumulative price increase of 53.82%. In this way, it is possible to estimate the cost of building telescopes today; one of the yellow dots on the graph corresponds to the GTC. At the moment the paper was written (2004) there were not enough data points to determine if the GSMs (Giant Segmented Mirror) will also follow a cost $\propto D^{2.46}$ power law; however, the authors naively expected for the cost-aperture relationship to generally adhere to this slope. Anyway, the cost-aperture power law is a useful –and widely-used in the Astronomy arena– tool for extracting approximated costs of new telescopes.

Telescope	Institute	Size(m)	Cost (M USD)	Year	Adjusted Cost (2000)	Adjusted Cost (2021)
GTC	Spain	10.4	90.6	1997	95.3	146.57

Table 2.3: GTC data used in this analysis.

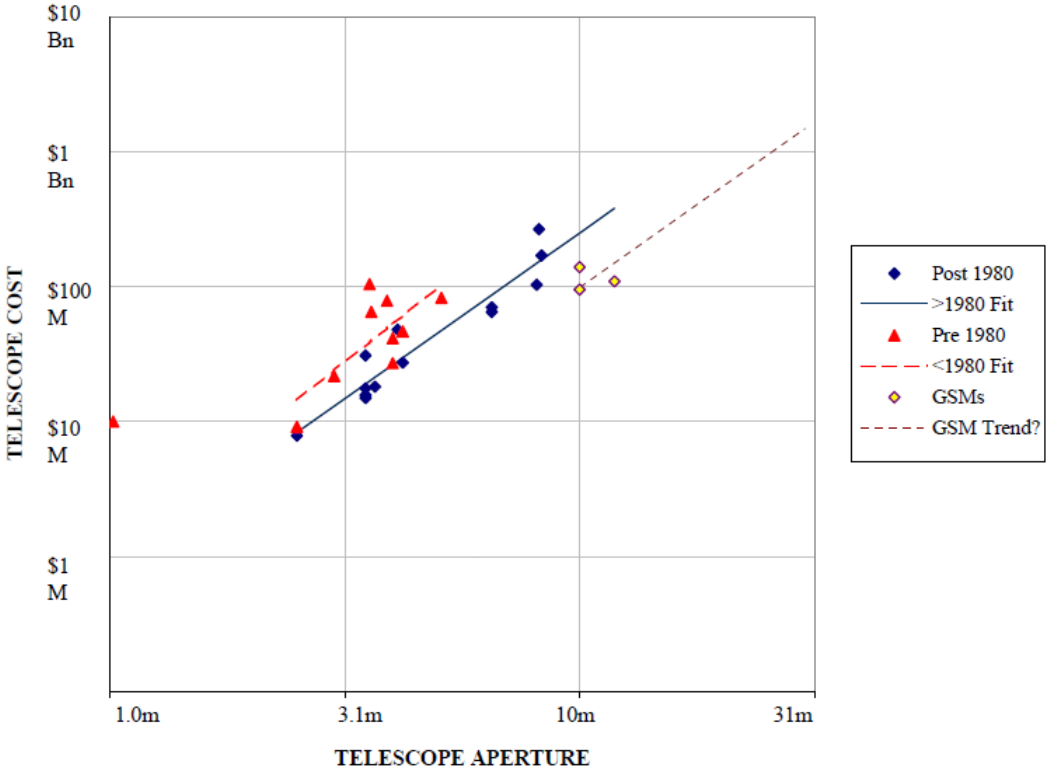

Figure 2.4: Cost versus aperture diameter for optical telescopes built before and after 1980. For the pre-1980 fit, cost $\propto D^{2.77}$, and for the post-1980 fit (exclusive of the giant segmented mirrors), cost $\propto D^{2.46}$.

Let's observe an example of estimating the cost for a new optical telescope. The Extremely

Large Telescope (ELT) will be the world's biggest eye on the sky, it is expected to be completely built in 2025. By employing the scaling law we can compute the construction cost as follows:

$$\frac{D_{\mathrm{ELT}}^{2.46}}{D_{\mathrm{GTC}}^{2.46}} = \left(\frac{39.3}{10.4}\right)^{2.46} = 26.32 \tag{3}$$

$$C \propto D^{x}$$

$$C_{\mathrm{ELT}} = 146.57\,\mathrm{MUSD} \times 26.32 = 3.8\ \text{billion USD (short scale)}$$

Apart from the construction cost, of equal or greater importance are the operating costs: as [37] states, large observatory operating costs ranged between 2.5% and 3.5% of facility construction cost not including "salaries of academic or scientific staff, support of graduate students, or other program-cost items such as scientific libraries." Most large observatories spend another 3% to 5% per year on development of new instruments and/or adaptive optics systems. Therefore, over a $\sim$ 30 year lifetime, the cost of running an observatory is two to three times higher than the construction cost. As it has been exposed the costs for creating OGS from scratch are remarkable, the large cost of dedicated receive telescopes makes this method (METHOD A) unrealistic —at least in the near-term. So, other methods such as retrofitting astronomical observatories (method B) and relinquish it purpose of research for switching to opticalcoms are more plausible. The case of the first deep space optical communication mission, Psyche & DSOC [7, 14] is an example that sustains such methodology. This mission, which is expected to be launched in 2022, will make use of two OGS, A 5 kW average power 1064 nm beacon laser from Table mountain OGS ($D = 1$ m) will be used to illuminate the spacecraft. Whereas the S/C flight laser transceiver (FLT)($D = 22$ cm) allow pointing of the 1550 nm downlink laser back to the GLR ($D = 5$ m) Hale telescope in Palomar Mountain, CA.

Finally, an study considering method C has been carried out at JPL [3,29,34] suggesting that for relatively low investment, retrofitting optical surfaces to existing RF antennas might be an option.

A priori, the proposal sounds pretty promising taking into account that when settling the bases for a new ODSN many aspects aside from technical features have to be considered. In [2] a summary of this further concepts such as political factors, licenses, climate conditions and network architecture among others are found. This JPL study case is revolutionary because all these further concepts are already solved, so the ODSN would be in fact the same ground infrastructure as RF-DSN but with some antennas being optically retrofitted as illustrated in figure 2.5. More specifically, the study indicates NASA is in the midst of building six new 34 m BWG antennas in the DSN. Two out of six were planned to be built at the DSN Goldstone, California and Canberra, Australia, complexes. The authors were investigating building these last two antennas as RF/optical hybrids. By delaying their operational dates by two years (timeline may have changed due to COVID-19 global pandemic) so they would be able to add the 8 m optical receive capability for these two antennas while fitting within existing budgetary constraints.

JPL has done analysis for NASA's ongoing next generation architecture studies that show DSOC will need the equivalent of an 8–12 m ground telescope to support the links that are expected to be needed for human missions to Mars. For this reason the size hybrid antennas mirrors design is established to be 8 m, equivalent to an state-of-the-art optical primary. The authors looked at adding a larger surface area for the optical portion of the RF/Optical hybrid, but beyond 8 m it would have to both increase the mass and distribute the loads outside the integral ring girder of the reflector. This would make the spherical aberration correction system more complicated and require a mechanical structure update for additional mass and moments.

In the experiments performed in the paper, the hybrid antennas were not designed for optical uplink. Instead, a smaller optical station somewhere nearby would supply uplink. Both RF and optical signals could be received (and RF transmitted) simultaneously in operations (see figure 2.5). In all cases, the authors conclude the cost of the hybrid was less than half of what would be expected for monolithic system OGS (same diameter size) with the savings achieved by leveraging the existing and planned Deep Space infrastructure.

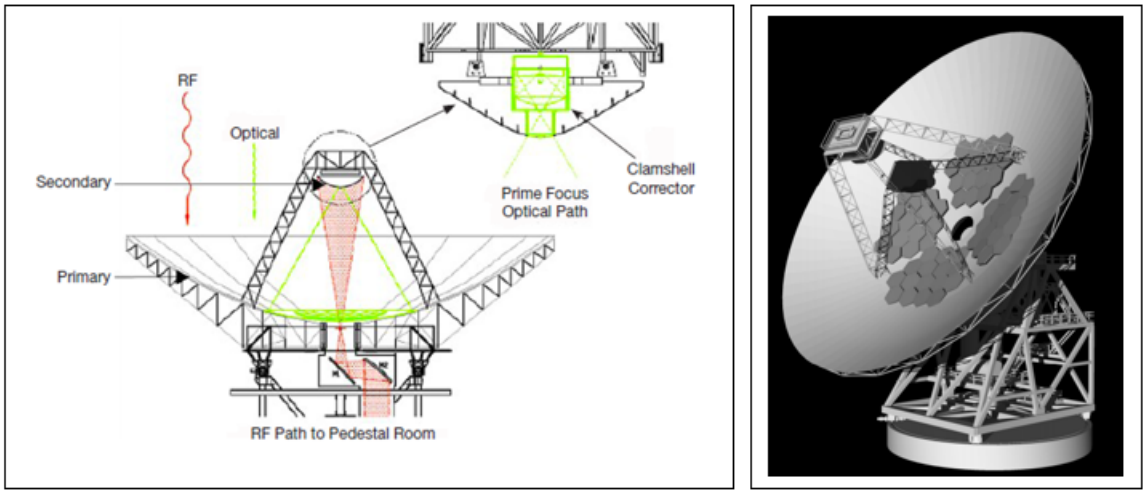

Figure 2.5: Side view of the RF/optical concept, including ray paths. [3] (right) RF/Optical Antenna Concept render (left).

In order to contribute in attenuating the atmospheric perturbations, multiplexed system with several lasers on separate wavelengths could be used if required. As [38] (among others) have concluded, multi-beam propagating technique is an effective way to reduce the effects of scintillation. Despite a laser beam which is travelling through the atmosphere cannot get rid of scintillation effects it can be emitted or received in a cloudless sky, by having a cluster of ODSN antennas with sufficient distance among them, it might decrease the cloud fraction and the optical cloud thickness and thus the laser beam blockage. RF transceivers can help to avoid this atmospheric perturbation in worst weather situations.

Admittedly, the ultimate solution to atmospheric disturbances involves relocating OGS away from the Earth, in other planets or natural satellites with nearly non existing atmosphere or

settling transceiver satellites in solar system libration points, albeit it would not be a very realistic approach to envisage such projects for the 20s-30s decades. Figure 2.6 exemplifies ODSN future locations; OGS in the moon (left) and as satellite relay in a libration point (right).(Ilustration on the right is in fact a render for the NASAs LCRD mission, TBL in June 23, 2021.)

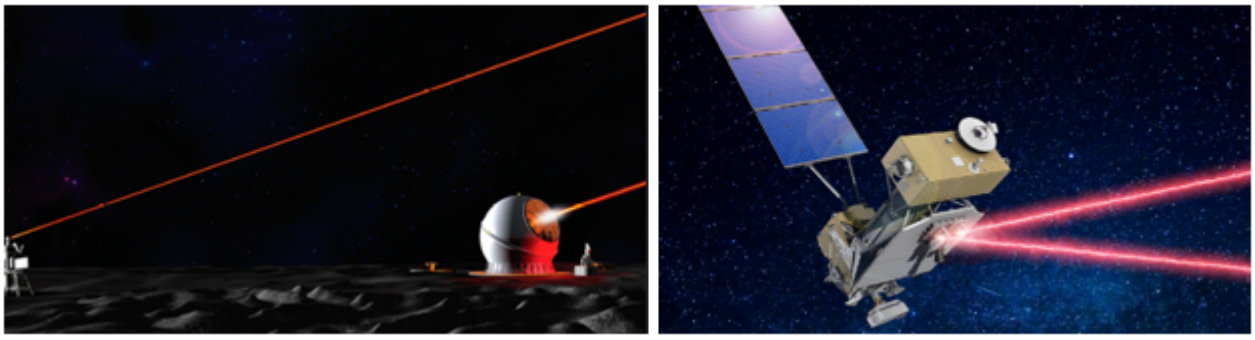

Figure 2.6: An artist's rendering of feasible future ODSN locations. Credits: NASA, University of Southern California, Charles University Prague.

2.1.2 Feasibility analysis: Cloud fraction and Aerosol analysis

One of the multiple reasons that have conducted Earth-to-space optical communications not to be yet established on a daily basis, refers to the outage effect caused by atmospheric phenomena. We all have observed how as a thunderstorm approaches the sunlight is partially blocked (light trespassing degree will depend on cloud optical thickness) and consequently the sky darkens. This phenomena in addition with scintillation (that occurs even with clear sky) is the main reason why astronomical observatories are placed in regions where the cloud fraction coverage is minimum and set in a higher altitudes to minimise the amount of atmosphere that light has to travel through. For this reason, prior to selecting which method would be more feasible (methods B or C) for implementing an ODSN it is presented a cloud fraction coverage study (method A has been already ruled out unless there was no alternative).

First of all, cloud and aerosol data have to be acquired from several available databases. We have considered suitable remote sensing data generated by *MODIS* (MODerate resolution Imaging Spectroradiometer) [39] available online at LAADS DAAC (Level-1 and Atmosphere Archive & Distribution System Distributed Active Archive Center) [26]. The spectroradiometer installed on board the satellite *Terra* has generated data for more than 20 years, since *Terra* was launched in late 1999 with the data stream beginning in late February 2000, followed by its counterpart *Aqua* in May 2002. *MODIS* features spectral and spatial resolution in key atmospheric bands that expand the capability to globally retrieve cloud properties. The *MODIS* atmosphere products are archived into two categories: pixel-level retrievals (Level-2 products) and global gridded statistics at a resolution of 1° (Level-3 products).

The Level-3 Atmosphere (MOD08) consists of approximately 800 statistically derived data

sets (SDSs) from the Level-2 products. Statistics are computed over a 1 degree equal-angle lat-lon grid that spans through a monthly, 8-day or daily average interval. Since the grid cells are 1×1 degree, the output grid is always 360 pixels in width and 180 pixels in length. To assess the cloud coverage study, the Level-3 SDS 'Cloud_Fraction_Mean_Mean', 'Cloud_Top_Height_Mean_Mean' & 'Deep_Blue_Aerosol_Optical_Depth_550_Land_Mean_Mean' from MODIS on-board Terra (i.e., MOD08 product, Collection 6.1) are analyzed. In order to obtain data redundancy, it could have been analyzed as-well files form its counterpart Aqua but has been dismissed.

On LAADS DAAC database data is stored as hierarchical data files (.hdf), for MODIS Level-3 HDF product, files have standardized [40], described below:

MOD08_X3.AYYYYDDD.CCC.YYYYDDDHHMMSS.hdf

The definition of the highlighted text is as follows:

MOD08 = Earth Science Data Type name. (MOD: Terra, MYD: Aqua)

X3 = X: M(monthly), E(eight days) or D(daily) data; 3 stands for a Level-3 product.

A = indicates following date/time information is for the acquisition (observation).

YYYYDDD = acquisition year and day-of-year.

CCC = collection number (e.g., '006' for Collection 6, '061' for Collection 6.1).

YYYYDDDHHMMSS = production data and time hdf file format.

In an attempt to obtain the Earth cloudy regions overview, the study, reviews two decades (2000-2020) of generated data. To do so, monthly MODIS data product (MOD08_M3) has been taken as an input and after data processing (see algorithm 1) a general $1 \times 1^{\circ}$ resolution, two decades average along the planisphere has been attained.

Algorithm of `AnnualMeans`; Earth cloud fraction mean from 2000-2020

Data input: MOD08_M3 product, Collection 6.1, HDF format;
Data output: 360 pixels in width and 180 pixels in length two decades world average cloud fraction grid called TDMM;
foreach MOD08_M3 HDF file **do**
  Sort HDF files into annual folders from 2000 to 2020 ;
end foreach
Initialize to zeros TDM ← Two_Decades_Matrix ;
foreach Annual folder **do**
  Extract from stored HDF MOD08_M3 HDF files the SDS 'Cloud_Fraction_Mean_Mean' to a (180x360) matrix MMM ← Monthly_Matrix_Mean ;
  Sum all MM into AMM ← Annual_Matrix_Mean;
  Divide the AMM over the numbers of files available in the folder.
  TDM= TDM + AMM;
end foreach
TDMM=TDM/20← Two_Decades_Mean_Matrix;

Algorithm 1: Earth cloud fraction mean from 2000-2020.

The resulting 1×1 degree resolution, world cloud fraction two decades mean matrix (TDMM) is shown in figure 2.7.

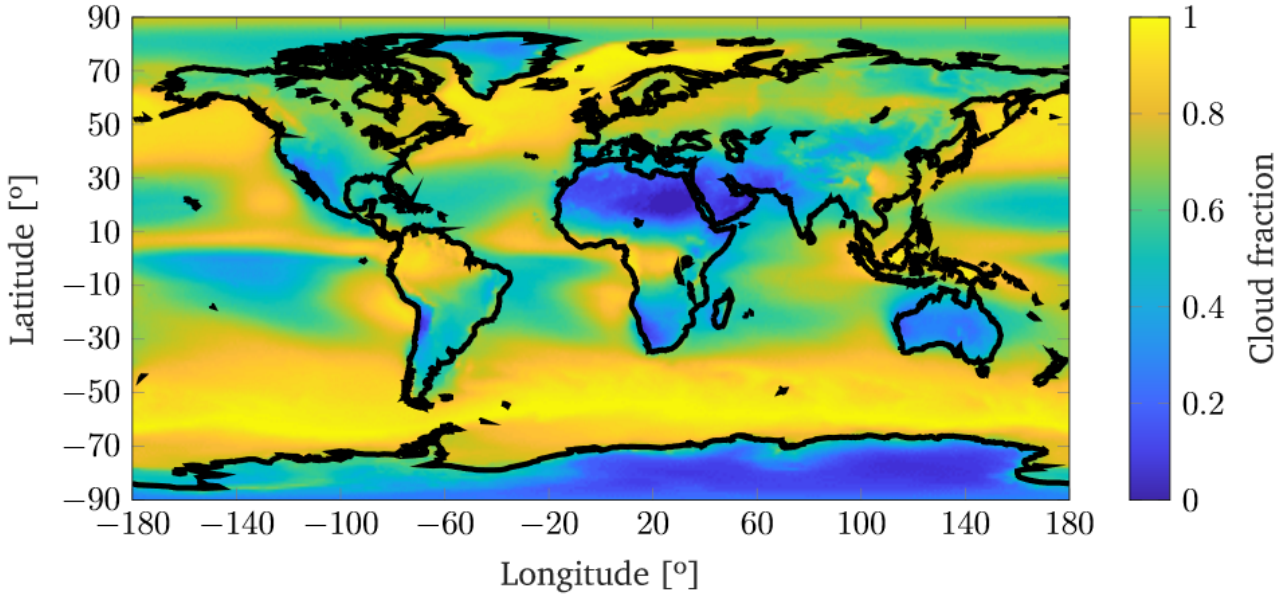

Figure 2.7: 2000-2020 average Cloud fraction. 1×1 degree resolution.

In order to have a cloud top height overview and visualizing if clouds are set below mountains summits (typical OGS locations) just by changing the SDS in the algorithm 1 the resulting 1×1 degree resolution, cloud top height's two decades mean matrix (TDMM) is shown in figure 2.8

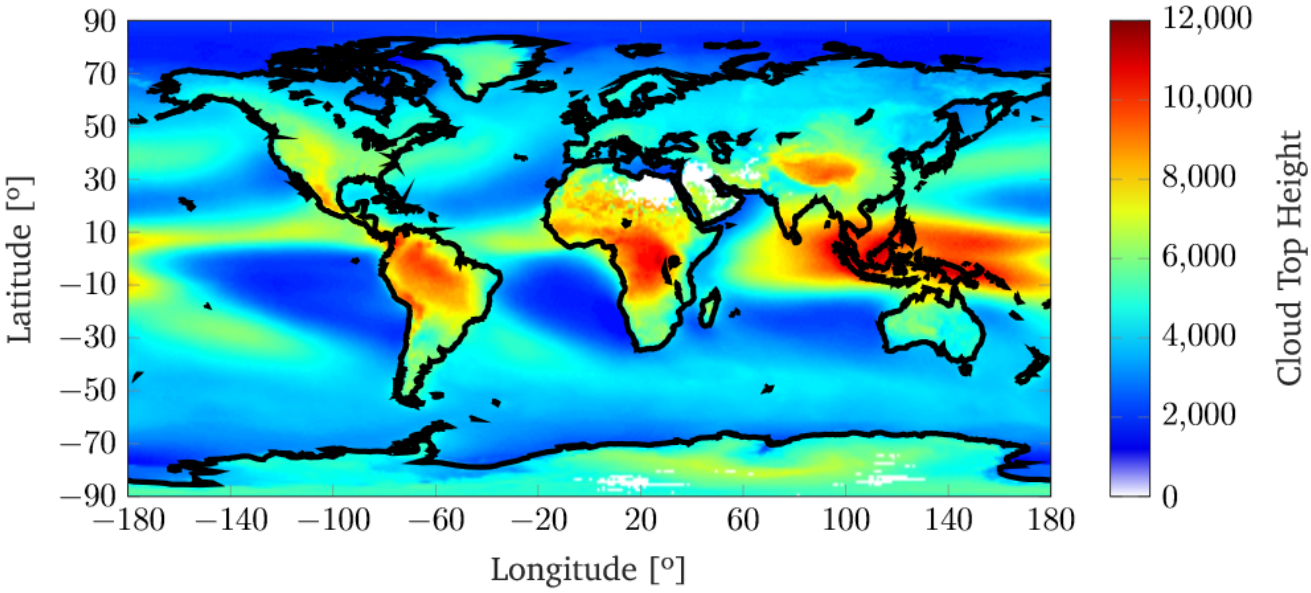

Figure 2.8: 2000-2020 average Cloud top height [m]. 1×1 degree resolution. No data generated in white regions.

Without delving deeper, one can realise method C proposed in [3, 29, 34] is more favourable for Goldstone and Canberra (with lower serviceableness) DSN complexes where cloud fraction values are lower (see figure 2.9). The main deduction is that even if DSN as a whole is retrofitted for transiting towards an ODSN, it will not suffice. Since Canberra's cloud fraction goes two points above and Madrid's duplicates Golstone's cloud fraction, it would be necessary for ensuring maximum availability against bad weather conditions, to locate an OGS replacing Madrid complex elsewhere, for instance in Canary islands.

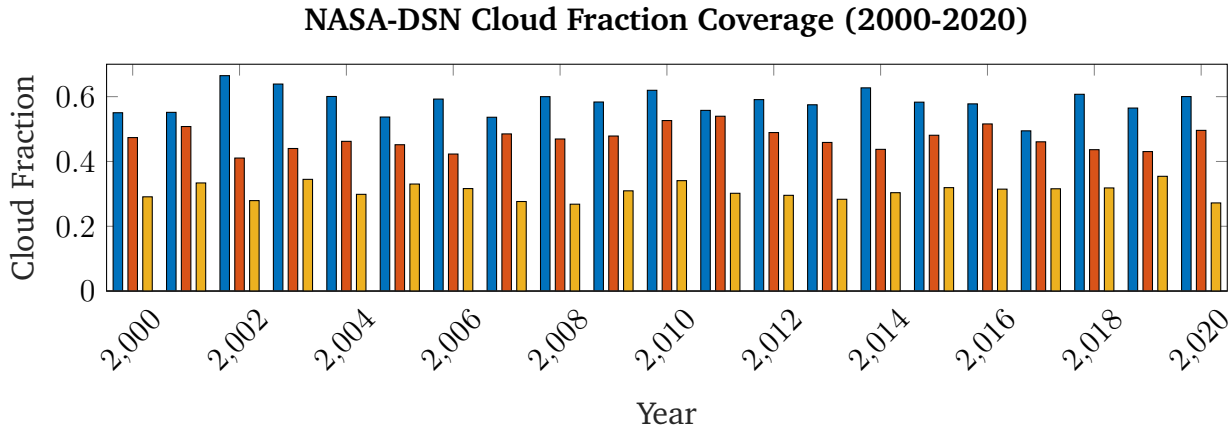

Figure 2.9: Cloud fraction from 2000 to 2020 at DSN complexes. Madrid (blue), Canberra (orange), Goldstone (yellow).

Articles [3, 29, 34], which are considered in this thesis to follow method C concept, discuss about taking profit of fallen in disuse RF big deep space antennas. In fact, method C gathers the same philosophy as method B, as deep space probes need to have a permanent availability

ground segment it does not make any sense, at least in the near-term, to retrofit a deep space antenna which is being operative for serving forthcoming deep space probe operating in optical regime. For this reason [3, 29, 34] propose to utilize DSN antennas that may have fallen in disuse in order to start the RF based DSN to an ODSN transition with lower budget impact.

Figure 2.7 presents a synoptic scale cloud fraction. By reading the displayed results one can extract the first conclusions: Atacama desert in Chile, Mojave desert in California-USA , Australia, South Africa, Northern Africa, Middle East, Greenland and Antarctica are the regions where, as regards cloud fraction, OGS could be placed.

Nevertheless, not only clouds can block or attenuate the intensity of the laser beam; Aerosols such as desert dust, biomass burning particles, transport pollution, marine salt [41] among others act as well as an obstruction factor by absorbing or scattering photons. If only the results posted in Figure 2.7 where analysed one could commit a mistake while deciding the best locations for OGS. Hence, an aerosol study for the lower cloud fraction regions has been executed in the same procedure as algorithm 1 but changing the SDS to 'Deep_Blue_Aerosol_Optical_Depth_550_Land_Mean_Mean', which is one of the multiple SDS available in *MODIS* concerning aerosols retrieval.

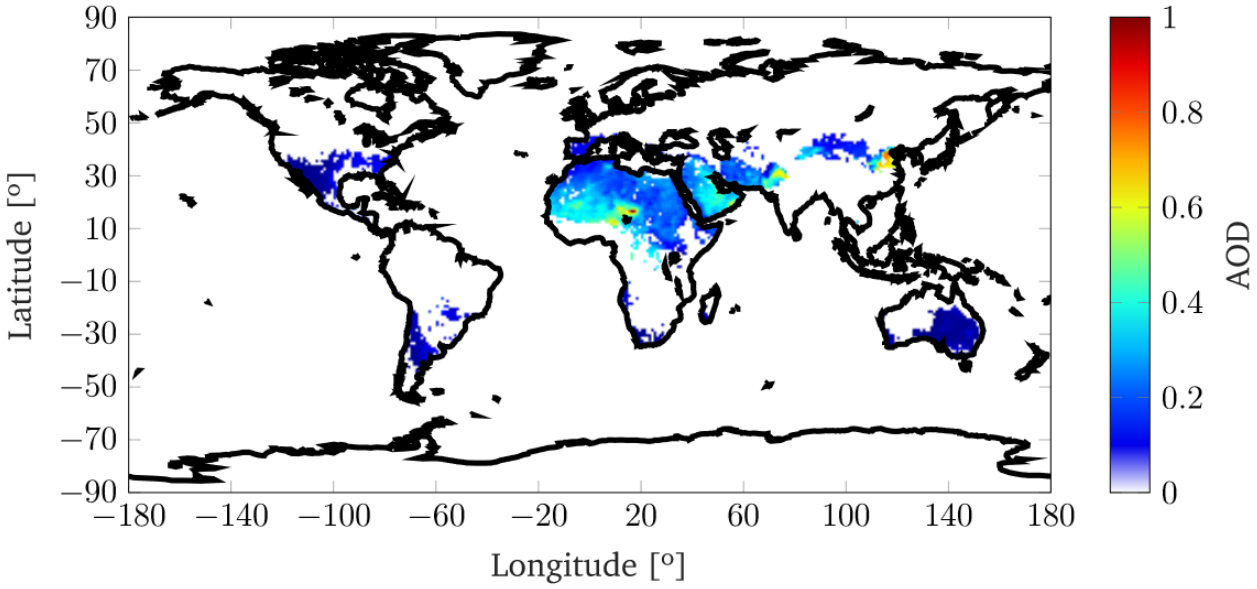

Figure 2.10: Spatial distributions of two decades mean Aerosol optical depth [-] for *Terra MODIS* C6.1 Deep Blue datasets at at 0.55 μm. Data from 2000 to 2020. No data generated in white regions.

Regarding the cloud coverage study, Northern Africa and Middle East seemed to be proper location for settling OGS, however the aerosol study shown in Figure 2.10 indicates that these regions are especially affected by aerosols in comparison with other cloudless regions. At first sight, similar to [30], Atacama desert in Chile, Mojave desert in California-USA , Australia,

South Africa, Southern Spain and Canary Islands, Hawaii, Northern-West India among others gather the best conditions for setting permanent OGS serving to ODSN.

The study's final conclusion and therefore the most feasible proposal to ensure an ODSN in the near-term future would be a combination between methods B and C, for the reasons set out in the items hereunder.

- ODSN must consist of a number of ground stations located around the Earth as a linear distributed optical subnet (LDOS). Ideally the ground stations would be located between latitudes $-40°$ and $+40°$, as deep space probes' main purpose is to explore solar system bodies which are placed at the ecliptic plane.
- Since the laser transmitter beam width from space may cover a limited area on Earth (see figure 2.11) it is necessary that the ODSN consists of a number of ground stations located around the Earth as a LDOS, similarly to the current RF DSN stations which are located at approximately 120 degrees of separation in longitude.
- Despite the most favourable regions are endowed with low cloud fraction values, it does not entail sometimes outages might be produced by clouds/aerosols appearance. Furthermore, when the line of sight is too low on the horizon (20 degrees of elevation or less) turbulence may significantly worsen the link quality. For this reason, OGS redundancy is a must. Nowadays NASA's DSN is not equipped with redundancy because fading caused by clouds is not a worry in RF.

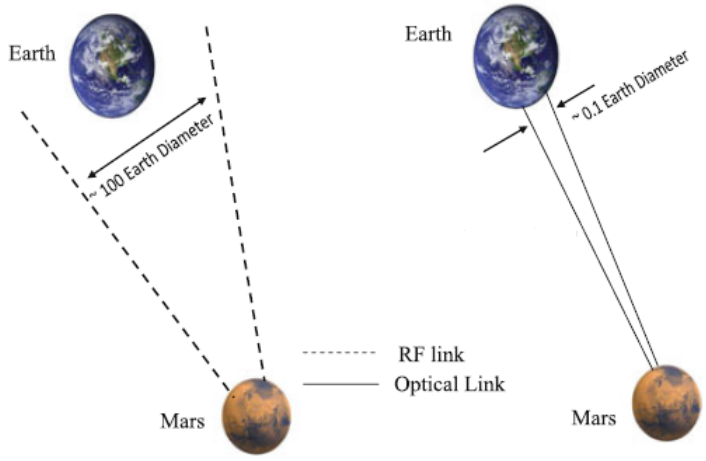

Figure 2.11: Comparison of optical and RF beam divergence from Mars toward Earth [4]

Some of the OGS that may fit in ODSN concept were previously mentioned at 2.1. Attending the study's obtained data, we propose to follow LDOS architecture with the following OGS (see table 2.4). (In section 3.3.1 from [12] several architecture proposals such as cluster optical subnet –COS– are described). The idea behind LDOS is that the probes' laser beam is pointing at a visible station belonging to the LDOS, but anytime the beam could cover two nodes of LDOS, due to its divergence, knowing that the pointed node is receiving the maximum intensity and at footprint surroundings will experience some losses.

Node	Country	OGS	Function
I	Australia	AAT (Anglo Australian Telescope)	Tx
		Canberra DSN complex	Rx
II	India	Indian Astronomical Observatory (IAO) (Hanle)	Rx
III	South Africa	-South African Astronomical Observatory (SAAO) 1.9m Telescope	Rx
IV	Spain (Canary Islands)	- OGS Teide (Tenerife)	Tx
		- Isaac Newton (La Palma)	Rx
V	Chile	Paranal, La Silla complexes	Rx
VI	USA, CA	- TMF	Tx
		-5 m Hale Telescope (Palomar) -Goldstone DSN Complex (retrofitted)	Rx
VII	USA (Hawaii)	- Haleakala	Rx

Table 2.4: ODSN proposal and suitable candidates.

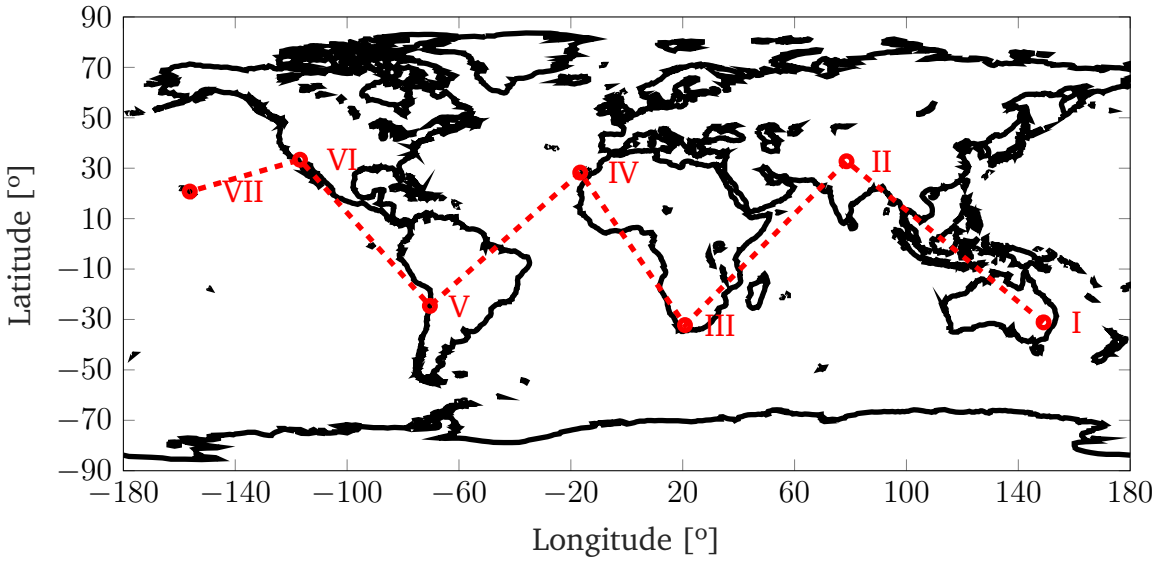

Figure 2.12: ODSN nodes.

3 Link Power budget equation

Laser communications data transfer schematic resembles RF communications. Equivalent to RF, in lasercom data must be modulated prior to be transmitted by the antenna. Due to the finite speed of the light, beam pointing system is anticipated taking into account that the receiver terminal has moved and it is no longer at the angle it was observed.

For deep space optical communications the channel is the outer space, however if the transmitter or receiver is located on the Earth then the atmosphere also plays an important role in terms of wavefront distortion. Finally, when the laser beam encounters the receiver which is continuously monitoring the transmitter (tracking), signal and background photons, these last are filtered to increase SNR, hit the detector (generally an avalanche photo-diode) and can be demodulated and deciphered the containing data.(see Figure 3.1)

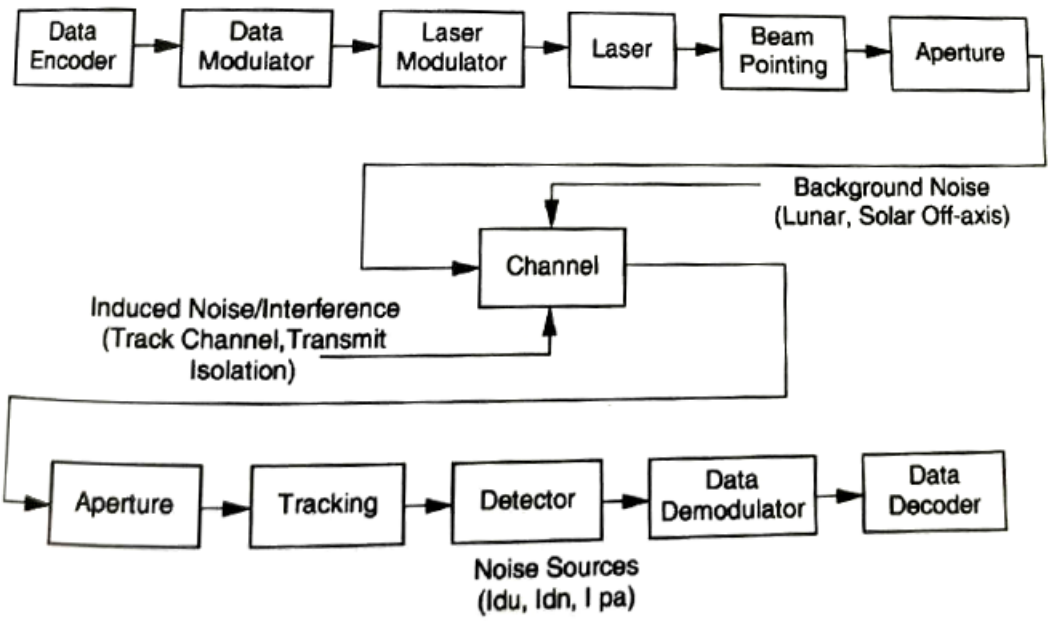

Figure 3.1: Data transfer link model [5].

At Deep Space Communications and Navigation Center of Excellence (DESCANSO) [42] book series Volume 7, it is detailed the most general from of the link equation model ([12], page 89). Other equivalent expressions can be found in literature with slightly different nomenclature [5, 43].

The link budget or link equation model presented in this thesis is mainly based on the approach presented in Ref. [44] as well as the previously mentioned references. After rearranging some terms the equation becomes;

$$P_{\mathrm{Rx}} = P_{\mathrm{Tx}} \cdot G_{\mathrm{Tx}} \cdot G_{\mathrm{Rx}} \cdot S \cdot \phi \tag{4}$$

Where:

- P_{Rx} [W] is the signal power received.
- P_{Tx} [W] is the signal power transmitted.
- G_{Tx} is the gain of the transmitter telescope, is given by:

$$G_{\mathrm{Tx}} = \left(\frac{\pi D_{\mathrm{Tx}}}{\lambda}\right)^2 \tag{5}$$

  Being D_{Tx} [m] the transmitter aperture diameter and λ [m] the transmit wavelength.

- G_{Rx} is the gain of the receiver telescope, is given by:

$$G_{\mathrm{Rx}} = \left(\frac{\pi D_{\mathrm{Rx}}}{\lambda}\right)^2 \tag{6}$$

  Being D_{Rx} [m] the receiver aperture diameter

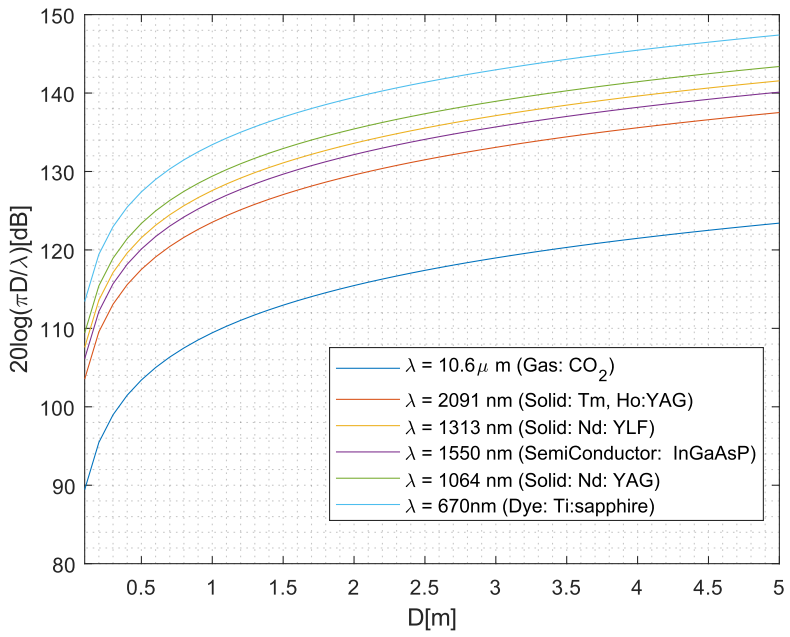

Figure 3.2: Maximum theoretical gain available from a circular aperture of diameter D for relevant laser wavelengths.

- S is the space loss (also known as range loss), it depends on the link propagation distance R and is given by:

$$S = \left(\frac{\lambda}{4\pi R}\right)^2 \tag{7}$$

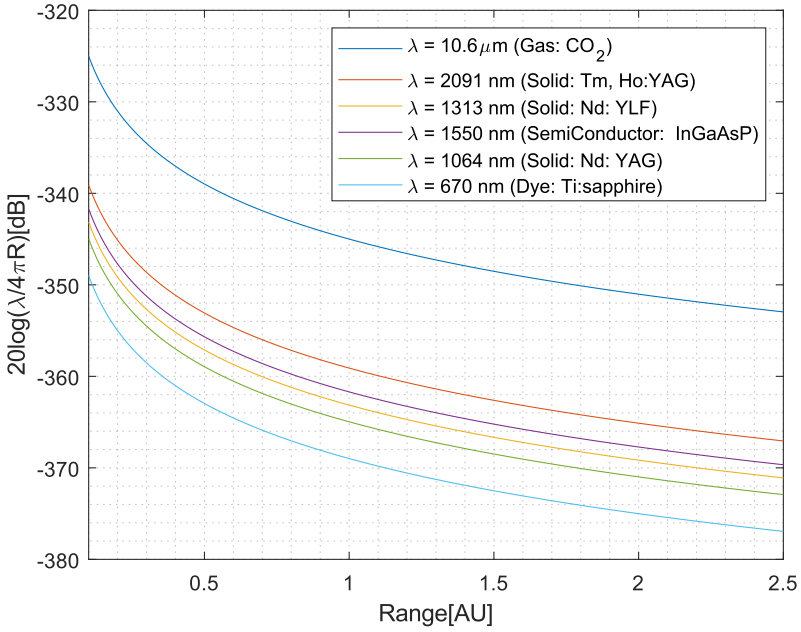

Figure 3.3: Free space loss for relevant laser wavelengths.

- ϕ reflects all the other system-dependent lower losses and efficiencies. Despite in ([12], page 89) ϕ term does not strictly appear on the link budget equation, it has been considered to gather all the remaining terms under this parameter, in order to denote that space losses are more significant than those gathered by ϕ parameter. ϕ is equivalent to the following terms from link budget equation ([12], page 89) :

$$\phi = \eta_{\mathrm{Tx}} \cdot \eta_{\mathrm{A}} \cdot \eta_{\mathrm{TP}} \cdot L_{\mathrm{atm}} \cdot L_{\mathrm{pol}} \cdot \eta_{\mathrm{RP}} \cdot g_{\mathrm{R}} \cdot \eta_{\mathrm{Rx}} \cdot \eta_{\lambda} \tag{8}$$

Where:
η_{Tx} is the transmitter optics efficiency.
η_{A} is the aperture illumination efficiency of the transmitter optics.
η_{TP} is the transmitter pointing efficiency, defined as the ratio of power radiated in the direction of receiver to the peak radiated power. If the transmitter is directly pointed at the receiver, the pointing loss is 0 dB.
L_{atm} is the fractional loss due to absorption of the transmitting medium (e.g., Earth atmosphere and any occluded planet atmospheres)
L_{pol} is the fractional signal loss due to mismatch of the transmit and receive antenna polarisation patterns. It has been considered out of the scope of this thesis, consequently, some random values will be assumed.
g_{R} is the receiver efficiency factor or receiver gain efficiency. Is given by [45]:

$$g_{\mathrm{R}}(\mathrm{dB}) = 10\log(1-\gamma_{\mathrm{rx}}^2) \tag{9}$$

where γ_{rx} refers to the obscuration coefficient for the receiver antenna. As shown in

Equation12 η_{RP} is the detector truncation loss factor, defined as the ratio of receive antenna gain in the direction of the transmitter to the peak receive antenna gain.

η_{Rx} is the receiving optics collecting efficiency, defined as the fraction of optical power at the receiving aperture that is collected within the field of view of the receive detector. η_λ is the narrow-band filter transmission efficiency.

Furthermore, it must be noticed that the laser beam is assumed to follow a Gaussian intensity profile (TEM_{00} geometry, where TEM stands for Transverse Electromagnetic Mode which results in maximum concentration of the laser beam).

3.1 Transceiver optics & narrow-band filter efficiencies (η_{Tx}, η_{Rx}, η_λ)

The parameter η_{T} in the link power budget equation (Equation 4) is the transmitter optic efficiency that takes into account the transmission and reflection losses in the transmitter laser beam routing through the optomechanical assembly, OMA (relay optics, steering mirrors and the telescope) (see Figure 3.4) Its typical values are in the range of 0.4 to 0.7 [4], depending upon transmission and reflection coefficients of the optical components in the transmitting system. In order to obtain the system efficiency it should be studied for each particular case, but generally it is a data given by the optic manufacturer. If this data is not provided, there are methodologies that allow to obtain it; for instance with, RF systems this parameter is studied with an anechoic chamber.

The other receiver parameter η_{R} in the range equation (Equation 4) is the receiver optic efficiency that will take into account the transmission and reflection losses in the receiver. Its typical value ranges from 0.5 to 1. Also, it is necessary to take into account the narrow band filter (NBF) transmission efficiency η_λ, which is given by the manufacturer. The narrow band filter is an important component in the optical communication system as it greatly affects the sensitivity and background noise rejection (see Figure 3.4). Ideally, the filter should have 100% transmission in the pass band and a very narrow spectral bandwidth ~~filter~~ (e.g., $\Delta\lambda_{\mathrm{NBF}} = 1$ Å or less). The size of the filter is used for calculating the background noise power detected by the receiver system.

3.2 Aperture illumination efficiency (η_{A})

The aperture illumination efficiency (η_{A}) barely appears in literature with this designation, the main reason being that η_{A} may be considered as a ”meta”-loss, a set of multiple losses. Such loss is composed by the transmitter efficiency factor or transmitter gain efficiency (g_{T}) and the Strehl loss or wave-front loss (L_{SR}). Anyway, the expressions concerning this term found in opticalcoms reference books are equivalent after carrying out some algebra. Finally it must be noticed that such efficiency only accounts for the transmitter (Tx).

$$\eta_{\mathrm{A}} = g_{\mathrm{T}} \cdot L_{\mathrm{SR}} \tag{10}$$

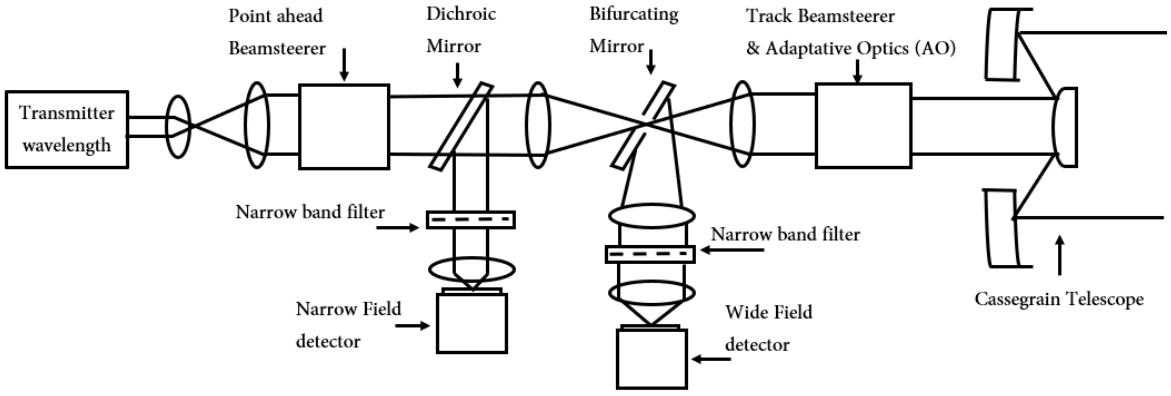

Figure 3.4: Laser beam routing through a general OMA for a transceiver. Adapted from [5].

3.2.1 Antenna transmitter efficiency factor (g_T)

The antenna transmitter efficiency factor also known as gain efficiency accounts for obscuration, truncation, off-axis intensity, near field and deforming effects, it is given by [46]:

$$g_{\mathrm{T}}(\alpha,\beta,\gamma,X) = 2\alpha^2 \left| \int_{\gamma^2}^{1} e^{j\beta u} e^{-\alpha^2 u} J_0(X\sqrt{u}) du \right|^2 \tag{11}$$

where $J_0(\cdot)$ is the Bessel function of order 0, note that if $X = 0$ then $J_0(0) = 1$; α (beam width ratio), β , γ (obscuration ratio), X are the following dimensionless parameters;

$$\left.\begin{array}{rcc} \alpha & = & a/\omega \\ \gamma & = & b/a \\ X & = & k\, a\, sin\theta_1 \\ \beta & = & k\, a^2/2\ [1/r + 1/R] \end{array}\right\} \tag{12}$$

Being a and b the radius of the primary and secondary mirrors respectively (observe figure 3.5). ω is the $1/e^2$ radius of the Gaussian beam coupled to the telescope optics. k is the wave-number $k = 2\pi/\lambda$. r and θ_1 are the observation points. R is the radius of curvature of the beam front at the telescope aperture plane.

A particular but accurate equation is obtained considering:

- $X = 0$ for the on-axis antenna efficiency for incident Gaussian energy
- Taking into account the far field and allowing Gaussian amplitude plane waves $\beta \equiv 0$ to impinge on the aperture.

Equation 11 becomes,

$$g_{\mathrm{T}}(\alpha,0,\gamma,0) = \frac{2}{\alpha^2}[e^{-\alpha^2} - e^{-\gamma^2\alpha^2}]^2 \tag{13}$$

$$\frac{d}{d\alpha}\left[g_{\mathrm{T}}(\alpha,0,\gamma,0)\right] = 0 \rightarrow \alpha \approx 1.12 - 1.30\gamma^2 + 2.12\gamma^4 \ (\text{optimum}) \tag{14}$$

Equation 14 gives the optimum aperture to beamwidth ratio for a general obscuration and is accurate to within $\pm 1\%$ for $\gamma < 0.4$.

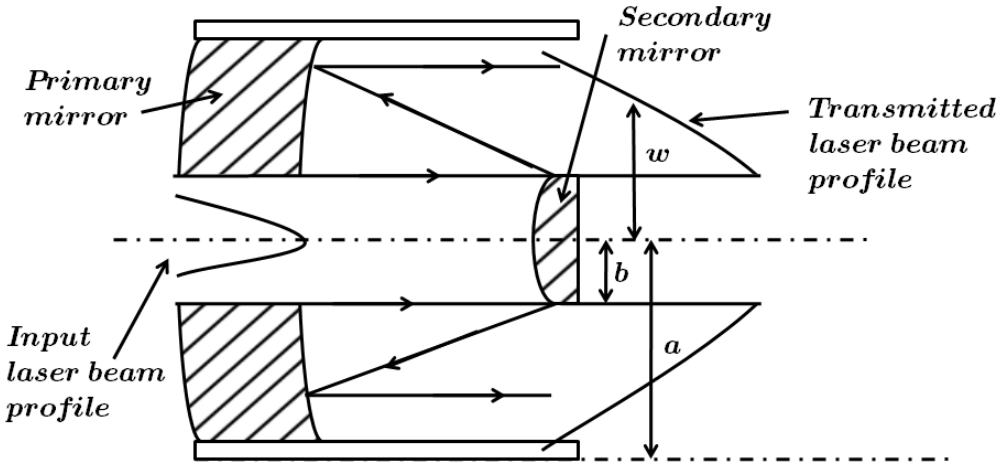

Figure 3.5: Cassegrain geometry telescope and Gaussian beam profile relationship. Black arrows indicate the laser beam in transmitting direction.

Equation13, is plotted in Figure 3.6 for a number of different obscuration ratios. Even for an unobscured aperture, the theoretical maximum gain is reduced due to truncation (if $\gamma = 0$ then optimum $\alpha = 1.12$).

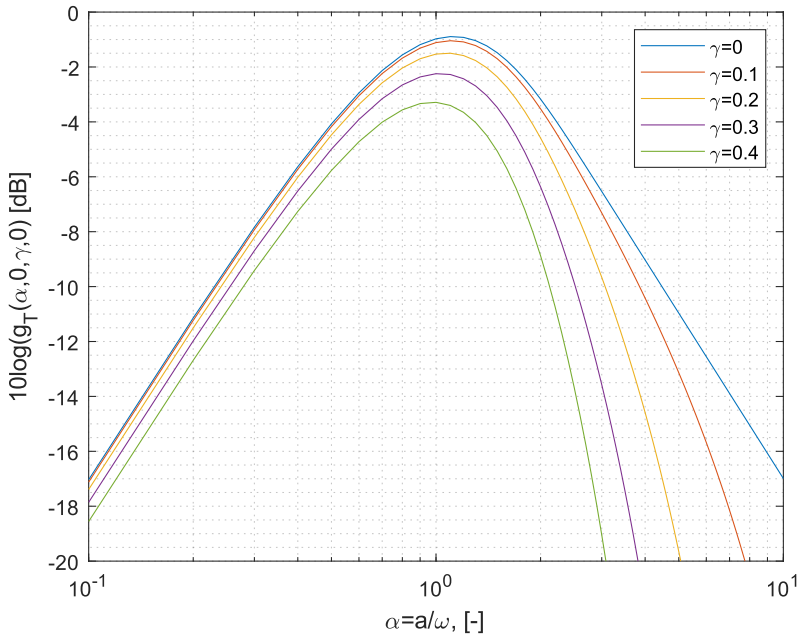

Figure 3.6: Antenna transmitter efficiency factor g_{T} as function of α for five different obscuration ratios (γ).

To conclude, the antenna transmitter efficiency factor is defined by the telescope geometry. Data from Table Mountain facility is extracted from a similar study [47] in which such observatory is analysed.

Observatory	**Diameter (D)**	**Obscuration (γ)**	α_{opt}	$10\log(g_{\text{T}}(\alpha, 0, \gamma, 0))$
Table Mountain	1 m	0.2	1.07	-1.5 dB

Table 3.1: $g_{\text{T}}(\alpha_{\text{opt}}, 0, \gamma, 0)$ from Table mountain facility.

3.2.2 Strehl loss (L_{SR})

In reality, no lens or surfaces are conceived with perfect geometry, therefore any time a laser beam encounters a surface or a lens it does not propagate in an ideal way; the main consequence of this phenomenon is the decay of the expected intensity with respect to an ideal case where non aberration is present.

The Strehl Ratio is defined as the intensity at the centre of the aberrant system to that of an ideal optical system. The Strehl ratio, and therefore the Strehl loss (L_{SR}) (a.k.a wavefront loss) is given by:

$$SR = e^{-(k\sigma)^2} \tag{15}$$

$$L_{\text{SR}} = 10\log(\text{SR}) \tag{16}$$

Being $k = 2\pi/\lambda$ and σ is the root mean square (RMS) optical path difference (a.k.a wavefront error, WFE).

$$\sigma = \sqrt{\frac{\sum_{i=1}^{n} x_i^2}{n}} \tag{17}$$

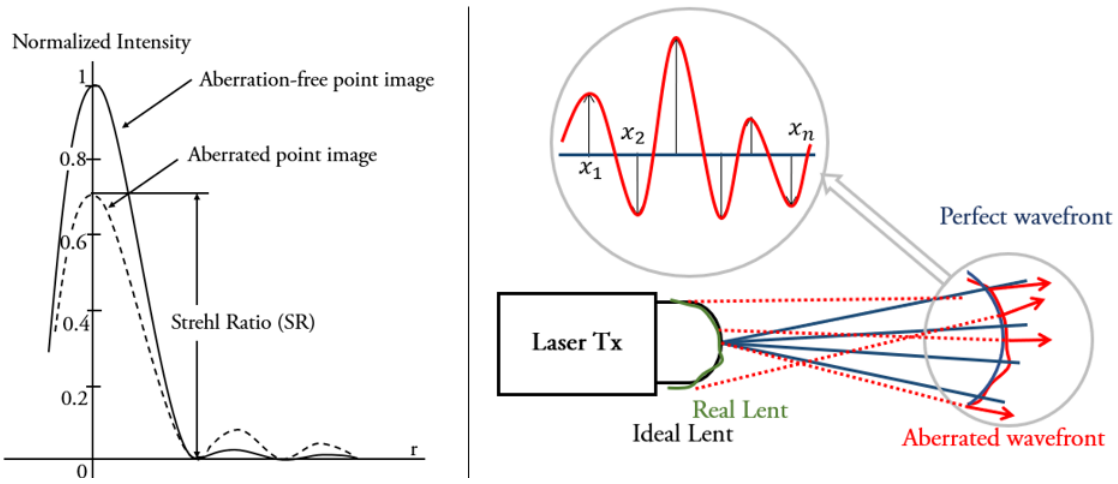

Figure 3.7: On the left, beam intensity 2D view along its radius and Strehl Ratio [6]. On the right, RMS schematic.[Own work]

For smooth optics, σ is approximately 28% of the peak-to-valley differences. The WFE is represented as λ/x', $x' =$ WFE. As [5] indicates, most laser communication systems operate with $\sigma = \lambda/10$, which is the value that is taken into account for obtaining the Strehl loss in the present work.

$$\sigma = \lambda/10 \tag{18}$$

$$\mathrm{SR} = e^{-(\frac{2\pi\sigma}{\lambda})^2} = e^{-(\frac{2\pi\lambda}{\lambda 10})^2} = 0.673 \tag{19}$$

$$L_{\mathrm{SR}}(\mathrm{dB}) = 10\log(0.673) = -1.71\ \mathrm{dB} \tag{20}$$

For any other WFE observe figure 3.8. To conclude, it might be find in literature alternate higher order approximations for the SR, the expression presented becomes inaccurate as RMS WFE becomes larger than ($> \lambda/4$); therefore the expression is valid for opticalcom ($\sim \lambda/10$).

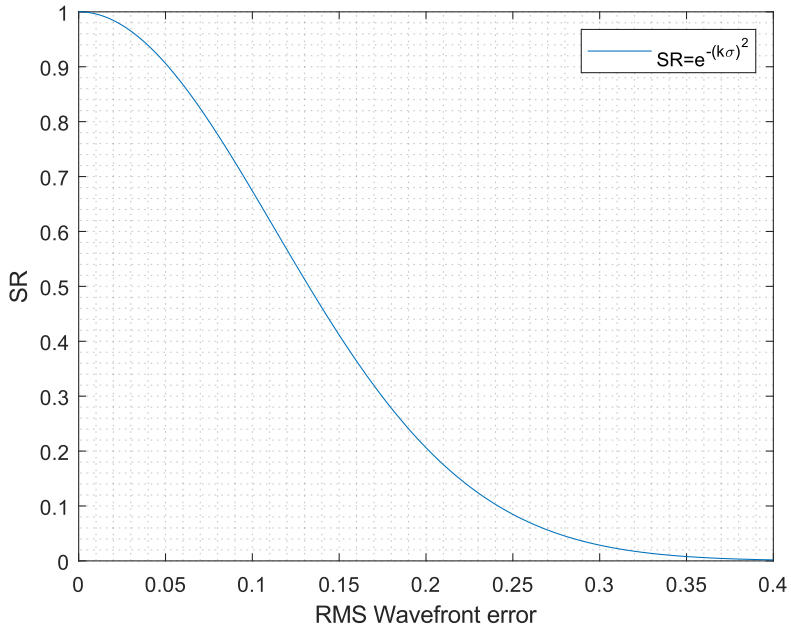

Figure 3.8: Strehl ratio as a function of RMS WFE.

3.3 Transmitter/Receiver pointing loss efficiencies (η_{TP}, η_{RP})

In section 3.2.1, on-axis transmitter gain was determined. However, any laser beam mispointing causing the receiver to be located off-centre from the far-field irradiance profile will result in a decrease in that gain; this decrease can be measured in terms of the off-axis gain.

In practice, a transmitter and a receiver will never be perfectly aligned, consequently pointing losses will arise, keeping the narrow-angular-width laser beam pointed in the presence of spacecraft attitude and vibration disturbances (jitter) becomes a formidable challenge.

Therefore, in determining a link budget, some losses are allocated to mispointing in terms of efficiencies η_{TP} and η_{RP} (see Eq. 4).

By establishing $X = k\,a\,\sin\theta_1$ in Eq.11 it is observed the effect mispointing at different angles.(see figure 3.9).

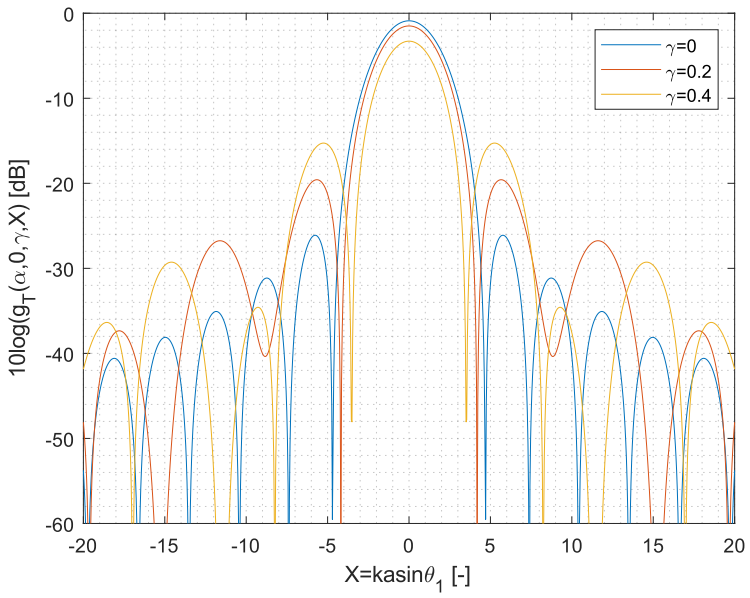

Figure 3.9: Far-field ($\beta = 0$) transmitter antenna efficiency factor in dB relative to a transmitter antenna gain as a function of the angle θ_1, from the optical axis of the antenna.

The pointing loss of an optical link vary as function of the transmitter antenna diameter and the laser wavelength. In order to exemplify the pointing loss with real data it is considered the flight terminal transceiver from the *Psyche* mission targeted to be launched in summer 2022. *Psyche* S/C transceiver is equipped with a Gregorian telescope design, see Figure 3.10. Hence, for the calculations presented afterwards the design has been treated, approximately, as a Cassegrain geometry with obscuration ratio $\gamma = 0$.

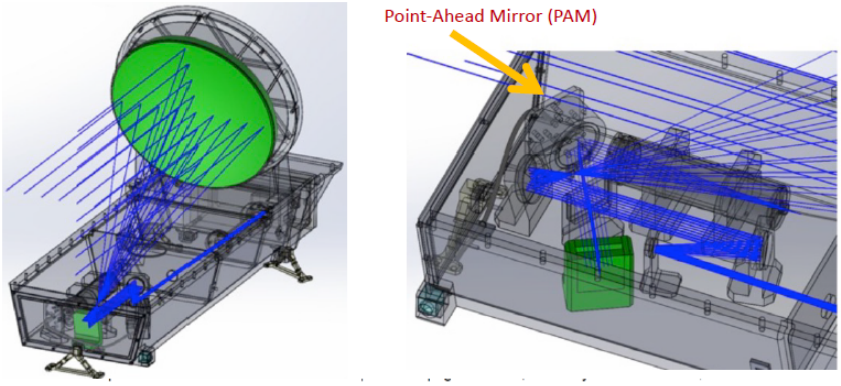

Figure 3.10: On the left, *Psyche* flight transceiver, primary mirror diameter of 22cm following a Gregorian telescope design. On the right, the transceiver to telescope routing. [7, 8]

Psyche optical antenna's aperture diameter measures $D_{\text{rx}} = 22$ cm and for downlink communication operates at $\lambda = 1550$ nm. Its gain as function of the off-axis angle θ_1 can be determined as follows:

knowing that,

$$G'_{\text{Tx}}(\text{dB}) = 10\log\left[G_{\text{Tx}} \cdot g_{\text{T}}\right] = 10\log\left[\left(\frac{\pi D_{\text{Tx}}}{\lambda}\right)^2 \cdot g_{\text{T}}\right] \tag{21}$$

$$X = k\,a\,\sin\theta_1 \rightarrow \theta_1 = \arcsin\left(\frac{X\lambda}{\pi D_{\text{Tx}}}\right) \tag{22}$$

The resulting plot is shown in Figure 3.11. Note that multiple gains are plotted considering different obscuration ratios in order to see the effect that provokes an antenna geometry which secondary mirror in the midst of the primary.

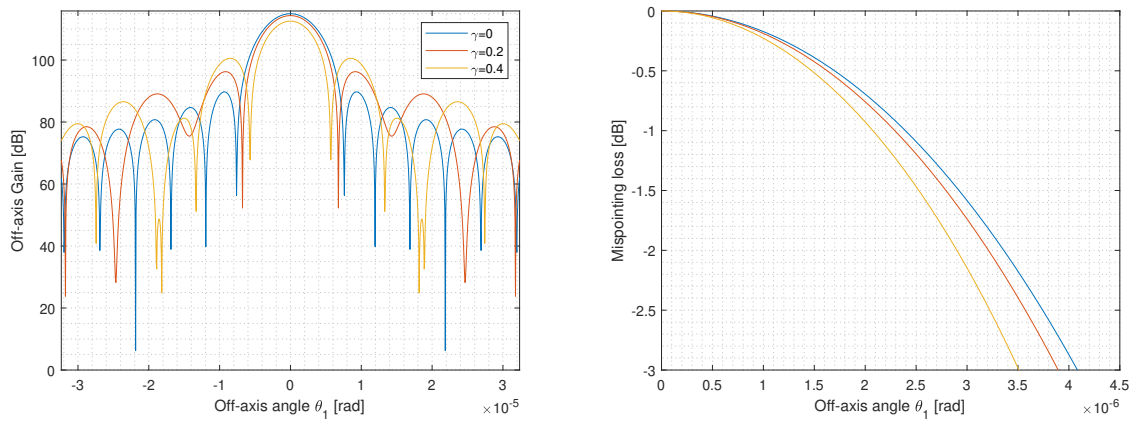

(a) (b)

Figure 3.11: (a) G'_{Tx} as function of the mispointing angle θ_1 at different obscuration ratios, for a downlink communication with $\lambda = 1550$ nm and the flight terminal transmitter antenna having a $D_{\text{Tx}} = 22$ cm. (b) Mispointing loss $g_{\text{T}} - max(g_{\text{T}})$ [dB] as function the mispointing angle θ_1 at different obscuration ratios. Same parameters as case (a).

For *Psyche* downlink, case $\gamma = 0$ from Figure 3.11, it must be noticed that a deviation of 4.1μrad from the on-axis gain can produce a pointing loss of ~ 3 dB, such losses are not insignificant at all and must be taken into account in the link budget. By knowing the operating wavelength, λ, and the diameter of the transmitting antenna, D_{Tx}, one can follow the previous procedure to find the mispointing loss given the accuracy of the transmitter. In other words if a value of 2 dB mispointig loss is assumed to be the maximum loss –for the *Psyche* downlink, case $\gamma = 0$ from Figure 3.11– then the pointing mechanism must ensure an angle deviation interval ranging from $0\,\mu$rad to $\sim 3.36\,\mu$rad.

However, angular pointing error, θ_1, is continuously changing due to non controllable phenomena such as jitter. For this reason, it turns out applicable an statistical approach for the

behaviour of θ_1 that can be described mathematically and represents the performance of the utilised pointing mechanisms. As reported in [47, 48] the probability distribution function for pointing errors can be expressed as the Rice probability density function (Eq. 23):

$$f(x|\nu,\sigma_{RD}) = \frac{x}{\sigma_{RD}^2}\exp\left[\frac{-(x^2+\nu^2)}{2\sigma_{RD}^2}\right] I_0\left(\frac{x\nu}{\sigma_{RD}^2}\right) \tag{23}$$

Where $I_0(\cdot)$ is the modified Bessel function of the first kind with order zero. ν is the mean of the variable x and σ_{RD} is the variance of x. So, if the x variable becomes the angular pointing error θ_1 the Rice probability density function becomes:

$$f(\theta_1|\chi_{\mathrm{Tx}},\vartheta_{\mathrm{Tx}}) = \frac{\theta_1}{\vartheta_{\mathrm{Tx}}^2}\exp\left[\frac{-(\theta_1^2+\chi_{\mathrm{Tx}}^2)}{2\vartheta_{\mathrm{Tx}}^2}\right] I_0\left(\frac{\theta_1\chi_{\mathrm{Tx}}}{\vartheta_{\mathrm{Tx}}^2}\right) \tag{24}$$

For small error angles, θ_1 can be expressed as two orthogonal components $\theta_{1\mathrm{x}}$ and $\theta_{1\mathrm{y}}$ such that $\theta_1 = \sqrt{\theta_{1\mathrm{x}}^2+\theta_{1\mathrm{y}}^2}$. Considering θ_{1x}^2 and θ_{1y}^2 as independent Gaussian random variables with means χ_{x} and χ_{y} and variances $\vartheta_{\mathrm{x}}^2 = \vartheta_{\mathrm{y}}^2 = \vartheta_{\mathrm{Tx}}^2$. Where ϑ^2 is a measure of jitter in the pointing mechanism, and $\chi_{\mathrm{Tx}} = \sqrt{\chi_{\mathrm{x}}^2+\chi_{\mathrm{y}}^2}$ is a measure of pointing error due to a constant bias in pointing accuracy. For example, choosing χ_{Tx} and ϑ_{Tx} a 25% of the mispointing angle at 2 dB in [μrad] for the current link yields the probability distribution function shown in Figure 3.12.

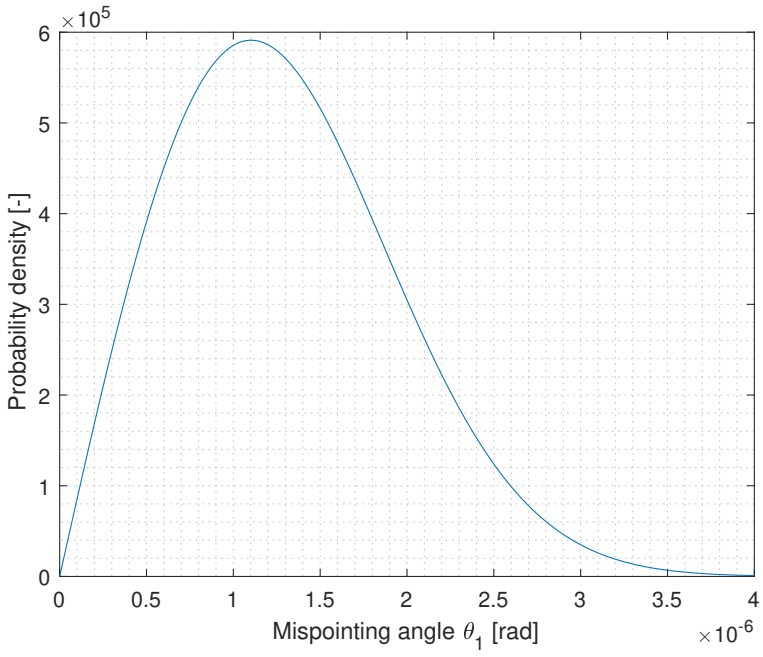

Figure 3.12: PDF as a function of the mispointing angle for a fixed bias and rms jitter that is 25 percent of the mispointing angle required for a 2 dB loss.

Consider that, by design or estimation, some critical error angle (δ) is known that cannot be exceeded without causing a communication error. For *Psyche* case, a condition of 2 dB

fading was arbitrarily considered to be the outage limit, which led to a mispointing angle of $\theta_1 = 3.36\,\mu$rad. For any other case, if the maximum mispointing angle would be exceeded, then, the power level of the received signal will fade too low for detection. This event is named a pointing induced fade (PIF) [49] and is described as follows:

$$\mathrm{PIF}(\theta_1 \geq \delta) = \int_{\delta}^{\infty} f(\theta_1|\chi_{\mathrm{Tx}}, \vartheta_{\mathrm{Tx}}) d\theta_1 \tag{25}$$

For *Psyche* downlink, Eq. 25 yields a corresponding PIF of 0.0029 or 0.29%. So, provided the pointing bias and jitter can be held within the allocation, then 99.71% of the time the beam will be pointed in a manner that will result in ≤ 2 dB loss.

Despite a mispointing losses computation procedure have already been explained, in the link power budget equation (Equation 4), the contribution of pointing losses has account for in terms of η_{TP} and η_{RP} efficiencies , the transmitter pointing loss and the receiver truncation factors or efficiencies. Generally, the mean value of the first factor [43, 48] is considered and is given by:

$$\eta_{\mathrm{TP}} = \int_{0}^{\infty} \eta_{\mathrm{TP}}(\theta_1) f(\theta_1|\chi_{\mathrm{Tx}}, \vartheta_{\mathrm{Tx}})\, d\theta_1 \tag{26}$$

Where $\eta_{\mathrm{TP}}(\theta_1)$ is the instantaneous pointing loss as function of off-axis pointing angle, θ_1 and can be defined as a Taylor series approximation;

$$\eta_{\mathrm{TP}}(\theta_1) \cong \frac{1}{f_0^2(\gamma_{\mathrm{tx}})} \left[f_0(\gamma_{\mathrm{tx}}) + \frac{f_2(\gamma_{\mathrm{tx}})}{2!} x^2 + \frac{f_4(\gamma_{\mathrm{tx}})}{4!} x^4 + \frac{f_6(\gamma_{\mathrm{tx}})}{6!} x^6 \right] \tag{27}$$

Where $x = \pi(D_{\mathrm{Tx}}/\lambda)\theta_1$ and the coefficients f_0, f_2, f_4, f_6 are given for several values of γ in the following table [50];

Transmitter Obscuration ratio, γ	f_0	f_1	f_4	f_6
0	0.569797	-0.11342	0.0503535	-0.0292921
0.1	0.566373	-0.115327	0.0513655	-0.0299359
0.2	0.555645	-0.120457	0.0542465	-0.0317773
0.3	0.535571	-0.126992	0.0584271	-0.0344978
0.4	0.50138	-0.131777	0.0626752	-0.0374276

Table 3.2: Values for the Coefficients in the Series Approximation to the Pointing Loss. (Given by Equation 27).

Finally, for *Psyche* downlink, once substituted all the previously mentioned values into Eq 26 it results a transmitter pointing efficiency of $\eta_{\mathrm{TP}} = 0.9213$. For further details refer to the *Annex. Code*.

The same procedure applies for the receiver, therefore, the receiver efficiency is defined as:

$$\eta_{\mathrm{RP}} = \int_0^{\infty} \eta_{\mathrm{RP}}(\theta_1) f(\theta_1 | \chi_{\mathrm{Rx}}, \vartheta_{\mathrm{Rx}}) d\theta_1 \tag{28}$$

Where $\eta_{\mathrm{RP}}(\theta_1)$ is the instantaneous detector truncation loss as a function of off-axis pointing error, given by:

$$\begin{aligned} \eta_{\mathrm{RP}}(\theta_1) = \frac{2}{1-\gamma_{\mathrm{rx}}} \int_0^{2\pi} \int_0^{\Omega_{FOV}} \Bigg[J_1 \left(\pi \frac{D_{\mathrm{Rx}}}{\lambda} \sqrt{\theta_1^2 + \kappa^2 - 2\theta_1 \kappa cos\Psi} \right) - \\ \gamma_{\mathrm{rx}} J_1 \left(\pi \frac{\gamma_{\mathrm{rx}} D_{\mathrm{Rx}}}{\lambda} \sqrt{\theta_1^2 + \kappa^2 - 2\theta_1 \kappa cos\Psi} \right) \Bigg]^2 \frac{d\kappa}{\kappa} d\Psi \end{aligned} \tag{29}$$

where Ω_{FOV} is the receiver field-of-view or solid angle viewed by the detector, γ_{rx} is the receiver obscuration ratio, and $J_1(\cdot)$ is the Bessel function of order one. Calculation of $\eta_{\mathrm{RP}}(\theta_1)$ using Equations 28 and 29 is rather difficult, requiring computation of a triple numerical integral. As a result, it is often assumed that $\eta_{\mathrm{RP}} = 1$. Realistically, η_{RP} is 1 only in cases where no attempt is made to optimise background light rejection [43]. In other cases η_{RP} is in the range $0.5 < \eta_{\mathrm{RP}} < 1$.

3.4 Atmosphere losses (L_{atm})

Air molecules can absorb, scatter, diffract and wander the laser beam. The main losses are caused due to atmospheric absorption and light scintillation, so the atmospheric losses term from Equation 4 becomes:

$$L_{\mathrm{atm}} = L_{\mathrm{trans}} \cdot L_{\mathrm{turb}} \tag{30}$$

Now, we analyse both terms.

3.4.1 Atmospheric transmittance loss (L_{trans})

According to the International telecommunication Union (ITU) report Rep ITU-R F.2106-1 [51], the signal under clear-sky weather conditions is attenuated because of extinction caused by air molecules and aerosols. In addition, if signal passes through adverse weather conditions, it contributes to increase the attenuation. The transmittance (T) of laser radiation that has propagated over a distance (R) is described by the Beer–Lambert relation:

$$T(\lambda, R) = \frac{P_{\mathrm{Rx}}}{P_{\mathrm{Tx}}} = e^{-\alpha_{\mathrm{e}}(\lambda) \cdot R} \tag{31}$$

where;

- T is the transmittance at distance R [km] of the transmitter.
- $\alpha_{\mathrm{e}}(\lambda)$ is the extinction coefficient per unit of length [km^{-1}]

- P_{Rx} refers to the received power which is equivalent to the transmitted power at distance R, and is equivalent to $P_{\mathrm{Tx}}(\lambda, R)$
- P_{Tx} refers to the transmitted power $P_{\mathrm{Tx}}(\lambda, 0)$

The extinction coefficient is the sum of two terms:

$$\alpha_{\mathrm{e}}(\lambda) = \alpha_{\mathrm{clear\_air}}(\lambda) + \alpha_{\mathrm{excess}}(\lambda) \tag{32}$$

where;

- $\alpha_{\mathrm{clear\_air}}$ is the specific attenuation under clear air (due to the presence of gaseous molecules)
- α_{excess} is the specific attenuation due to the occasional presence of fog, mist, haze, drizzle, rain, snow, hail, etc. It is not considered owing to 0act that laser communications are not prone to be utilised with adverse weather.

$$\alpha_{\mathrm{clear\_air}}(\lambda) = \alpha_{\mathrm{m}}(\lambda) + \alpha_{\mathrm{a}}(\lambda) + \beta_{\mathrm{m}}(\lambda) + \beta_{\mathrm{a}}(\lambda) \tag{33}$$

where

- $\alpha_{\mathrm{m}}(\lambda)$ is the molecular absorption coefficient (N_2, O_2, H_2, OH, CO_2, O_3, ...)
- $\alpha_{\mathrm{a}}(\lambda)$ is the absorption coefficient by the aerosols (small solid or liquid particles present in the atmosphere like ice, dust, smoke...)
- $\beta_{\mathrm{m}}(\lambda)$ is the Rayleigh scattering coefficient resulting from the interaction of the wave with particles (molecular gas) of a smaller size than the wavelength
- $\beta_{\mathrm{a}}(\lambda)$ is the Mie scattering coefficient. It appears when particles (aerosols) are of the same order of magnitude as the transmitted wavelength.

Rayleigh scattering	**Mie scattering**	**Non-selective or geometrical scattering**
$r \ll \lambda$	$r \sim \lambda$	$r \gg \lambda$
Air molecules Haze	Haze Fog Aerosols	Fog, Rain, Snow, Hail

Table 3.3: Scattering regimes depending on the scatterer's size r with respect to the transmission laser wavelength λ.

A priori, the atmospheric extinction $\alpha_{\mathrm{e}}(\lambda)$ can be computed by determining the exact composition of the atmosphere over the path of interest and employing the physics of molecular and aerosol extinction as well as Earth observation techniques [52]. In the literature, multiple semi-empirical models can be found to compute such coefficients (For instance the model

presented at ITU-R P.1622 [53] which allows to compute the Mie scattering coefficient, $\beta_{\mathrm{a}}(\lambda)$ and the Rayleigh scattering coefficient $\beta_{\mathrm{m}}(\lambda)$). However, because of the wide variations in weather conditions and sparsity of data on some atmospheric constituents, it is desirable to have an engineering approach to atmospheric modeling to obtain α_{m}, α_{a}, β_{m}, and β_{a} coefficients.

To deal with these complex phenomena, the Phillips Laboratory of the Geophysics Directorate at Hanscom Air Force Base, Massachusetts, developed software to predict transmittance/radiance effects for varying conditions. One of the first software programs describing the atmospheric effects on a laser beam was LOWTRAN (acronym for LOW resolution atmosphere TRANsmission). Afterwards, an improved version called MODTRAN (acronym for MODerate atmospheric TRANsmission) was developed, allowing a narrower spectral resolution up to 0.2 cm^{-1}. However, the requirement to properly model the propagation of laser beam with a narrow linewidth in the sub-angstrom range has inspired the development of software programs such as FASCODE (acronym for FASt atmospheric Signature CODE) which is based on the high-resolution molecular absorption database, HITRAN.

For instance, in [54] LOWTRAN is used to support the study whereas in [24] it is employed MODTRAN. In figure 3.13, similarly to the previously mentioned studies, the atmospheric transmittance through a vertical laser path along wavelength spectrum have been obtained, in this case by means of the MODTRAN Web Application [28], which is available online and allows to configure multiple inputs.

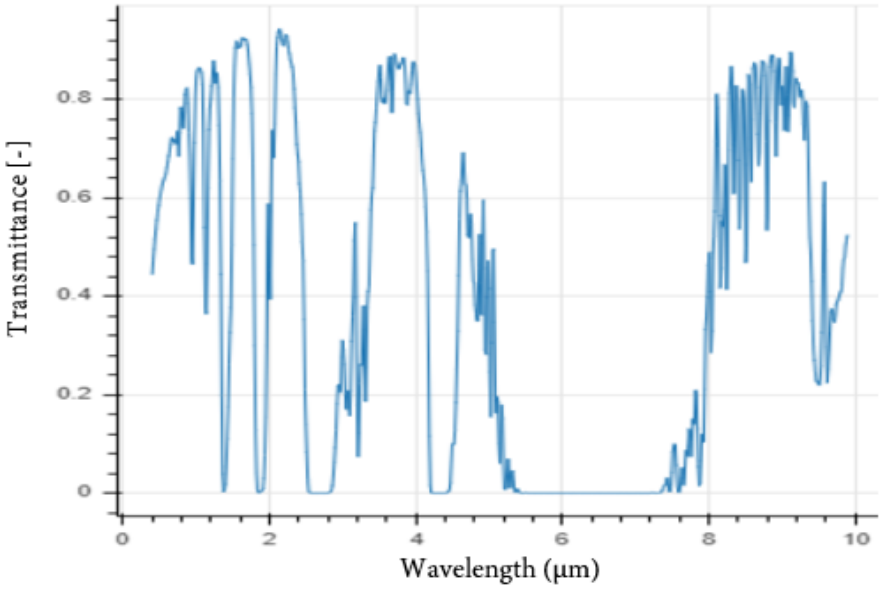

Figure 3.13: Atmospheric transmittance in an Earth-to-space path at zenith ($R = 100$ km). A rural aerosol composition with a surface visual range of 23 km and US Atmosphere standard 1976 model is considered. The data refers to the case of an observer located at elevations sea level (SL), and considering the shortest (vertical) ground-to-space path at the zenith.

By analysing the transmittance curve from figure 3.13 some essential laser wavelengths suitable for communication purposes as well as their transmittance are shown in Table 3.4. Note that atmospheric transmittance loss can be computed as follows:

$$L_{\text{trans}} = 10\log[T(\lambda, R)] \tag{34}$$

Laser	λ**[nm]**	**Transmittance**	L_{trans} **[dB]**
Dye, Ti:Saphire	670	0.72	-1.42
Solid, Nd:YAG	1064	0.92	-0.36
Solid: Nd:YLF	1313	0.67	-1.73
SemiConductor: InGaAsP	1550	0.92	-0.36
Solid, Tm, Ho:YAG	2019	0.83	-0.80

Table 3.4: Transmittance loss for relevant lasers wavelength

The atmospheric loss might be mitigated by settling the OGS at higher altitudes than SL, at $\sim$ 2 km the typical attenuation for Space-Earth link, considering $\lambda = 1064$ or 1550 nm (near-infrared) at zenith would be 0.1—0.3 dB.

3.4.1.1 Atmospheric transmittance loss (L_{trans}) (Constrained method)

As stated in section 3.4.1, the dynamic nature of the atmosphere nature forces us to make use of databases in which atmospheric constituents properties are stored as a function of its height and the geographic Earth region, among other factors. Nevertheless, by making some assumptions one can determine the extinction coefficient α_{e} in a simplified way.

First of all, it is well known that Rayleigh scattering β_{m} is negligible for systems operating below 375 THz [53], that is, above 800 nm. As shown in table 3.4, suitable wavelength candidates are $\lambda = 1064$ nm and $\lambda = 1550$ nm. So, if these wavelengths are used then β_{m}=0; consequently, by choosing these specific wavelength the transmittance values are high enough to assume that absorbance coefficients α_{m} and α_{a} are $\sim$ 0 (observe similar assumptions in [55]). Therefore, equation 32 turns out

$$\alpha_{\text{clear\_air}}(\lambda) = \beta_{\text{a}}(\lambda) \tag{35}$$

ITU-R P.1622 [53] suggest a method to obtain β_{a} when local measurements characterising the atmosphere are not available. The method described can be used for calculating attenuation due to scattering along Earth-space paths. Considering wavelength; λ [μm], the height of the earth station above mean sea level h_0 [km] and the elevation angle θ [deg]

$$a = -0.000545\lambda^2 + 0.002\lambda - 0.0038 \tag{36}$$
$$b = 0.006628\lambda^2 - 0.0232\lambda + 0.0439 \tag{37}$$
$$c = -0.028\lambda^2 + 0.101\lambda - 0.18 \tag{38}$$
$$d = -0.228\lambda^3 + 0.922\lambda^2 - 1.26\lambda + 0.719 \tag{39}$$

The Mie scattering coefficient and therefore the extinction coefficient from $h_0 \to \infty$

$$\beta_{\mathrm{a}} = a \cdot h_0^3 + b \cdot h_0^2 + c \cdot h_0 + d \tag{40}$$

$$L_{\mathrm{trans}} = \frac{4.3429\,\beta_{\mathrm{a}}}{\sin\theta} \tag{41}$$

The method is appropriate for earth stations located at altitudes between 0 and 5 km above sea level and between 150 THz and 375 THz. It is accurate to within approximately 0.1 dB assuming elevation angles above 45°. However, local atmospheric conditions may lead to several dBs of

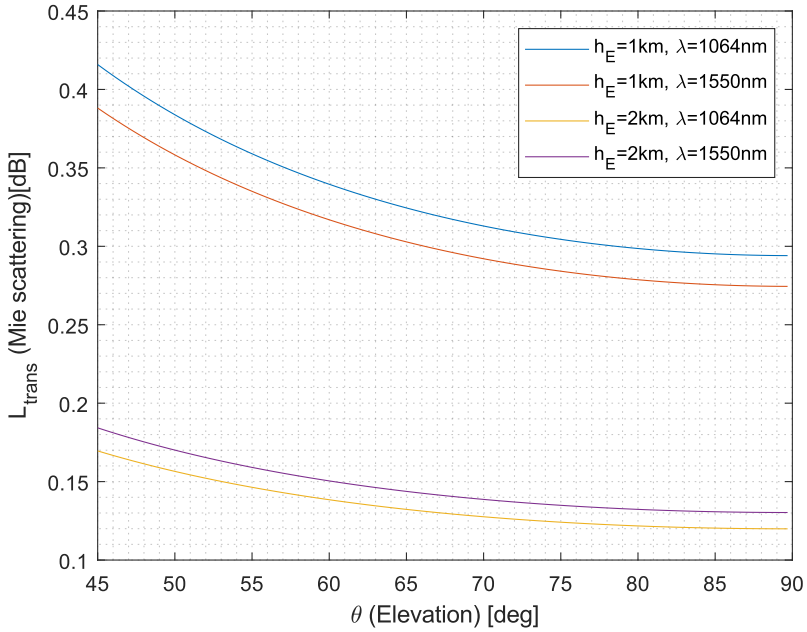

Figure 3.14: Atmospheric transmittance loss considering $\alpha_{\mathrm{clear\_air}} = \beta_{\mathrm{a}}(\lambda)$ from ground stations height ($h_E = 1km$, $h_E = 2km$) (ITU-R P.1622 recommendation)

3.4.2 Atmospheric turbulence/scintillation loss (L_{turb})

Turbulence is fundamentally a nonlinear process as described by the governing Navier-Stokes equations, and is a largely unsolved problem. Because of mathematical difficulties in solving these equations, Kolmogorov developed a statistical theory of turbulence that relies heavily on dimensional analysis and additional simplifications and approximations. Thus, turbulence

theory used to model laser beam behaviour through the atmosphere is not derived from first principles.

Winds, which are produced when solar radiation warms up the atmosphere in addition with Earth rotation and terrain orography variation, contribute in mixing moisture and smooth air temperature gradients. Such phenomena create irregularities in the refractive index of the atmosphere (a.k.a index-of-refraction turbulence, IRT) in the form of eddies, or cells, called optical turbules. A way to characterise such fluctuations of the atmosphere's refractive index is done through the modelling of the index of refraction structure constant (C_n^2); these fluctuations are responsible for random variations in the signal carrying laser beam intensity (irradiance) called scintillation.

Other effects are also caused by the atmosphere such as wavefront distortions, beam broadening caused by diffraction, beam wandering and Rx angle of arrival fluctuations that result in random signal losses at the Rx and increase the signal bit error rate (BER) due to signal fading. As shown in figure 3.15 randomly distributed cells are formed under the influence of thermal gradients inside the propagation medium; then, the wave fronts vary causing the focusing and defocusing of the beam. Theoretical and experimental studies of irradiance fluctuations generally centre around the scintillation index (normalised variance of irradiance fluctuations) defined by:

$$\sigma_I^2 = \frac{< I^2 > - < I >^2}{< I >^2} = \frac{< I^2 >}{< I >^2} - 1 \tag{42}$$

where the quantity I denotes irradiance in [W/m^2] of the optical wave and the angle brackets $<>$ denote an ensemble average or, equivalently, a long-time average.

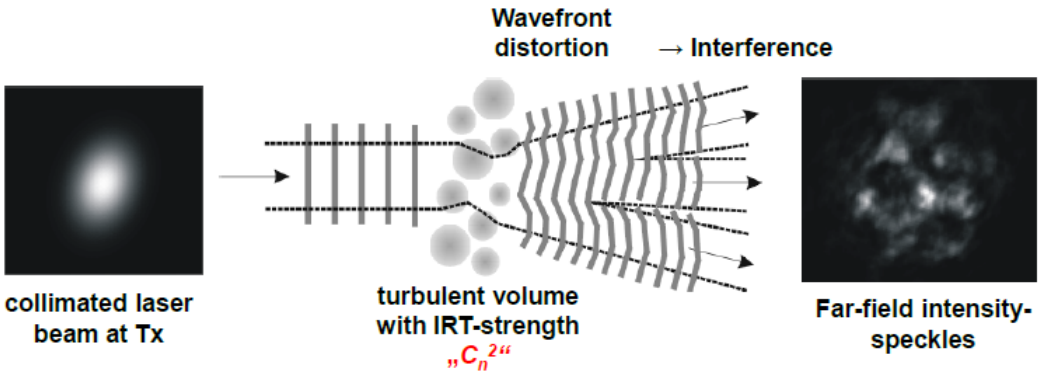

Figure 3.15: Far field intensity speckles caused by wavefront distortions due to atmospherics turbules. [9]

The scintillation index (σ_I^2) is used as a measure of scintillation and can be analysed using extended Rytov theory [56]. As turbulence is yet an unsolved problem, we can find in the literature multiple models to compute the scintillation index. In this thesis, Andrews *et al.* general theory for downlink scintillation under weak and strong fluctuations [56–58] has

been applied. The model is valid only for electromagnetic plane wave at any zenith angles $0° \leq \varphi \leq 90°$ and is defined by:

$$\sigma_{\mathrm{I}}^2 = exp\left[\frac{0.49\sigma_1^2}{(1+1.11\sigma_1^{12/5})^{7/6}} + \frac{0.51\sigma_1^2}{(1+0.69\sigma_1^{12/5})^{5/6}}\right] - 1 \tag{43}$$

where,

$$\sigma_1^2 = 2.25\mu_{pl}k^{7/6}(H-h_0)^{5/6}sec^{11/6}(\varphi) \tag{44}$$

$$\mu_{pl} = \int_{h0}^{H} C_n^2(h)\xi^{5/6}dh \tag{45}$$

and ξ is the normalised distance variable;

$$\xi = \frac{h-h_0}{H-h_0} \tag{46}$$

$k = (2\pi/\lambda)$ is the wavenumber in [rad/μm], h_0 is the height of earth station above sea level [m], H is the altitude of the satellite in [m], in [58] H value is set to LEO and GEO orbits, and as a the model is validated for such orbits, it will be assumed that an error is being made as the probes are travelling through deep space. The above (σ_{I}^2) expression (43) applies well to the downlink communications.

For applications involving propagation along a horizontal path, it is customary to assume the structure parameter $C_n^2(h)$ remains essentially constant. Propagation along a vertical or slant path, however, requires a $C_n^2(h)$ profile model to describe properly the varying strength of optical turbulence as a function of altitude h. Several $C_n^2(h)$ profile models, including both day and night models, are used by the technical community for ground-to-space or space-to-ground applications. One of the most widely used models is the Hufnagel-Valley (HV) [59] heuristic model described by

$$C_n^2 = 0.00594\left(\frac{w}{27}\right)^2\left(10^{-5}h\right)^{10}e^{\frac{-h}{1000}} + 2.7\times10^{-16}e^{\frac{-h}{1500}} + Ae^{\frac{-h}{1000}} \tag{47}$$

where h is the height [m], w is the rms wind speed (pseudowind) [m/s] between 5 km and 20 km of height. A is a parameter that is usually set equal to $1.7\times10^{-14}\,\mathrm{m}^{-2/3}$. The turbulence strength is usually changed by a variation of the w term. For HV_{21} model $w = 21$ m/s and A takes the previously mentioned value. This model is referred as $HV_{5/7}$ if the coherence diameter (a.k.a as Fried parameter) is set to $r_0 \sim 5$ cm and the isoplanatic angle $\theta_0 = 7\mu$rad. For the 5/7 model, the parameters assume values of $A = 1.7\times10^{-14}\,\mathrm{m}^{-2/3}$ and $w = 21$ m/s.

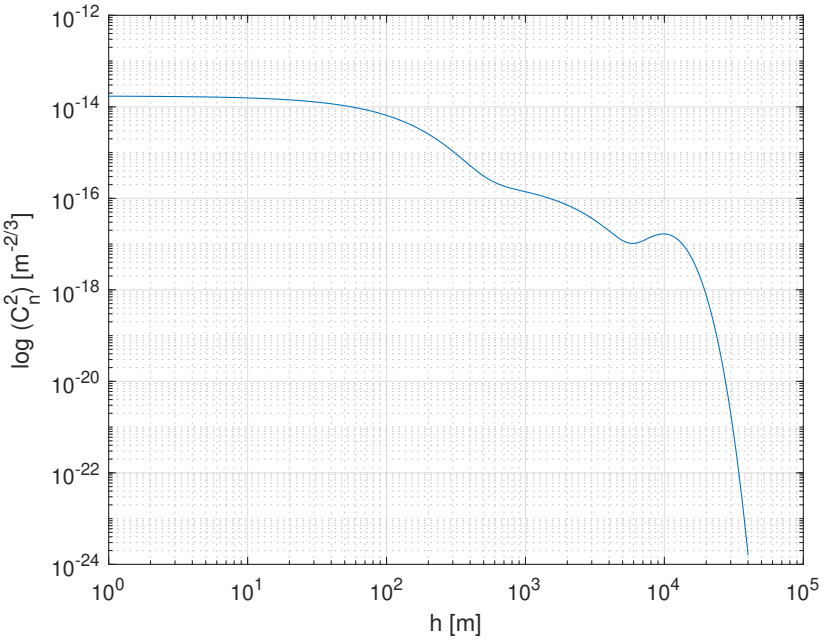

Figure 3.16: C_n^2 as a function of height above ground h according to the Hufnagel-Valley H-V5/7-model. $A = 1.7 \times 10^{-14}\,\mathrm{m}^{-2/3}$.

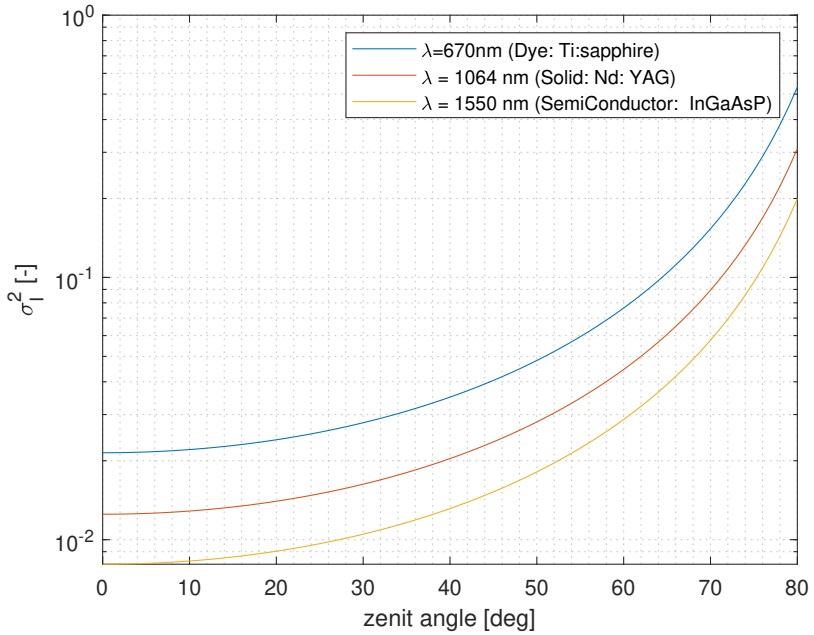

Figure 3.17: Scintillation index (σ_I^2) as function of zenital angle (φ). Considering Andrews *et al.* model, at $H = 2000$ km and $h_0 = 0$ m.

In figure 3.15 the far field intensity, after laser beam has travelled through the atmosphere, the receiver detect the beam as an speckle pattern. (A rough estimation for the speckle size

is $\rho_{\mathrm{I}} \approx 0.4\sqrt{R\lambda}$). If a receiving aperture is larger than a spatial scale size that produces the irradiance fluctuations, the receiver will average the fluctuations over the aperture and the scintillation will be less compared to scintillation measured with a point receiver; then, if the size of the receiver increases the receiver experiences a reduction of the fluctuation of total received power. The expression, from [60], describing the aperture averaging for plane waves in slant path is the following:

$$\Lambda = \left[1 + 1.11\left(\frac{D_{\mathrm{Rx}}^2}{h_s \lambda \cos\theta}\right)^{7/6}\right]^{-1} \tag{48}$$

Where λ is the wavelength in [μ m] , D_{rx} the diameter of collecting lens (Earth station aperture) in [m] and h_{s} is the turbulence scale height [m].

$$h_s = \left[\frac{\int_{h_0}^{H} C_n^2(h)(h-h_0)^2 dh}{\int_{h_0}^{H} C_n^2(h)(h-h_0)^{5/6} dh}\right]^{6/7} \tag{49}$$

Note that a longer wavelength causes larger speckle patterns and thus a reduced aperture-averaging effect, which leads to stronger power scintillation (σ_P^2) when plotted versus the scintillation index σ_{I}^2. At the same time Λ is the ratio between the normalised variance of the received power σ_{P}^2 and that of the intensity field σ_{I}^2;

$$\Lambda = \frac{\sigma_{\mathrm{P}}^2}{\sigma_{\mathrm{I}}^2}, \qquad 0 < \Lambda < 1 \tag{50}$$

Downlink communications:
Space probes main objective is to collect data, and thus a higher amount of bits is usually transmitted in downlink communications. Despite the fact that in downlink laser beam travels through free space for the major part of the journey, the impact of scintillation at the end of space-to-Earth path can be large enough to severely limit performance of receivers. If the receiver has a finite aperture larger than the atmospheric coherence length (a.k.a Fried parameter, r_0), the effect of scintillation is spatially averaged over the aperture resulting in a reduction of σ_{I}^2. While aperture averaging can mitigate amplitude scintillation effects, the corrupted phase can significantly degrade the performance of single spatial-mode optical receiver systems such as coherent detection or preamplified direct detection. The value of power scintillation σ_{P}^2 on paths in the space-to-Earth direction, equals the scintillation index but is modified by an aperture averaging factor, Λ. If required, further exact Gaussian beam formulations to compute σ_P^2 are presented in (p.177 [61]).

$$\sigma_{\mathrm{p\_downlink}}^2 = \Lambda \sigma_{\mathrm{I}}^2 \tag{51}$$

Uplink communications:
Uplink laser communications originated in the Earth are interesting from the point of view of future space manned missions, in which higher data rates will be required, for instance to provide live HD video. On the other hand, setting the OGS at the Earth surface can ease the maintenance and reduce costs.
According to ITU-R P.1622 recommendation [53] the variance of log-irradiance, on paths in the Earth-to-space (ES) direction, remain small ($\sigma^2_{\ln \mathrm{I}} \ll 4$), being $\sigma^2_{\mathrm{I}} = \exp(\sigma^2_{\ln \mathrm{I}}) - 1$. Experiments have verified that there is a low probability of exceeding this limit. Aperture averaging is generally not considered on paths in the Earth-to-space direction. A wavefront exiting the atmosphere experiences the same spatial redistribution of energy across its surface as occurs in the space-to-Earth direction. However, diffraction of the wavefront, as it propagates through space, spreads individual amplitude and phase perturbations across large areas (see figure 3.18).
Contrary to downlink, in literature it might be complex to obtain straightforward models to compute the turbulent loss during an uplink. For this reason, in this thesis it is not presented an uplink model to compute turbulent loss data during an uplink, but it will be acquired from different scientific papers. However, some models estimate the scintillation index σ^2_{I} for uplink spherical electromagnetic planes [58].

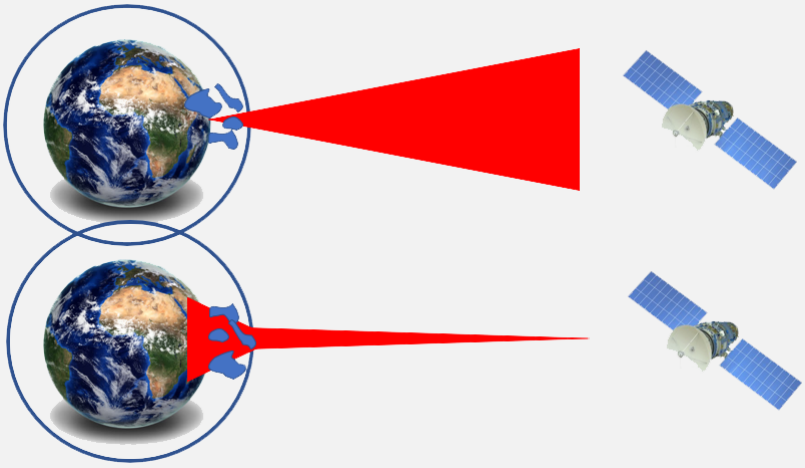

Figure 3.18: Uplink/Downlink beam refraction due to atmospheric turbulence.

Therefore, the turbulent loss (L_{turb}) which is in fact the laser beam amplitude fading, can be described by statistical models showing the probability density function (PDF) of the received signal x as following:

$$f(x) = \frac{1}{x\sqrt{2\pi\sigma^2_{\mathrm{LD}}}} \cdot \exp\left[-\frac{(\ln x - \mu_{\mathrm{LD}})^2}{2\sigma^2_{\mathrm{LD}}}\right] \tag{52}$$

Analysis presented in [54, 62] shows that the log-normal (LN) statistical model (see equation

52) generally adequately describes the amplitude-fading of the received signal. Therefore, the basic parameters of its lognormal distribution, σ_{LD} and μ_{LD} (the variance and mean of the originating normal distribution), must follow the relation:

$$\mu_{\mathrm{LD}} = -\frac{\ln(\sigma_P^2 + 1)}{2} = -\frac{\sigma_{\mathrm{LD}}^2}{2} \tag{53}$$

Then, the LN Rx power distribution $f(P_{\mathrm{Rx}})$ for a long-range static link with the long-term average received power $< P_{\mathrm{Rx}} >$ becomes:

$$f(P_{\mathrm{Rx}}) = \frac{1}{P_{\mathrm{Rx}}\sqrt{2\pi\sigma_{\mathrm{LD}}^2}} \cdot \exp\left[-\frac{\left[ln\left(\frac{P_{\mathrm{Rx}}}{<P_{\mathrm{Rx}}>}\right) - \mu_{\mathrm{LD}}\right]^2}{2\sigma_{\mathrm{LD}}^2}\right] \tag{54}$$

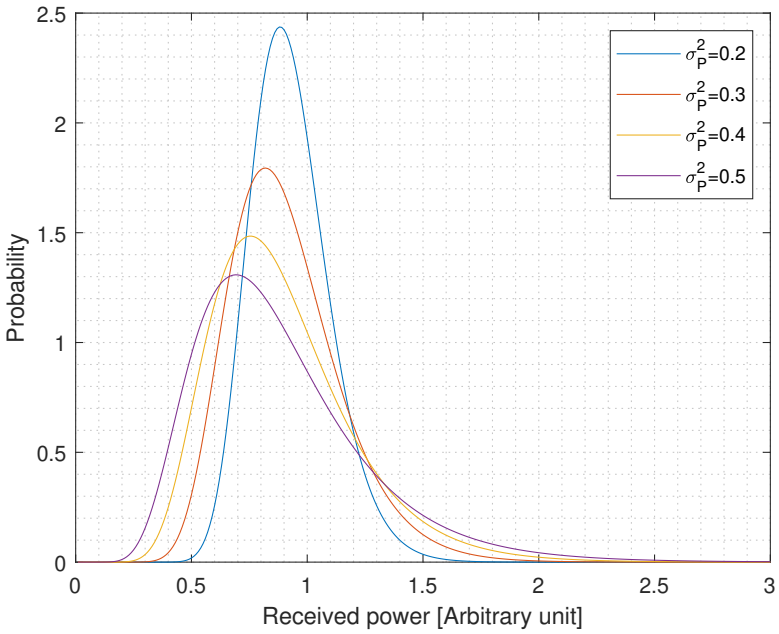

Figure 3.19: Received power PDF for a weak turbulence for different values of power scintillation index. The average received power here is $< P_{\mathrm{Rx}} >= 1$ in arbitrary unit.

When P_{Rx} is fading as described by Equation 54, a certain acceptable fraction of outage time is defined, during which $P_{\mathrm{Rx}} < P_{\mathrm{min}}$. Then, the required power margin between the average reception power $< P_{\mathrm{Rx}} >$ and P_{min} must be regarded as an additional loss in the link-budget calculation. This quantity is defined as the scintillation loss or turbulent loss (L_{turb}) of the transmission system in decibels (dB):

$$L_{\mathrm{turb}}(\mathrm{dB}) = 10\log\left(\frac{P_{\mathrm{min}}}{< P_{\mathrm{Rx}} >}\right) \tag{55}$$

With this threshold approach it is assumed that during times with P_{Rx} below P_{min} no data reception is possible at all. This reflects a good–bad-state channel modeling and does not require a detailed investigation of the specific receiver performance; the latter would again depend on modulation format and individual implementation performance. The fraction of outage time equals the probability p_{thr} that the actual power P_{Rx} falls below P_{min}. This threshold probability p_{thr} can be calculated with the distribution function based on Equation54 as indicated in [54, 62]:

$$p_{\mathrm{thr}}(P_{\mathrm{Rx}} < P_{\mathrm{min}}) = \int_0^{P_{\mathrm{min}}} f(P_{\mathrm{Rx}}) dP_{\mathrm{Rx}} = \frac{1}{2}\left(1 + erf\left\{\frac{ln\left[\frac{P_{\mathrm{min}}}{<P_{\mathrm{Rx}}>}\sqrt{\sigma_P^2+1}\right]}{\sqrt{2ln(\sigma_P^2+1)}}\right\}\right) \tag{56}$$

Where $\mathrm{erf}()$ denotes the error function. The principle is illustrated in Figure 3.20 with mean power, the loss fraction p_{thr} integral of the PDF-tail, and the according loss.

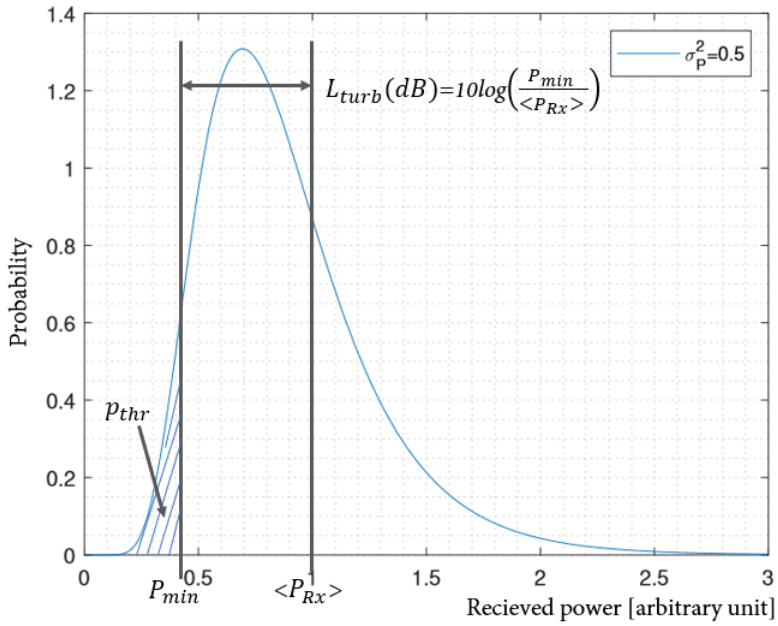

Figure 3.20: Achieving scintillation loss in a lognormal fading channel, relative to mean power $< P_{\mathrm{Rx}} >= 1$, $P_{\mathrm{min}} = 0.41a.u.$ Threshold probability p_{thr} value equals to the striped area below the curve. All parameters are illustrated under the power vector's probability distribution (blue line) for power scintillation value $\sigma_P^2 = 0.5$.

To calculate the fading loss (L_{turb}) the $\frac{P_{\mathrm{min}}}{<P_{\mathrm{rx}}>}$ term must be isolated from Equation56. By rearranging the equation it becomes:

$$\frac{P_{\mathrm{min}}}{< P_{\mathrm{Rx}} >} = \frac{\exp\left\{\mathrm{erf}^{-1}(2p_{\mathrm{thr}} - 1)\sqrt{2\ln(\sigma_{\mathrm{P}}^2+1)}\right\}}{\sqrt{\sigma_{\mathrm{P}}^2+1}} \tag{57}$$

By substituting Equation 57 into 55,

$$L_{\text{turb}}(\text{dB}) = 4.343 \left\{ \text{erf}^{-1}\left(2p_{\text{thr}} - 1\right) \left[\sqrt{2\ln(\sigma_p^2 + 1)}\right] - \frac{1}{2}\ln(\sigma_p^2 + 1) \right\} \tag{58}$$

From Ref. [54, 62, 63] it can be assumed a threshold probability (p_{thr}) interval between $0.5 - 1 \times 10^{-12}$. Turbulence losses under multiple conditions are shown in Figure 3.21.

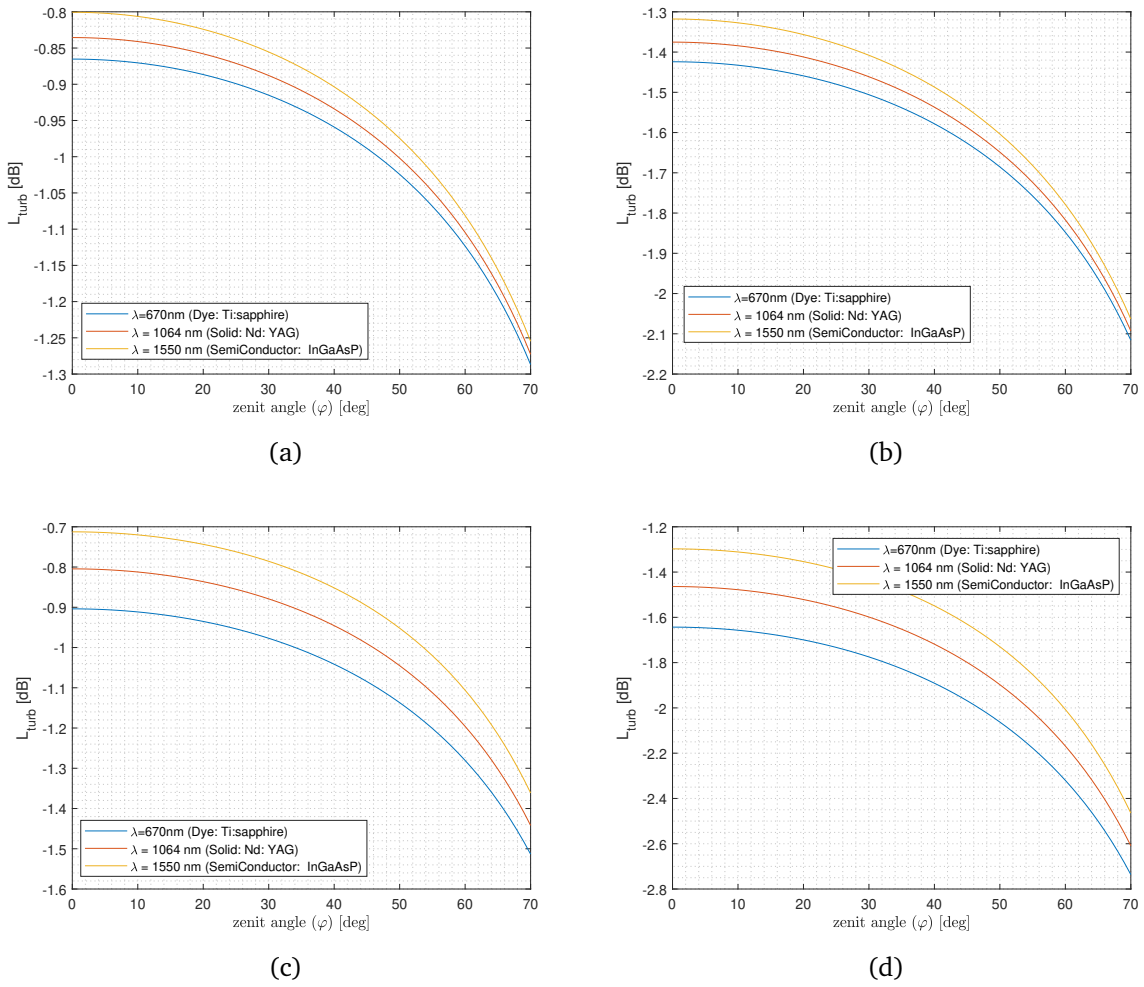

Figure 3.21: (a) Turbulent losses as function of zenit angle for a downlink communication from LEO orbit at multiple wavelengths, using Andrews *et al.* scintillation model with $H = 2000$ km and $h_0 = 0$. (a) $p_{\text{thr}} = 1 \times 10^{-5}$ and $D_{\text{Rx}} = 2$ m. (b) $p_{\text{thr}} = 1 \times 10^{-12}$ and $D_{\text{Rx}} = 2$ m. (c) $p_{\text{thr}} = 0.01$ and $D_{\text{Rx}} = 1$ m. (d) $p_{\text{thr}} = 1 \times 10^{-5}$ and $D_{\text{Rx}} = 1$ m.

4 Case Studies

This section presents two practical case studies for deep space optical communications. The objective pursued is to provide an application frame for the link power budget equation.In *Case Study I* an hypothetical Mars-Earth optical link is depicted, such link study has been considered appropriate owing to the recent interest in space sector to send manned missions to the red planet in a foreseeable future. Contrariwise, in a much closer and realistic mood, *Case Study II* is based on *Psyche* and DSOC mission which is estimated TBL in 2022.

4.1 Case study I: Hypothetical Mars-Earth optical downlink

To date, none FSO communication has overcome the maximum distance optical link record hold by the LLCD mission. However, the *Mars Telecommunications Orbiter* (MTO), encompassed under the MLCD mission, was to be, prior to its cancellation in 2005, the first satellite to beat that record by using a laser to beam its data from the red planet to Earth. Despite its cancellation, data from MLCD [64, 65] can be useful as a reference for this study, but reminding that almost after two decades, optical technology has reached new levels of maturity. MLCD Lasercom Terminal (MLT) communications system was designed for using pulsed format. In particular, Pulse Position Modulation (PPM) at a high alphabet size (M), was expected to support as high as 256-ary PPM, and thus, a low duty cycle. To achieve short (1-5 nsec) pulses, high average power (5 W) and high peak power (>300 W) were envisioned. MLT was planned to use a doped-fibre amplifier in a Master Oscillator Power Amplifier (MOPA) configuration. A COTS low-power distributed feedback (DFB) fibre laser based on Ytterbium-doped fibre was envisioned as the master laser and a $LiNbO_3$ Mach–Zehnder modulator would have provided the pulse modulation. To keep the mass low, a small telescope with a maximum diameter of 30.5cm telescope was purposed; nowadays FLT envision even lower diameters, but for the present case study we will maintain the same diameter value as MLT. The MLT's diffraction-limited beamwidth was about 3.5 μrad and the downlink wavelength was selected to be 1064 nm. Finally, the 5-meter Hale Telescope was selected as the receiver (equipped with an Avalanche Photo Diode, APD).

There is little doubt that sooner or later the MLCD concept arrive to Mars. If during the first part of 20s decade missions from table 2.2 are successful, the next step will involve Mars future orbiters being equipped, at the end of this decade, with such technology. For this reason, Fig.4.1 illustrates the Earth-Mars distance from a period going from 2021 to 2030.

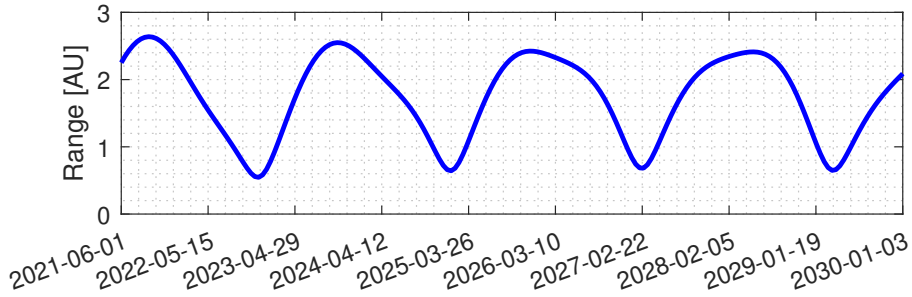

Figure 4.1: Earth-Mars distance from 2021 to 2030. Obtained using MICE.

From Fig.4.1 it is obtained the maximum Earth-Mars distance, 2.7 AU and hence the worst–case optical link scenario. Once this distance is known, it is obtained the link power budget equations parameters for the worst scenario, in terms of distance. The downlink analysis is shown in Table 4.1.

Mars Downlink ($\lambda = 1064$ nm)			
Parameters		Absolute Value	Equivalent Value [dB or dBm]
Transmitter parameters			
Laser Power, P_{TX}		5000 mW	36.98 dBm
Transmitter Gain, G_{Tx} TMF, $D_{\mathrm{Tx}} = 30.5$ cm		8.1×10^{11}	119.09 dB
η_A	Transmitter Gain efficiency g_{T} Obscuration ratio $\gamma_{\mathrm{Tx}} = 0$ $\alpha = \alpha_{\mathrm{opt}}$	0.814	-0.893 dB
	Strehl Loss L_{SR} RMS, $\sigma = \lambda/10$	0.673	-1.72 dB
Tx. efficiency η_{Tx}		0.65	-1.87 dB
Tx. pointing efficiency η_{TP}		0.9214	-0.35 dB
Channel Losses			
Space loss S Range, $R = 2.7$ au (worst case)		4.39×10^{-38}	-373.57 dB
L_{atm}	Transmittance Loss, L_{trans} Zenit angle, $\varphi = 0°$	0.95	-0.22 dB
	Turbulent Loss, L_{turb} $p_{\mathrm{thr}} = 1 \times 10^{-5}$ (Estimation based on Ref. [10])	0.845	-0.73 dB
Receiver parameters			
Receiver Gain, G_{Rx} Palomar-Hale, $D_{\mathrm{Rx}} = 5$ m Obscuration ratio $\gamma_{\mathrm{rx}} = 0.2$		2.17×10^{14}	143.38 dB
Receiver Gain efficiency g_{R}		0.96	-0.17 dB
Polarisation Loss L_{pol}		0.933	-0.3 dB
Rx. pointing efficiency η_{RP}		0.92	-0.36 dB
NBF transmission efficiency η_λ		0.6	-2.21 dB
Rx. efficiency η_{Rx}		0.65	-1.87 dB
Received Signal, P_{Rx}		3.28×10^{-12} W	-84.83 dBm
Margin		-	6 dB
Minimum detectable signal (Sensitivity), P_{s}		8.26×10^{-13} W	-90.8 dBm

Table 4.1: Link power budget equation parameters from an Hypothetical Mars DSOC Downlink.

Moreover, when the range between both planets is maximum another phenomenon occurs: the line of sight between both planets gets blocked by the Sun. The most stressing case happens for SEP angles lower than 3° (see Figure 4.2 and Figure 4.3).

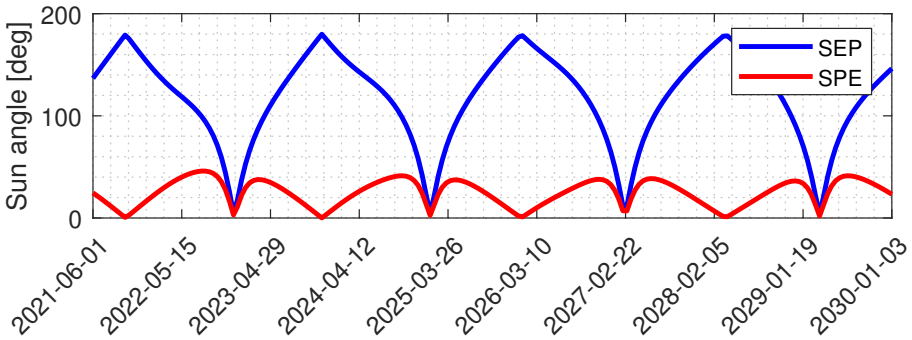

Figure 4.2: SEP, and SPE of Mars. Obtained using MICE.

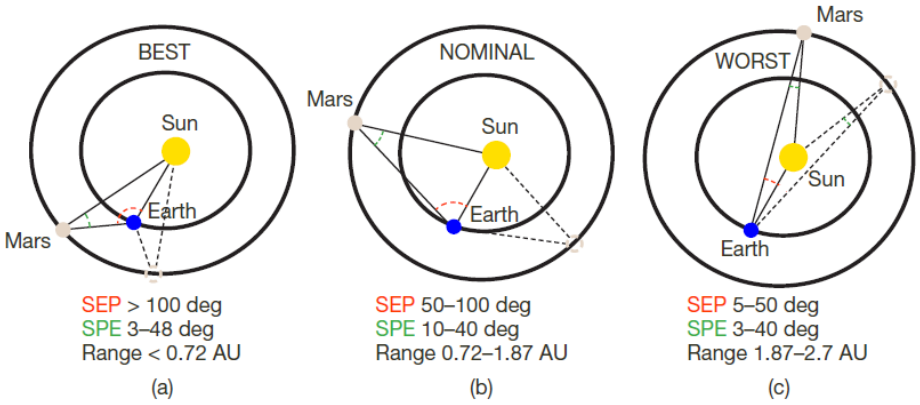

Figure 4.3: An ecliptic view of the Earth–Sun–Mars geometry for (a) “best”; (b) “nominal”; and (c) “worst” link conditions for an optical communication demonstration. [10]

When background photon flux (noise) is too much intense the signal can be masked and consequently become invisible for the detector. The remaining time noise contributes to degrade the communication and filtering techniques must be applied prior to the detection.

4.1.1 Received signal and noise

The received signal photon flux λ_s (in [photons/s]) [10], is defined as following:

$$\lambda_s = P_{\mathrm{Rx}} \frac{\lambda}{hc} \tag{59}$$

Whereas the received background photon flux λ_b or background noise in (photons/s) [12,43, 47] may come from multiple sources; These are diffused extended background noise coming

from the atmosphere, background noise from the Sun and other stellar (point) objects, and scattered light collected by the receiver, this last source is not considered in the study, as well as some pointing noise coming from stars that might be fitting in the field of view (FOV) of the receiver. Notice that some stars can increase the noise level portentously [66].

Furthermore, photodetectors produce dark noise [67], which are spurious photo-electrons that are present even with no incident light. For a well designed system, the contribution of dark current to the overall link budget is generally small, in this thesis, it would not be attacked the procedure for computing such noise. It must be taken into account that reducing the detectors area as well as cooling the detector results in lower dark count rates.

Finally, the total received background noise can be expressed as:

$$\lambda_b = \lambda_{\text{extended}} + \lambda_{\text{b\_point}} + \lambda_{\text{scattered}} + \text{dark\_noise} \tag{60}$$

Concerning the expressions that define either extended and point source noise, the FOV receiver solid angle term (Ω_{FOV}) must be considered when the solid angle of the noisy source, Ω_S, becomes greater than Ω_{FOV}. Observe Fig.4.4, Eq.61 and Equation 66.

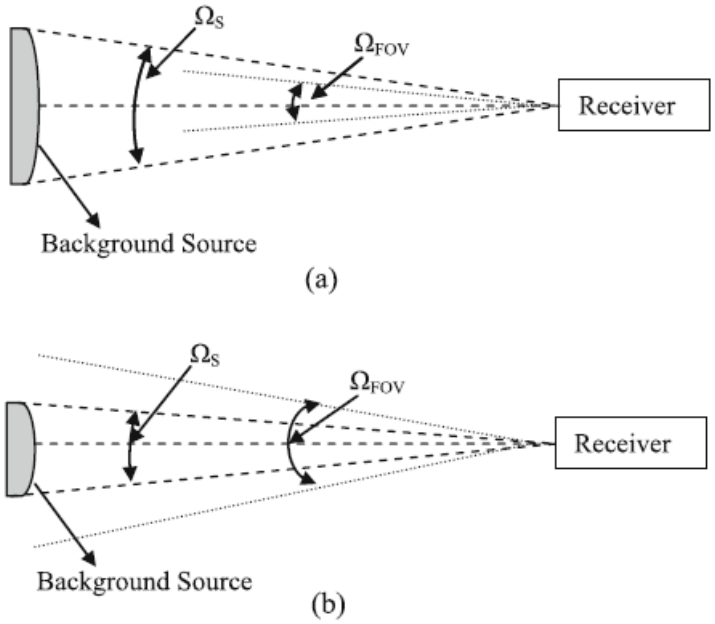

Figure 4.4: Geometry of (a) extended source when $\Omega_{\text{FOV}} < \Omega_{\text{S}}$ and (b) stellar or point source when $\Omega_{\text{S}} < \Omega_{\text{FOV}}$ [4].

In order to compute the different noise sources, in literature multiple formulations have been described, one of the most complete approach is found in Ref [47], nevertheless, more generic and compact expressions are also find in [5, 43]. The approach presented in this thesis has been based on the previously mentioned references and is detailed hereunder,

Extended noise ($\lambda_{\text{b\_extended}}$):

$$\lambda_{\text{b\_extended}} = P_{\text{b\_extended}} \cdot \frac{\lambda}{h\,c} = \eta^*_{\text{RX}} \cdot g_R \cdot A_{eff} \cdot \Omega_{\text{FOV}} \cdot \Delta\lambda_{\text{NBF}} \cdot L(\lambda) \cdot \eta_\lambda \cdot \eta_{\text{det}} \cdot \frac{\lambda}{h\,c} \tag{61}$$

Where;

- $P_{\text{b\_extended}}$ is the extended noise background power.
- η^*_{RX} [-] is the receiver system efficiency or optical throughput of the telescope and relay optics combination is (η^*_{RX}(dB)=η_{RX}-L_{pol}+3dB). Assuming that the laser signal light is circularly polarised meanwhile noise is not, so if proper polarising optics is installed at the ground receiver half (3dB) the background noise can be rejected.
- $\Delta\lambda_{\text{NBF}}$ represents the NBF optical bandwidth (in [Å]).
- $L(\lambda)$ represents the sky radiance at wavelength λ (in [W·sr^{-1}·m^{-2}·Å^{-1}]). It can be obtained using MODTRAN Web Application [28] which is available online and allows to configure multiple inputs.

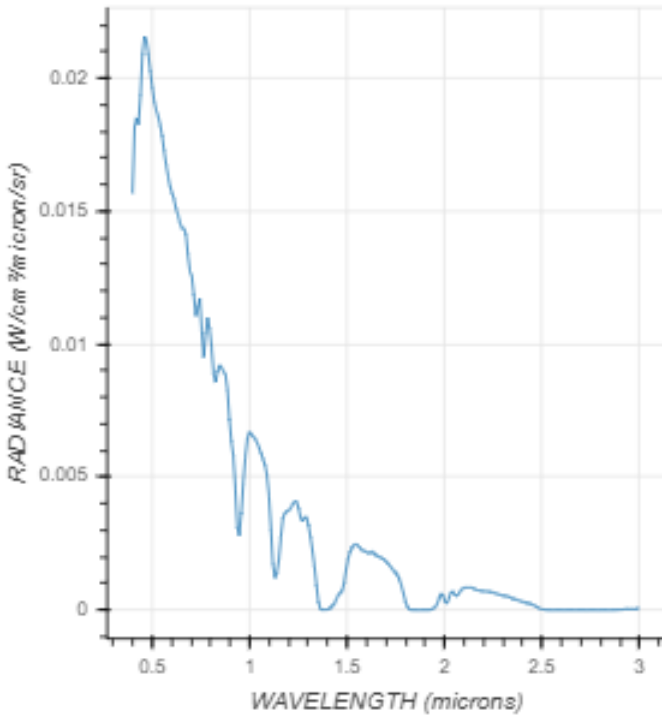

Figure 4.5: Atmospheric radiance in an Earth-to-space path at zenith ($R = 100$ km). A rural aerosol composition with a surface visual range of 23 km and US Atmosphere standard 1976 model is considered. The data refers to the case of an observer located at sea level (SL) and considering shortest (vertical) ground-to-space path (pointing at the zenith).

- h is the Planck's constant (in [J·s])

- c is the speed of light (in [m/s]).
- η_{det} [-] is the detectors' quantum efficiency, and concerns the fraction of incident photons which can be registered. COTS APDs, are available today, with quantum efficiency between 0.5-0.8 at 1064 nm [65].
- A_{eff} the effective area of the receiver (in [m^2]);

$$A_{\text{eff}} = \frac{G_{\text{RX}}\lambda^2}{4\pi} = \frac{\pi D_{\text{RX}}^2}{4} \tag{62}$$

- Ω_{FOV} is the receiver FOV solid angle (in [sr], and FOV angle in [rad]);

$$\Omega_{\text{FOV}} = 2\pi\left[1 - \cos\left(\frac{\theta_{\text{FOV}}}{2}\right)\right] \tag{63}$$

The solid angle can be determined by the approximation for small angles as,

$$\Omega_{\text{FOV}} \approx \frac{\pi\theta_{\text{FOV}}^2}{4} \tag{64}$$

Where θ_{FOV} is given by the receiver system is defined as,

$$\theta_{\text{FOV}} \approx 2\text{arctan}\left(\frac{d}{2f_{\text{d}}}\right) \tag{65}$$

Being f_{d} the focal length and d the size of the photo-detector.

Point noise (λ_{b_point}):

As previously mentioned, background point noise from other celestial bodies, with the exception of Mars, are not considered as a noisy source, thus $\lambda_{b\_point} = \lambda_{\text{b\_Mars}}$.

$$\lambda_{\text{b\_Mars}} = P_{\text{b\_Mars}} \cdot \frac{\lambda}{h\,c} = \eta_{\text{RX}}^* \cdot g_R \cdot A_{eff} \cdot \Delta\lambda_{\text{NBF}} \cdot I(\lambda)_{\text{Mars}} \cdot alb \cdot F \cdot L_{\text{atm}} \cdot \eta_\lambda \cdot \eta_{\text{det}} \cdot \frac{\lambda}{h\,c} \tag{66}$$

Where;

- $P_{\text{b\_Mars}}$ is the point Mars noise background power.
- alb [-] is the albedo of the planet Mars.
- $I(\lambda)$ is the irradiance from Mars incident at the Earth (in [W/m^2/Å]) [68, 69]

$$I(\lambda)_{\text{Mars}} = \frac{H_\lambda}{R_{\text{Mars-Sun}}^2}\left(\frac{R_{\text{Mars}}}{Z}\right)^2 \tag{67}$$

where H_λ is the solar flux at 1 au (in [W/m^2/Å]) (see Figure 4.6), $R_{\text{Mars}-\text{Sun}}$ is the sun-Mars distance (in [au]), R_{Mars} is the planet radius (in [km]), and Z is the distance between Mars and the receiver, the Earth (in [km]).

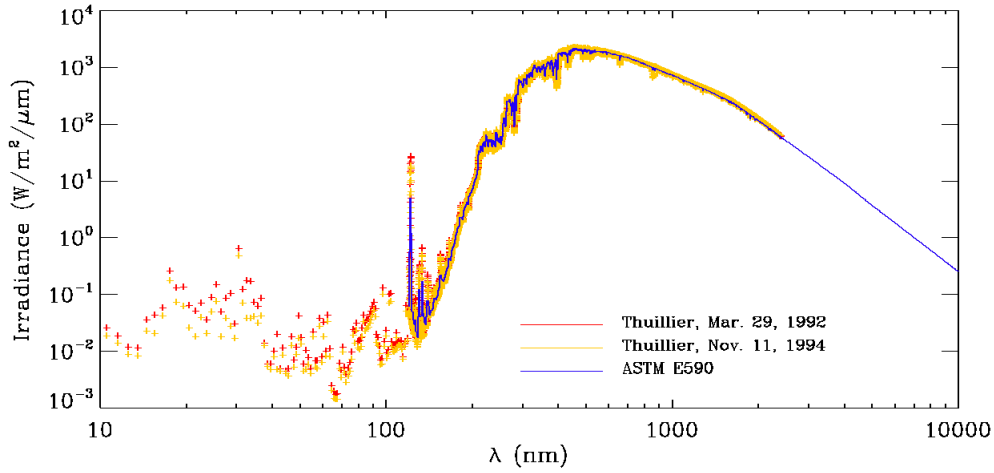

Figure 4.6: Thuillier 1992, 1994 and ASTM E590 Solar spectral irradiance models at a distance of 1 au. [11]

- F [-] is the correction factor considering the dependence of the albedo upon the Sun - probe - Earth (SPE) angle, F is modelled by the following polynomial,

$$F = 0.0003 \cdot \text{SPE}^2 - 0.0275 \cdot \text{SPE} + 1.1846 \tag{68}$$

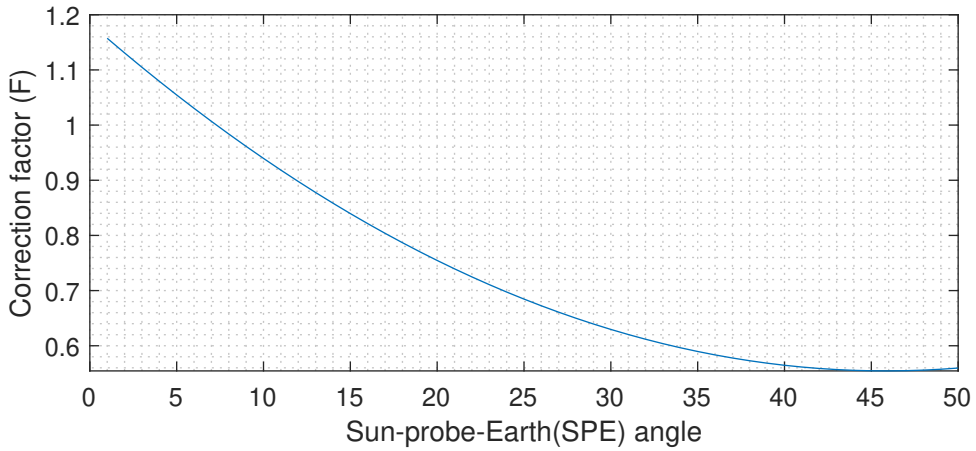

Figure 4.7: Correction factor, F [-] that takes into account multiple Sun illumination angles [deg].

Some of the parameters that are needed to compute the signal and noise fluxes were previously obtained and are shown in Table 4.1; on the contray, some others were not computed, and Table 4.2 shows the results that accounts for signal and noise above described procedure.

Mars Downlink Noise and Signal budget ($\lambda = 1064$ nm)		
Parameters	Absolute Value	Equivalent Value [dB or dBm]
Signal		
Received Power Signal, P_{RX}	3.28×10^{-12} W	-84.83 dBm
Received photon flux, λ_{s}	1.76×10^{7} photons/s	-
Noise equations data		
Tx. pointing efficiency, η_{RX}	0.65	-1.54 dB
Polarisation Loss, L_{pol}	1.072	-0.3 dB
-	-	+3 dB
Receiver efficiency, η^{*}_{RX}	1.21	0.8291 dB
Rx efficiency gain factor, g_{R}	0.96	-0.17 dB
Effective Area, A_{eff}	19.63 m^2	12.92 dBm^2
Receiver Field of view, θ_{FOV}	0.51μrad	-2.92 dBμrad
Receiver solid angle, Ω_{RX}	2.12×10^{-13} sr	-127.06 dBsr
NBF Bandwidth, $\Delta\lambda_{\mathrm{NBF}}$	2.5 $\mathring{A}$	3.97 dB$\mathring{A}$
Sky radiance, $L(\lambda)$ @ 1064nm	6.5×10^{-3} W $\cdot$ sr $^{-1}$ $\cdot$ m $^{-2}\cdot$ Å^{-1}	8.12 dBm sr^{-1} m^{-2} $\mathring{A}^{-1}$
Solar flux, H_λ, @ 1 ua @1064 nm	0.0669 W m^2 $\mathring{A}$	-11.74 dBW m^2 $\mathring{A}$
Distance $R_{\mathrm{Mars\_Sun}}$	1.52 au	-
Mars Radius, R_{Mars}	3389.5 km	-
Earth-Mars distance, Z	2.7 au	-
Irradiance from Mars incident to Earth, $I(\lambda)$	2.0294×10^{-12} W m^{-2} $\mathring{A}^{-1}$	3.07 dBW m^{-2} $\mathring{A}^{-1}$
Mars albedo, alb	0.25	-6.02 dB
Correction factor F, ($SPE = 3°$)	1.1048	-
NBF transmission efficiency η_λ	0.6	-2.21 dB
Quantum detector efficiency η_{det}	0.6	-2.21 dB
Atmospheric losses L_{atm}	0.80	-0.95 dB
Noise (Background power)		
Extended Noise		
Received extended noise $P_{\mathrm{b\_extended}}$	2.62×10^{-14} W	-105.81 dBm
Received extended photon flux $\lambda_{\mathrm{b\_extended}}$	1.40×10^{5} photons/s	-
Point Noise		
Received extended noise $P_{\mathrm{b\_Mars}}$	9.23×10^{-12} W	-80.34 dBm
Received extended photon flux $\lambda_{\mathrm{b\_Mars}}$	4.94×10^{7} photons/s	-
Scattered Noise		
Received scattered noise $P_{\mathrm{b\_scattered}}$	-	-
Received scattered photon flux $\lambda_{\mathrm{b\_scattered}}$	-	-
Dark Noise		
Received dark photon flux Dark current values are reported in Ref. [10]	-	-
Total		
Received background photon flux λ_{b}	4.96×10^{7} photons/s	-76.95 dBm

Table 4.2: Mars Downlink Noise and signal budget

The main lecture from the results displayed on the above table, and reported as well in literature (i.e Ref. [70]), is that in worst situations (long ranges, small SEP angles...) noise background flux may overcome the signal photon flux. However even when SNR<1 the signal can be processed but accounting for false-alarm and miss rate rises.

4.1.2 Capacity and signal modulation

When studying an optical link communication, another feature must be analysed, the capacity. Capacity can be understood as the tight upper bound on the data rate, DR, at which information can be reliably transmitted over a communication channel, it depends in part on the choice of modulation format and error-control coding scheme, this last item is not being treated in this thesis. The most general expression describing the capacity concerning deep space optical links is found in [71, 72]. However, this expressions may suffer some variations as function of the selected modulation. For FSO communications it is usually chosen the following modulation formats; on–off keying (OOK), pulse position modulation (PPM), and wavelength shift keying (WSK) [13]. Because PPM is an energy-efficient modulation format, it is commonly used in deep-space communications, while OOK is suitable for near-Earth optical links.

The M-ary PPM allows high peak-to-average-power ratio; in this modulation scheme, each channel symbol period is divided into M time slots, and the information is conveyed through the channel by the time window (a.k.a slot time, τ_{S}) in which the signal pulse is present. An illustration of the PPM modulation for a simple case of M = 8 (PPM order or alphabet size) is shown in Figure 4.8.

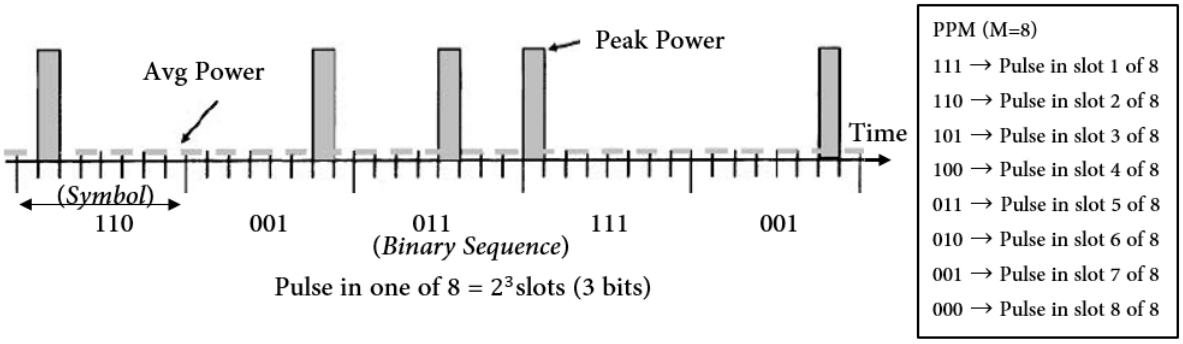

Figure 4.8: Example of a M-ary PPM modulation with M = 8 and straight binary mapping. Adapted from [12].

A Poisson channel model is used for detection of signal in background noise; however, for a PPM modulation the Poisson channel capacity does not, in general, have a closed form solution. Nevertheless, existing approximations provide insight into its behaviour. The PPM channel capacity with noise (in [bits/s]) can be computed using the expression from Equation 69 given at Ref. [67, 73];

$$C_{\mathrm{PPM}} \approx \frac{1}{\ln(2)E_{\lambda}} \left[\frac{P_{\mathrm{S}}^2}{P_{\mathrm{S}}\frac{1}{\ln(M)} + P_{\mathrm{b}}\frac{2}{M-1} + P_{\mathrm{S}}^2\frac{M\tau_{\mathrm{s}}}{\ln(M)E_{\lambda}}} \right] \tag{69}$$

where;

- P_{s} [W] is a measure of the weakest detectable optical signal. It is a parameter, intrinsically from the detector, which has to be selected taking into account that such parameter is constrained by the amount of received power, P_{RX}, at worst situation (for instance, the maximum range, R). P_{s} should not be equal to P_{RX}, so the optical link is designed with some margin by increasing the sensitivity of the detector, as in Ref. [44].
- Pb is the total noise power in [W].
- τ_{s} is the slot time in [s].
- $E_\lambda = h_p\, c/\lambda$ is the energy per photon (in [J]).
- M [-] is the PPM order or alphabet size.

Parameter	Absolute value
Received signal power, P_{S}	4.12×10^{-13} W
Received noise power, P_{b}	1.64×10^{-11} W
Energy per photon, E_λ	1.86×10^{-19} J
PPM order, M	8
Time slot, τ_{s}	1 ns
Capacity, bits/s	1.4 Mbps

Table 4.3: Capacity parameters, for an terminal orbiting Mars at $R = 2.7$ au from Earth.

As mentioned, data rate varies with the propagation distance, the most restrictive case is shown in table 4.3. On the other hand, data rate evolution is presented in Figure 4.9. Furthermore, studies such as [74–76] have also analysed interplanetary optical links and obtained similar results.

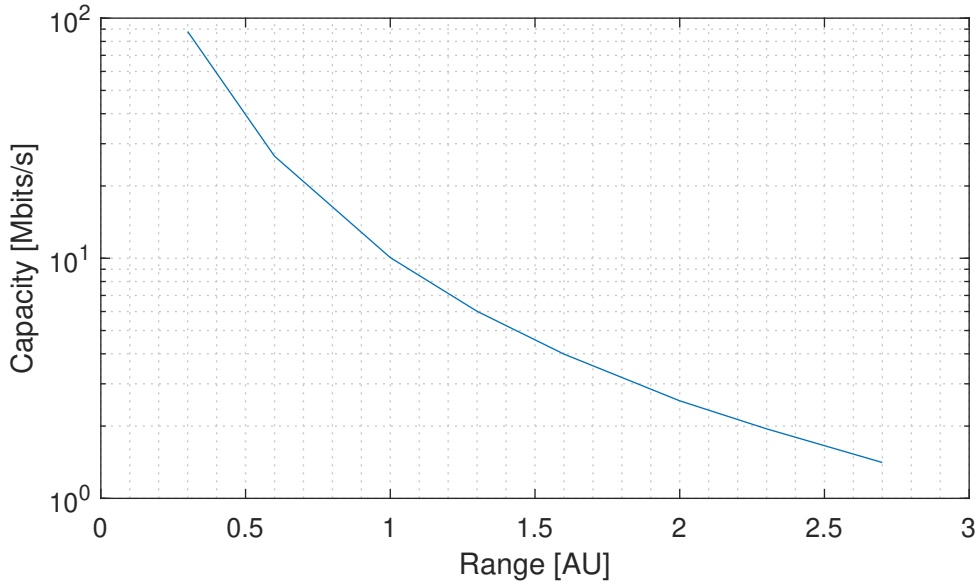

Figure 4.9: Data rate as a function of range (in [au]) for the sample Earth–Mars link.

4.1.3 Doppler and Point ahead

Additionally to the received signal and noise study, some other features that account in deep space laser communications must be considered. Among those, the point ahead angle and Doppler effect are of special interest. As the case study is only considering a downlink communication, it is necessary to obtain the relative velocities between Mars and the Earth. To do so, it has been used the SPICE from Matlab, known as MICE, from NASA's JPL NAIF (The Navigation and Ancillary Information Facility) (See Annex: Code).

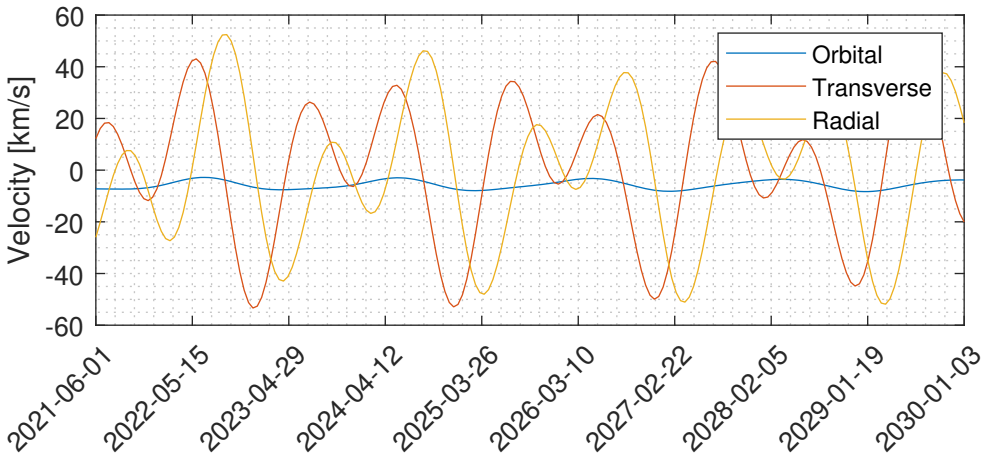

Figure 4.10: Earth-Mars relative velocities (Orbital, transverse and radial). Obtained using MICE

Once the transverse and radial Earth velocities, v_{trans}, v_{radial}, with respect to Mars are obtained (see Figure 4.10), the point ahead angle, Θ, and the frequency or wavelength Doppler shift $\Delta f\text{d}$, $\Delta\lambda\text{d}$ can be derived as indicated in Equations 70, 71, 72. Due to the finite speed of the light, beam pointing system is anticipated taking into account that the receiver terminal has moved and it is no longer at the angle it was observed; this anticipation is called the point ahead angle,

$$\Theta = \frac{2v_{\text{trans}}}{c} \tag{70}$$

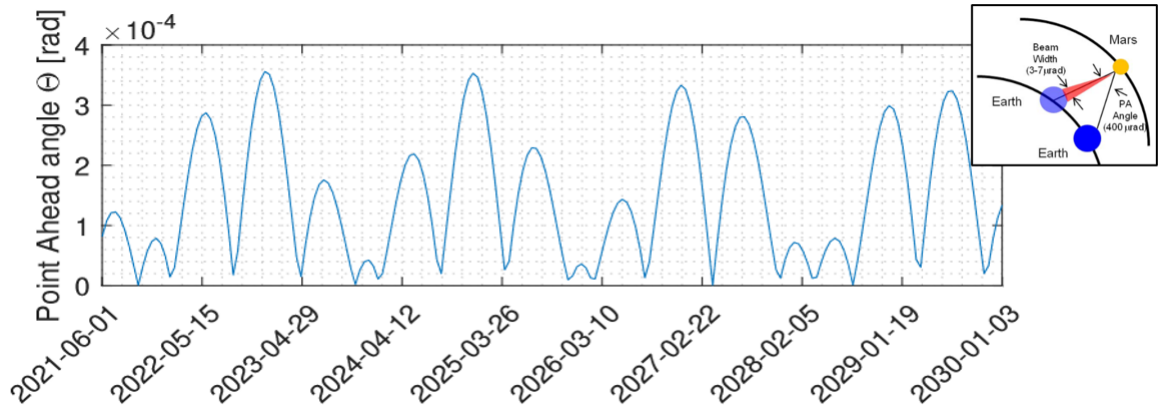

Figure 4.11: Point ahead angle from a transmitter orbiting Mars and transmitting through Earth direction. Obtained using MICE. Corner point ahead Mars-Earth schema from Ref. [13]

When a body that is emitting radiation has a non-zero radial velocity relative to an observer, the wavelength of the emission will be shortened or lengthened, depending upon whether the body is moving towards or away from an observer. This change in observed wavelength, or frequency, is known as the Doppler shift. For $v_{\text{radial}} \ll c$, the classical expression for the Doppler effect reads,

$$\Delta f_{\text{d}} \approx f \frac{v_{\text{radial}}}{c} \tag{71}$$

$$\Delta \lambda_{\text{d}} \approx \lambda \frac{v_{\text{radial}}}{c} \tag{72}$$

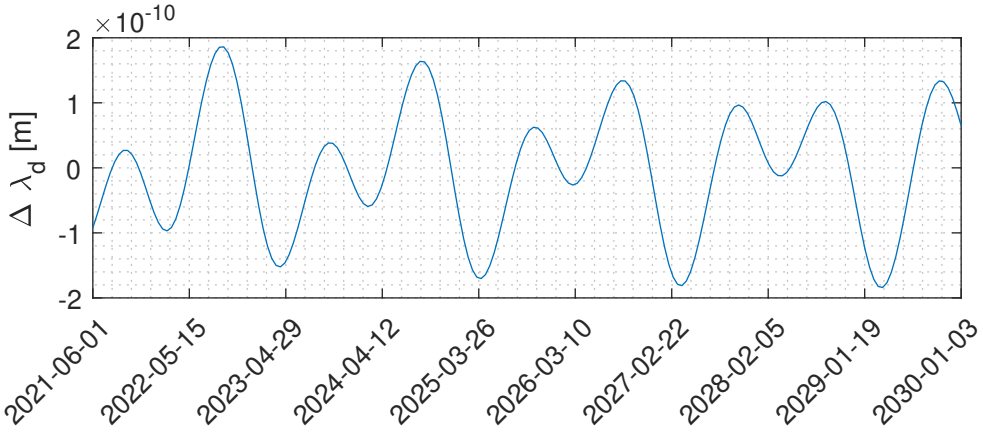

Figure 4.12: Doppler shift wavelength, considering Mars as an observer with respect to the Earth. Obtained using MICE.

To reject the maximum amount of noise, the NBF bandwidth should be as narrow as possible; however, by making it too narrow, it would result quite complex for the system to stay in tune with the laser beam line centre. For this reason, when deciding the bandwidth of the filter, is commonly used the following criteria; $\Delta\lambda_{\text{NBF}} > \max(|\Delta\lambda_{\text{d}}|)$. For the case study Mars example, the maximum $\Delta\lambda_{\text{d}}$ becomes 1.9 Å, which has lead to select a $\Delta\lambda_{\text{NBF}}$ of 2.5 Å(see table 4.2).

4.2 Case study II: *Psyche* & DSOC mission

The objective of *Case study II* is not to reissue the procedure concerning an interplanetary laser link, as done in *Case study I*, but to provide an overview of a real DSOC mission.

If everything goes according to plan, on August, 2022, NASA's *Psyche* mission will be launched, which plans to host the DSOC technology demonstration. After the MLCD [77] mission, which was cancelled in 2005, *Psyche* & DSOC is the second mission planning to establish a deep space optical link (beyond cis-lunar frontier) and consequently be the first one to accomplish such a feat.

In summary, *Psyche* & DSOC consists of a space exploration probe that will study the inner core of the asteroid 16 Psyche, which is orbiting the Sun at an average distance of 2.9 au.

To do so, it will perform a gravity assist around Mars in May 2023 in order to achieve the necessary velocity increase (ΔV) to reach the asteroid in 2026. During the trip and once it reaches its destination, the onboard optical communications module will emit a laser beam to 5 m-Hale telescope at Palomar Observatory (US), and receive it from 1 m-OCTL telescope at Table Mountain (US) (see Figure 4.13), thus achieving the longest distance optical link ever made and opening the door to a new paradigm for deep space communications.

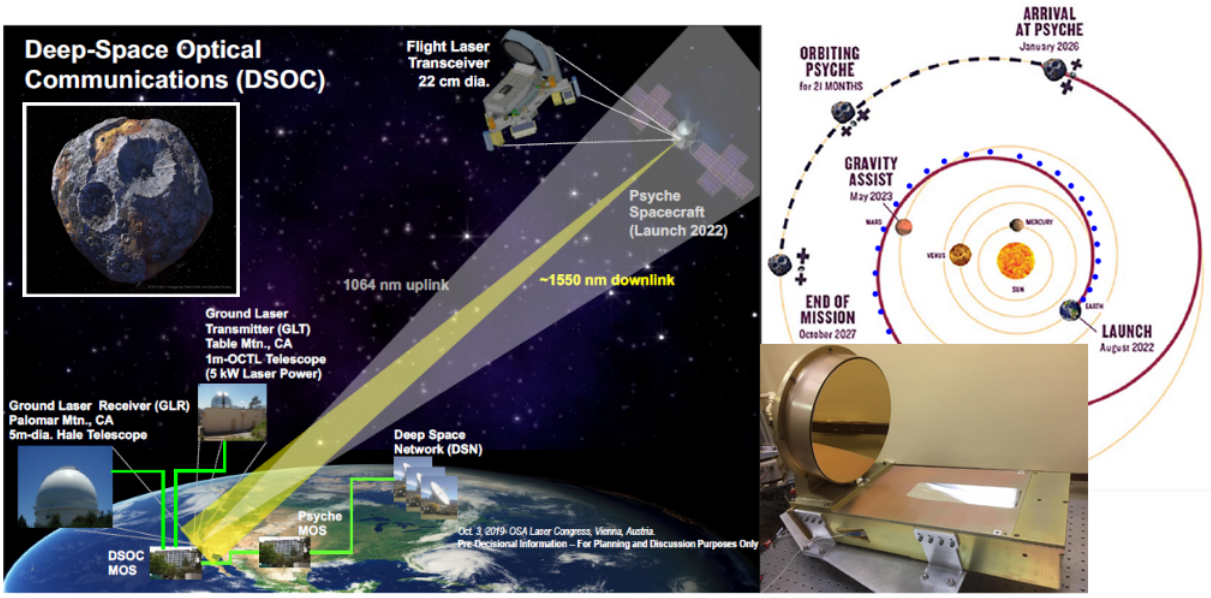

Figure 4.13: *Psyche* and DSOC layout, on the left the asteroid Psyche and OGS-FLT links. On the right, probe cruise to Psyche and optical transceiver assembly (OTA) FLT prototype. [7]

In the bottom right of Figure 4.13 is presented the frame of the optical system so-called OTA. Nevertheless, FLT is formed by multiple subsystems (see Fig4.14):

- Silicon carbide (SiC) Optical Telescope Assembly (OTA) receives beacon and transmits downlink
- Photon Counting Camera (PCC) detects “dim” 1064 nm laser beacon transmitted from Earth
- Isolation Pointing Assembly (IPA) “floats” OTA to stabilize and steer OTA line-of-sight
- Laser Transmitter Assembly (LTA) delivers high peak power pulse train modulated by downlink data
- Electronics – firmware/software platforms, power and clock distribution for “floating” and stationary parts, power and data interface to spacecraft

For further detail in [8] are depicted the involved mechanical pieces as well as the laser trajectory along the FLT.

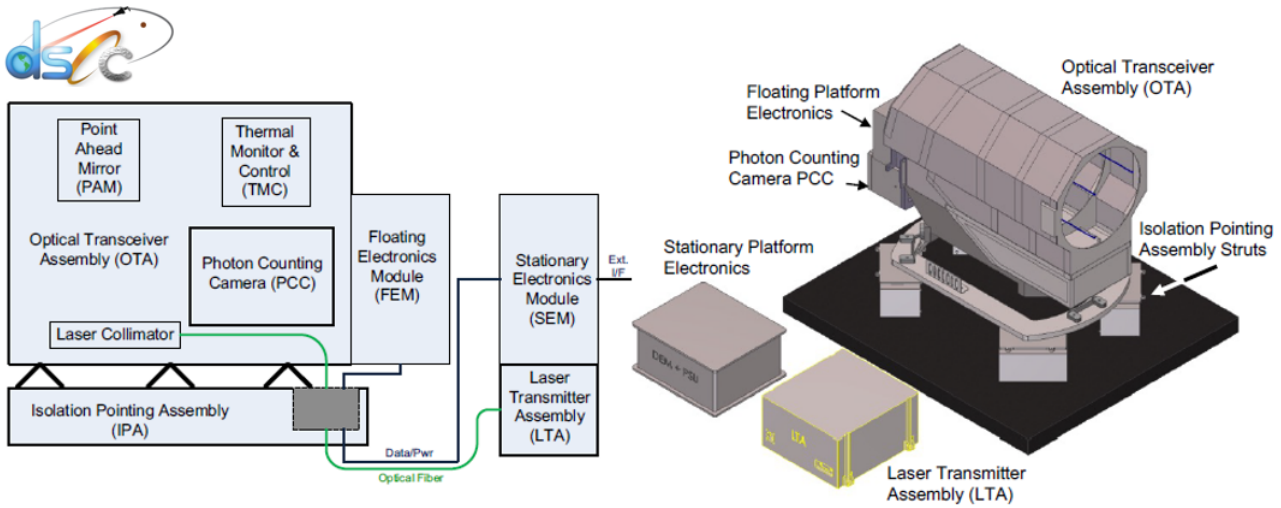

Figure 4.14: Flight laser transceiver [7].

Regarding *Psyche* & DSOC astrodynamics and flight laser parameters, in Figure 4.15 is presented a summary of the data to perform properly the link. Same graphics can be obtained by changing the observed body to *Psyche* in MICE code, available at *Appendix II: Code*.

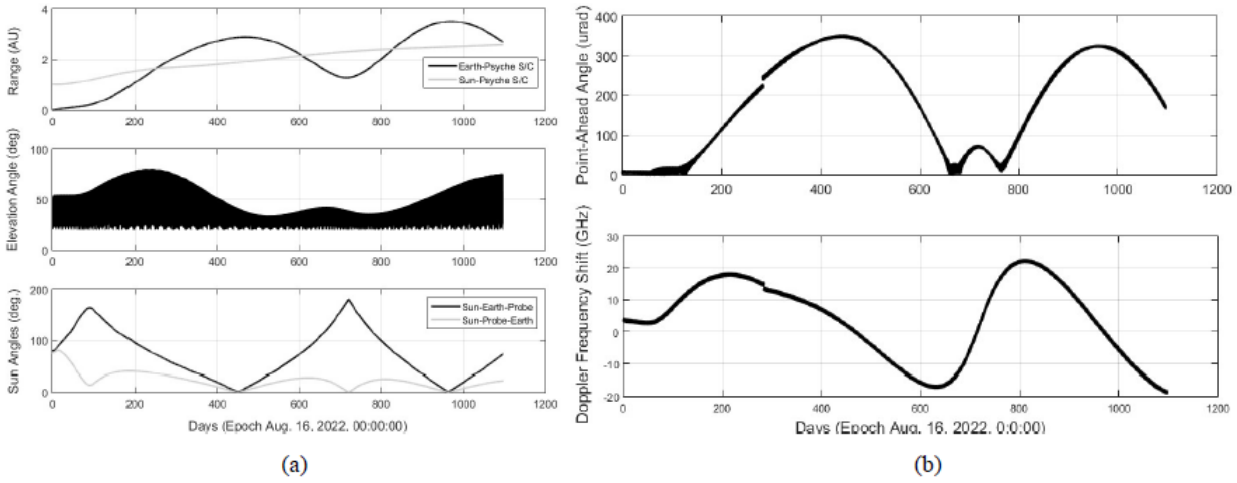

Figure 4.15: Psyche flight parameters summary [14]

Once Psyche's orbital parameters are known, the laser parameters can be designed according to ensure the mission success. A summary of the power link budget equation is displayed in *Appendix I: Psyche link power budget equation*, either for uplink and downlink scenarios. Finally, the achievable data rates were computed in [14], as illustrated in figure 4.16.

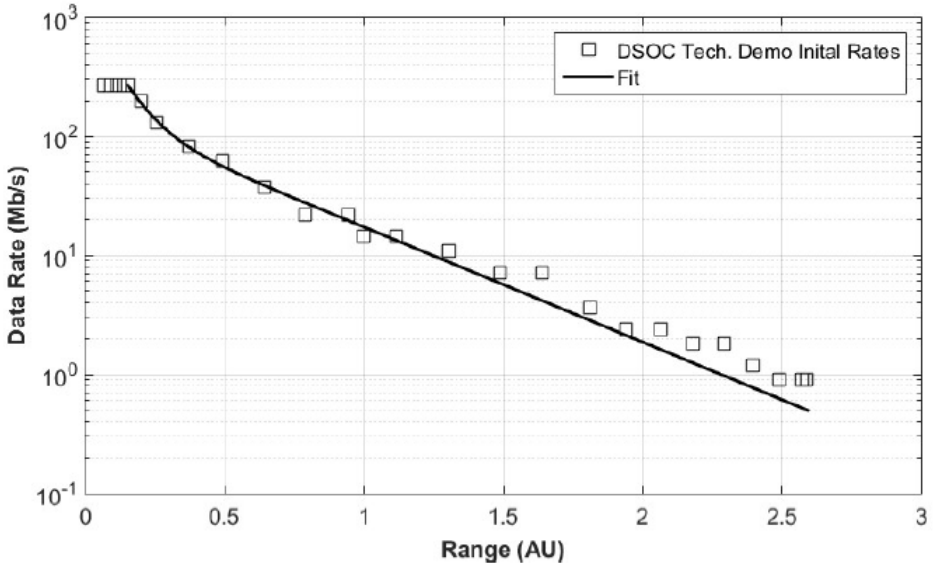

Figure 4.16: Data rate as a function of range (in [au]) for Earth–Psyche link. [14]

5 Conclusions and future work

5.1 Conclusions

The most salient outcome of this work are listed below:

1. We have analysed the best locations for optical ground stations around the world, and made a preliminary analysis of the costs incurred in the erection of an optical DSN.
2. We have performed a detailed analysis of the link equation, taking into account all the relevant inputs. This analysis has been made by means of a thorough analysis of the most salient works in optical communications.
3. Two application cases have been explored in detail, in particular the downlink of a hypothetical mission to Mars.

In the next few paragraphs, we expand a bit the discussion about this and other, less relevant, outcomes.

As has been discussed throughout this work, optical communications offer many advantages over RF band, but there is currently no international network for optical band communications for deep space roving probes. The climate study of the Earth, described in the first chapter, has brought to the table the privileged locations for installing such OGS, as well as, in a very general way, the cost that would be involved in the installation of such a network.

Conversely, since RF-based communications were implemented long before optical band communications, their characteristics are widely known. Therefore, in literature, the vast majority of authors are in agreement when explaining the different variables that form the link equation, a fact that occurs less frequently with the expressions used to model the behaviour of the signal in the optical band.

The development of this thesis has enabled us to carry out an in-depth research task among the diversity of scientific articles open to the community. The concept of laser communications to replace RF communications in deep space was proposed by JPL in the late 1970s [12]. However, the definitive implementation of this concept will take place throughout the present decade, as it has already been started in LEO environment with the *Starlink* project from the SpaceX company as well as with the LLCD mission and the future *Psyche* & DSOC. The results obtained from the upcoming missions will contribute to definitely settle or redefine some parameters from the mathematical as well as engineering point of view, as happened with the RF systems in the past.

The main learning obtained from the thesis concerning interplanetary optical links is that they are feasible, achieving a minimum requirement of $\sim$ 1 Mbps at the worst case studies scenarios, but much higher data rates in the overwhelming majority of scenarios. However, atmospheric turbulence or severe weather conditions may seriously degrade the link performance. For that reason as a future work it is proposed to study the effect of locating a transceiver as a relay on a sun synchronous orbit to overcome such troublesome.

5.2 Future developments

We have seen that, regarding optical links, beam mispointing is a critical parameter, and its effects have been computed and analysed resulting in $\sim$ 3 dB losses at $\sim$ 4 μrad deviation from central axis. As a future work it would be convenient to utilise the scripts presented on *Appendix II: Code* (which gather the minimum necessary information to extract the parameters involved in an optical link) and reorganise them in order to make a simulator with a graphic user interface similar to those of the Deep space Optical Link (*DeSOL*) shown in [78] or SCaN Optical Link Budget tool (*OLiBut*) shown in [54].

The atmospheric variables, like the extinction coefficient or the sky irradiance, have been introduced into the scripts as a known input for a particular wavelength. It would be interesting to link MODTRAN, LOWTRAN or HITRAN software with MATLAB, as well as studying and comparing multiple turbulent models. On the other hand, the astrodynamics study, performed with MICE, has not considered that the satellites containing the optical payload can be orbiting around planets, and so communication windows would be constrained by the availability between the transmitter and the receiver. Furthermore, natural satellites may produce occultations and consequently outage the laser link.

Another item that has been eluded, refers to the probe interplanetary cruise before arriving to its final destination or the fact that during its mission some probes perform fly-by manoeuvres, such as *Juno* mission did in June 7, 2021 by flying by Jupiter's giant moon Ganymede and showing the surface in remarkable detail including crater and long structural features possibly linked to tectonic faults.

Furthermore, it would be an interesting matter of study the effect of modifying the elevation angle, as well as comparing multiple modulation approaches in order to observe their contributions to the final link capacity. Notice that bit error rates and error control coding schemes have been out of the scope of this thesis as well as laboratory practises involving FSO coms; such issues ought to be developed in a further analysis.

Finally, as already stated, an analysis for space-located optical ground station seems of great relevance. Being located outside the terrestrial atmosphere, the optical beam would arrive to the receiver unaltered, greatly facilitating the task of obtaining a fast communication link. LEO, GEO and the surface of the Moon seem particularly well-suited locations, all with their own advantages and weaknesses.

6 Budget

In Table 6.1 is presented the estimated costs of the products and activities needed for the completion of this study. It is worth noting that this project started on February, 15, 2021, hence a completion duration of 4 months is applied.

Concept	Unit cost	Number of units	Cost [€]
Resources			
Human Resources	15€/h	400h	6000€
Personal Laptop depreciation	650€/6y	0.33y	35.75€
PC desktop depreciation	2000€/6y	0.05y	16.6€
MATLAB Academic License	250€/y	0.33y	82.5€
Internet Access	372€/y	0.33y	122.76€
Electric Consumption			
Personal Laptop (50W and 5h/day)	0.25€/kWh	30.11kWh	7.56€
Personal Laptop (200W and 3h/day)	0.25€/kWh	10.95kWh	2.73€
Total			6267.90€

Table 6.1: Cost of the project estimation.

First of all, human resources account for the expected retribution a junior engineer could be receiving these days. Second, most of the computations have been implemented and executed with the personal laptop, over the 4-months duration of this thesis.

In addition, the downloading and post-processing of all the atmospheric data (cloud coverage, aerosols...) was performed with a desktop computer which took approximately 18 days. It was done in such manner due to memory and capability reasons. The power consumption estimates for the personal laptop and the desktop computer are 50 and 200 W/h respectively.

Bibliography

[1] Light spectrum image source:. https://www.nasa.gov/directorates/heo/scan/engineering/technology/txt_opticalcomm.html, 2021 (accessed April 23, 2021).

[2] Farid Amoozegar, Robert Cesarone, Sabino Piazzolla, Leslie Paal, and Richard Emerson. Performance analysis and comparison of clustered and linearly dispersed optical deep space network. 2003.

[3] T Torrez. Rf/optical hybrid antenna. IPN Progress Report, pages 42–201, 2015.

[4] Hemani Kaushal, VK Jain, and Subrat Kar. Free space optical communication. Springer, 2017.

[5] Stephen G Lambert and William Lee Casey. Laser communications in space. Artech House, 1995.

[6] Warren J Smith. Modern optical engineering: the design of optical systems. McGraw-Hill Education, 2008.

[7] Abhijit Biswas. Nasa's deep space optical communications–an update. In Applications of Lasers for Sensing and Free Space Communications, pages LTh1B–1. Optical Society of America, 2019.

[8] W Thomas Roberts. Discovery deep space optical communications (dsoc) transceiver. In Free-Space Laser Communication and Atmospheric Propagation XXIX, volume 10096, page 100960V. International Society for Optics and Photonics, 2017.

[9] Dirk Giggenbach. Optical free space links for satellite-ground communications. 2014.

[10] Abhijit Biswas, Hamid Hemmati, Sabino Piazzolla, Bruce Moision, Kevin Birnbaum, and Kevin Quirk. Deep-space optical terminals (dot) systems engineering. IPN Progress Report, 42:183, 2010.

[11] Rob Garner. Solar irradiance. https://www.nasa.gov/mission_pages/sdo/science/solar-irradiance.html, Nov 27, 2017 (accessed June, 2021).

[12] Hamid Hemmati. Deep space optical communications, volume 11. John Wiley & Sons, 2006.

[13] Hamid Hemmati, Abhijit Biswas, and Ivan B Djordjevic. Deep-space optical communications: Future perspectives and applications. Proceedings of the IEEE, 99(11):2020–2039, 2011.

[14] Abhijit Biswas, Meera Srinivasan, Sabino Piazzolla, and Daniel Hoppe. Deep space optical communications. In Free-Space Laser Communication and Atmospheric Propagation XXX, volume 10524, page 105240U. International Society for Optics and Photonics, 2018.

[15] Antonios Seas, Bryan Robinson, Tina Shih, Farzana Khatri, and Mark Brumfield. Optical communications systems for nasa's human space flight missions. In International Conference on Space Optics—ICSO 2018, volume 11180, page 111800H. International Society for Optics and Photonics, 2019.

[16] Mars 2020 mission communications. https://mars.nasa.gov/mars2020/spacecraft/rover/communications/, 2021 (accessed April 23, 2021).

[17] Dlr researchers set world record in free-space optical communications, nov 2016. https://www.dlr.de/content/en/articles/news/2016/20161103_world-record-in-free-space-optical-communications_19914.html#:~:text=Researchers%20at%20the%20German%20Aerospace,of%2045%20DVDs%20per%20second., 2021 (accessed April 26, 2021).

[18] Nasa, deep space optical communications (dsoc). https://gameon.nasa.gov/archived-projects-2/deep-space-optical-communications-dsoc/, 2021 (accessed April 26, 2021).

[19] John A Maynard and M Ross. Airborne flight test system (afts). Technical report, MCDONNELL DOUGLAS ASTRONAUTICS CO-ST LOUIS MO, 1981.

[20] Keith E Wilson, James R Lesh, and Tsun-Yee Yan. Gopex: a laser uplink to the galileo spacecraft on its way to jupiter. In Free-Space Laser Communication Technologies V, volume 1866, pages 138–146. International Society for Optics and Photonics, 1993.

[21] KE Wilson. An overview of the gold experiment between the ets-vi satellite and the table mountain facility. The Telecommunications and Data Acquisition Progress Report 42-124, October–December 1995, pages 8–19, 1996.

[22] Badri A Younes and James S Schier. Space communications and navigation (scan) integrated network architecture definition document (add). volume 1; executive summary; revision 1. 2010.

[23] In Keun Son and Shiwen Mao. A survey of free space optical networks. Digital communications and networks, 3(2):67–77, 2017.

[24] Hamid Hemmati. Near-earth laser communications, volume 1. CRC press, 2020.

[25] Alexander Vavoulas, Harilaos G Sandalidis, and Dimitris Varoutas. Weather effects on fso network connectivity. IEEE/OSA Journal of Optical Communications and Networking, 4(10):734–740, 2012.

[26] Laads daac, level-1 and atmosphere archive distribution system distributed active archive center. https://ladsweb.modaps.eosdis.nasa.gov/, 2021 (accessed April 4, 2021).

[27] The spice toolkit, nasa caltech. https://naif.jpl.nasa.gov/naif/toolkit.html, 2021 (accessed April 2, 2021).

[28] Spectral science inc. modtran web app. `http://modtran.spectral.com/modtran_home`, 2021 (accessed May 14, 2021).

[29] Leslie J Deutsch, Stephen M Lichten, Anthony J Russo, Donald M Cornwell, and Daniel J Hoppe. Toward a nasa deep space optical communications system. In 2018 SpaceOps Conference, page 2554, 2018.

[30] Inigo del Portillo, Marc Sanchez, Bruce Cameron, and Edward Crawley. Optimal location of optical ground stations to serve leo spacecraft. In Proc. IEEE Aerosp. Conf., pages 1–16, 2017.

[31] Stephen A Townes, Bernard L Edwards, A Biswas, DR Bold, RS Bondurant, D Boroson, JW Burnside, DO Caplan, AE DeCew, R DePaula, et al. The mars laser communication demonstration. In 2004 IEEE Aerospace Conference Proceedings (IEEE Cat. No. 04TH8720), volume 2, pages 1180–1195. IEEE, 2004.

[32] Mars relay network. `https://www.jpl.nasa.gov/news/the-mars-relay-network-connects-us-to-nasas-martian-explorers`, 2021 (accessed May 2, 2021).

[33] Esa mars orbiters support nasa perseverance landing. `https://www.esa.int/Enabling_Support/Operations/ESA_Mars_orbiters_support_NASA_Perseverance_landing`, 2021 (accessed May 2, 2021).

[34] Jeffrey R Charles, Daniel J Hoppe, and Asim Sehic. Hybrid rf/optical communication terminal with spherical primary optics for optical reception. In 2011 International Conference on Space Optical Systems and Applications (ICSOS), pages 171–179. IEEE, 2011.

[35] JR Lesh and DL Robinson. A cost-performance model for ground-based optical communications receiving telescopes. TDA Progress Report 42, 87:56–64, 1986.

[36] Gerard Theodore van Belle, Aden Baker Meinel, and Marjorie Pettit Meinel. The scaling relationship between telescope cost and aperture size for very large telescopes. In Ground-based telescopes, volume 5489, pages 563–570. International Society for Optics and Photonics, 2004.

[37] Larry M Stepp, Larry G Daggert, and Paul E Gillett. Estimating the costs of extremely large telescopes. In Future giant telescopes, volume 4840, pages 309–321. International Society for Optics and Photonics, 2003.

[38] Yaqin Zhao, Danli Xu, and Xin Zhong. Scintillation reduction using multi-beam propagating technique in atmospheric wocdma system. Chinese Optics Letters, 9(11):110602, 2011.

[39] Michael D King, W Paul Menzel, Yoram J Kaufman, Didier Tanré, Bo-Cai Gao, Steven Platnick, Steven A Ackerman, Lorraine A Remer, Robert Pincus, and Paul A Hubanks. Cloud and aerosol properties, precipitable water, and profiles of temperature and water

vapor from modis. IEEE Transactions on Geoscience and Remote Sensing, 41(2):442–458, 2003.

[40] Platnick S. et al. Modis atmosphere l3 monthly product. nasa modis adaptive processing system, goddard space flight center, usa:. `http://dx.doi.org/10.5067/MODIS/MOD08_M3.061`, 2015 (accessed April, 2021).

[41] T Ayash, SL Gong, CQ Jia, P Huang, TL Zhao, and D Lavoue. Global modeling of multicomponent aerosol species: Aerosol optical parameters. Journal of Geophysical Research: Atmospheres, 113(D12), 2008.

[42] Descanso, deep space communications and navigation center of excellence. `https://descanso.jpl.nasa.gov/`, 2021 (accessed May 5, 2021).

[43] WK Marshall and BD Burk. Received optical power calculations for optical communications link performance analysis. TDA Progress Report 42, 87:32–40, 1986.

[44] Bruce Moision, Janet Wu, and Shervin Shambayati. An optical communications link design tool for long-term mission planning for deep-space missions. In 2012 IEEE Aerospace Conference, pages 1–12. IEEE, 2012.

[45] John J Degnan and Bernard J Klein. Optical antenna gain. 2: Receiving antennas. Applied optics, 13(10):2397–2401, 1974.

[46] Bernard J Klein and John J Degnan. Optical antenna gain. 1: Transmitting antennas. Applied optics, 13(9):2134–2141, 1974.

[47] Abhijit Biswas and Sabino Piazzolla. Deep-space optical communications downlink budget from mars: System parameters. IPN Progress Report, 42(154):0–1, 2003.

[48] VA Vilnrotter. The effects of pointing errors on the performance of optical communications systems. TDA Progress Report 42, 63:136–146, 1981.

[49] Stephen Hall. A survey of free space optical communications in satellites. 2020.

[50] William Blitzstein, Richard J Mitchell, and Bruce D Holenstein. Estimation of detector response in optical astronomical radiometry. Applied optics, 26(11):2055–2055, 1987.

[51] F Series. Fixed service applications using free-space optical links. 2011.

[52] Frederick G Smith, Joseph S Accetta, and David L Shumaker. The infrared & electro-optical systems handbook. atmospheric propagation of radiation, volume 2. Technical report, INFRARED INFORMATION AND ANALYSIS CENTER ANN ARBOR MI, 1993.

[53] Propagation Data. Prediction methods required for the design of earth-space systems operating between 20 thz and 375 thz. Recommendation ITU-R P.1622, 2003.

[54] Hennes Henniger and Otakar Wilfert. An introduction to free-space optical communications. Radioengineering, 19(2), 2010.

[55] Abdulsalam Alkholidi and Khalil Altowij. Effect of clear atmospheric turbulence on quality of free space optical communications in western asia, das, n.(ed.) optical communications systems, isbn: 978-953-51-0170-3, 2012.

[56] Larry C Andrews and Ronald L Phillips. Laser beam propagation through random media. SPIE, 2005.

[57] Larry C Andrews. University of central florida. Field Guide to Atmospheric Optics.

[58] Larry C Andrews, Ronald L Phillips, and Cynthia Y Young. Scintillation model for a satellite communication link at large zenith angles. Optical Engineering, 39(12):3272–3280, 2000.

[59] Richard J Sasiela. Electromagnetic wave propagation in turbulence: evaluation and application of Mellin transforms, volume 18. Springer Science & Business Media, 2012.

[60] Hal T Yura and WG McKinley. Aperture averaging of scintillation for space-to-ground optical communication applications. Applied Optics, 22(11):1608–1609, 1983.

[61] Larry C Andrews, Ronald L Phillips, and Cynthia Y Hopen. Laser beam scintillation with applications, volume 99. SPIE press, 2001.

[62] Dirk Giggenbach and Hennes Henniger. Fading-loss assessment in atmospheric free-space optical communication links with on-off keying. Optical Engineering, 47(4):046001, 2008.

[63] Dirk Giggenbach and Florian Moll. Scintillation loss in optical low earth orbit data downlinks with avalanche photodiode receivers. In 2017 IEEE International Conference on Space Optical Systems and Applications (ICSOS), pages 115–122. IEEE, 2017.

[64] Don M Boroson, Abhijit Biswas, and Bernard L Edwards. Mlcd: Overview of nasa's mars laser communications demonstration system. In Free-Space Laser Communication Technologies XVI, volume 5338, pages 16–28. International Society for Optics and Photonics, 2004.

[65] Don M Boroson, Roy S Bondurant, and Joseph J Scozzafava. Overview of high-rate deep-space laser communications options. In Free-Space Laser Communication Technologies XVI, volume 5338, pages 37–49. International Society for Optics and Photonics, 2004.

[66] RC Ramsey. Spectral irradiance from stars and planets, above the atmosphere, from 0.1 to 100.0 microns. Applied Optics, 1(4):465–471, 1962.

[67] Sam Dolinar, Bruce Moision, and Baris Erkmen. Fundamentals of free-space optical communications. 2012.

[68] Farzana I Khatri, Don M Boroson, Daniel V Murphy, and Jaya Sharma. Link analysis of mars-earth optical communications system. In Free-Space Laser Communication Technologies XVI, volume 5338, pages 143–150. International Society for Optics and Photonics, 2004.

[69] J Katz. Planets as background noise sources in free space optical communications. The Telecommunications and Data Acquisition Progress Report 42-85, January–March 1986, pages 13–24, 1986.

[70] Shinhak Lee, Keith E Wilson, and Mitchell Troy. Background noise mitigation in deep-space optical communications using adaptive optics. Interplanetary Network Progress Report, 161, 2005.

[71] Bruce Moision and Jon Hamkins. Deep-space optical communications downlink budget: modulation and coding. IPN Progress Report, 42(154):1–28, 2003.

[72] Konrad Banaszek, Ludwig Kunz, Marcin Jarzyna, and Michal Jachura. Approaching the ultimate capacity limit in deep-space optical communication. In Free-Space Laser Communications XXXI, volume 10910, page 109100A. International Society for Optics and Photonics, 2019.

[73] Bruce Moision and Hua Xie. An approximate link equation for the direct-detected optical ppm link. Interplanet. Netw. Prog. Rep, 199(27):1, 2014.

[74] Julian Breidenthal, Hua Xie, and Loren Clare. Optical ground segment performance summary. The Interplanetary Network Progress Report, 42:205, 2016.

[75] Julian Breidenthal and Douglas Abraham. Design reference missions for deep-space optical communication. The Interplanetary Network Progress Report, 42:205, 2016.

[76] Bruce Moision and William Farr. Range dependence of the optical communications channel. The Interplanetary Network Progress Report, 42:199, 2014.

[77] A Biswas, D Boroson, and B Edwards. Mars laser communication demonstration: what it would have been. In Free-Space Laser Communication Technologies XVIII, volume 6105, page 610502. International Society for Optics and Photonics, 2006.

[78] Hua Xie, David Heckman, and Julian Breidenthal. Link characterization for deep-space optical communications. The Interplanetary Network Progress Report, 42:205, 2016.

Appendix I: Psyche link power budget equation

Psyche Downlink ($\lambda = 1550.12 \pm 0.04nm$)			
Parameters		Absolute Value	Equivalent Value [dB or dBm]
Transmitter paramters			
Laser Power, P_{TX}		4000mW	36.02 dBm
Transmitter Gain, G_{Tx} FLT, $D_{Tx} = 22cm$		1.98×10^{11}	112.98 dB
η_A	Transmitter Gain efficiency g_T Obscuration ratio $\gamma_{Tx} = 0$ $\alpha = \alpha_{opt}$	0.814	-0.893dB
	Strehl Loss L_{SR} RMS, $\sigma = \lambda/10$	0.673	-1.72 dB
Tx. efficiency η_{Tx}		0.7	-1.54 dB
Tx. pointing efficiency η_{TP}		0.921	-0.36 dB
Channel Losses			
Space loss S Range, $R = 3au$ (worst case)		7.55×10^{-38}	-371.22 dB
L_{atm}	Transmittance Loss, L_{trans} Zenit angle, $\varphi = 0°$	0.95	-0.22 dB
	Turbulent Loss, L_{turb} $p_{thr} = 1 \times 10^{-5}$	0.845	-0.73 dB
Receiver parameters			
Receiver Gain, G_{Rx} Palomar-Hale, $D_{Rx} = 5m$ Obscuration ratio $\gamma_{rx} = 0.2$		1.027×10^{14}	140.11 dB
Receiver Gain efficiency g_R		0.96	-0.17dB
Polarization Loss L_{pol}		0.933	-0.3 dB
Rx. pointing efficiency η_{RP}		1	0 dB
NBF transmission efficiency η_λ		0.7	-1.54 dB
Rx. efficiency η_{Rx}		0.7	-1.54 dB
Received Signal, P_{Rx}		7.68×10^{-13}W	-91.1 dBm

Link power budget equation parameters from Psyche DSOC Downlink.

Psyche Uplink ($\lambda = 1064nm$)			
Parameters		Absolute Value	Equivalent Value [dB or dBm]
Transmitter paramters			
Laser Power, P_{TX}		5kW	66.98dBm
Transmitter Gain, G_{Tx} TMF, $D_{Tx} = 1m$		8.71×10^{12}	129.40 dB
η_A	Transmitter Gain efficiency g_T Obscuration ratio $\gamma_{Tx} = 0.2$ $\alpha = \alpha_{opt}$	0.708	-1.499dB
	Strehl Loss L_{SR} RMS, $\sigma = \lambda/10$	0.673	-1.72 dB
Tx. efficiency η_{Tx}		0.7	-1.54 dB
Tx. pointing efficiency η_{TP}		0.914	-0.39 dB
Channel Losses			
Space loss S Range, $R = 3au$ (worst case)		3.56×10^{-38}	-374 dB
L_{atm}	Transmittance Loss, L_{trans} Zenit angle, $\varphi = 0°$	0.95	-0.22 dB
	Turbulent Loss, L_{turb} $p_{thr} = 1 \times 10^{-5}$	0.845	-0.73 dB
Receiver parameters			
Receiver Gain, G_{Rx} FLT, $D_{Rx} = 22cm$ Obscuration ratio $\gamma_{rx} = 0.2$		4.219×10^{11}	116.25 dB
Receiver Gain efficiency g_R		1	0 dB
Polarization Loss L_{pol}		0.933	-0.3 dB
Rx. pointing efficiency η_{RP}		1	0 dB
NBF transmission efficiency η_λ		0.7	-1.54 dB
Rx. efficiency η_{Rx}		0.7	-1.54 dB
Received Signal, P_{Rx}		7.38×10^{-11}W	-77.3 dBm

Link power budget equation parameters from Psyche DSOC uplink.

Appendix II: Code

```
% Read MODIS file with MATLAB.
% Marc Casanovas
%
% This example code illustrates how to access and visualize LAADS
% MOD08_M3 v6 HDF-EOS2 Grid file in MATLAB.

% Tested under: MATLAB R2020b
% Last updated: 2021-06-14

clc; clear all;

import matlab.io.hdfeos.*
import matlab.io.hdf4.*

currentFolder = pwd;
year=2000:2020;

DATA_ANNUAL_MEAN = zeros(180, 360);
TWO_DECADES_DATA_MEAN= zeros(180, 360);

for count=1:length(year)

%Use your own adress...
adress=sprintf('%s\\DATA_BASE\\MODIS_MOD08_M3\\%g',currentFolder,year(count));
Files=dir(adress);
for i=1:(length(Files)-2)
    Files(i).name= Files(i+2).name;
end


for i=1:length(Files)

% Read data field
FILE_NAME= Files(i).name;
GRID_NAME='mod08';
FileAdress=sprintf('%s\\%s',adress,FILE_NAME);
%%

fullFileName = fullfile(adress, Files(1).name);
if exist(fullFileName)
  % Opening the HDF-EOS2 Grid File
    file_id = gd.open(FileAdress,'rdonly');
else
  % File does not exist.
  warningMessage = sprintf('%s does not exist', fullFileName);
  uiwait(warndlg(warningMessage));
end

```

```
% Open Grid
grid_id = gd.attach(file_id, GRID_NAME);

% Define the Data Field...
%DATAFIELD_NAME='Cloud_Fraction_Mean_Mean';
DATAFIELD_NAME= 'Deep_Blue_Aerosol_Optical_Depth_550_Land_Mean_Mean';
%DATAFIELD_NAME='AOD_550_Dark_Target_Deep_Blue_Combined_Mean_Mean';
%DATAFIELD_NAME='Aerosol_Optical_Depth_Land_Mean_Mean';
%DATAFIELD_NAME='Cloud_Top_Height_Mean_Mean';
%DATAFIELD_NAME='Cloud_Optical_Thickness_Combined_Mean_Mean';

% Read the dataset.
data(i).mat = gd.readField(grid_id, DATAFIELD_NAME);

% Read lat and lon dataset.
lon = gd.readField(grid_id, 'XDim', [], [], []);
lat = gd.readField(grid_id, 'YDim', [], [], []);

% Detach Grid object.
gd.detach(grid_id);
gd.close(file_id);

% Transpose the data to match the map projection.

data(i).mat=data(i).mat(:,:,1)'; %.mat';

% Convert the data to double type for plot.
data(i).mat=double(data(i).mat);
lon=double(lon);
lat=double(lat);

% Read attributes from the data field.
SD_id = sd.start(FileAdress, 'rdonly');
sds_index = sd.nameToIndex(SD_id, DATAFIELD_NAME);
sds_id = sd.select(SD_id, sds_index);

% Read _FillValue from data field.
fillvalue_index = sd.findAttr(sds_id, '_FillValue');
fillvalue = sd.readAttr(sds_id, fillvalue_index);

% Get the long name from data field.
long_name_index = sd.findAttr(sds_id, 'long_name');
long_name = sd.readAttr(sds_id, long_name_index);

% Read units from the data field.
units_index = sd.findAttr(sds_id, 'units');
units = sd.readAttr(sds_id, units_index);

% Read scale_factor from the data field.
scale_index = sd.findAttr(sds_id, 'scale_factor');
scale = sd.readAttr(sds_id, scale_index);
scale = double(scale);
```

```
101
102 % Read add_offset from the data field.
103 offset_index = sd.findAttr(sds_id, 'add_offset');
104 offset = sd.readAttr(sds_id, offset_index);
105 offset = double(offset);
106
107 % Read valid_range from the data field.
108 range_index = sd.findAttr(sds_id, 'valid_range');
109 range = sd.readAttr(sds_id, range_index);
110
111 % Terminate access to the corresponding data set.
112 sd.endAccess(sds_id);
113
114 % Close the file.
115 sd.close(SD_id);
116
117 % Replace the filled value with NaN.
118 data(i).mat((data(i).mat)==fillvalue) = NaN;
119 data(i).mat(data(i).mat > double(range(2)))= NaN;
120 data(i).mat(data(i).mat < double(range(1))) = NaN;
121
122 % Multiply scale and add offset, the equation is scale *(data-offset).
123 data(i).mat = scale*(data(i).mat-offset);
124
125 end
126
127 % Mean of all monthly data into a year:
128 for k=1:length(data)
129  DATA_ANNUAL_MEAN = DATA_ANNUAL_MEAN  + data(k).mat;
130 end
131 SecondAdress=sprintf('%s\\DATA_BASE\\MODIS_MOD08_M3\\AnnualMeans\\',...
132 currentFolder);
133 DataName= sprintf('%sDATA_ANNUAL_MEAN_%g.mat',SecondAdress,year(count));
134 DATA_ANNUAL_MEAN=DATA_ANNUAL_MEAN/length(data);
135 save(DataName,'DATA_ANNUAL_MEAN');
136
137 % Mean of 2000-2020 years:
138 TWO_DECADES_DATA_MEAN= TWO_DECADES_DATA_MEAN + DATA_ANNUAL_MEAN;
139
140 end
141
142 TWO_DECADES_DATA_MEAN= TWO_DECADES_DATA_MEAN/length(year);
143
144 figure()
145 h1 = axes;
146 imagesc(lon,lat,TWO_DECADES_DATA_MEAN);
147 TWO_DECADES_DATA_MEAN(isnan(TWO_DECADES_DATA_MEAN))=0;
148 myColorMap = jet(256);
149 myColorMap(1,:) = 1;
150 colormap(myColorMap);
151 shading(gca,'interp')
152
```

```
set(h1, 'Ydir', 'normal')
hold on
load coastlines
c=colorbar();
xlabel('Longitude [  ]')
ylabel('Latitude [  ]')
LabelText = 'AOD';
ylabel(c,LabelText);

% Set Tick Marks
set(gca,'XTick',-180:40:180);
set(gca,'YTick',-90:20:90);
plot(coastlon,coastlat,'k','linewidth',2)

%Configure figures to latex.
%addpath('./DATA_BASE/matlab2tikz/src/');
%matlab2tikz('WORLD_AEROSOL_MEAN_2000_2020.tex','width','\figW','height',...
'\figH');
```

```
%% Mispointing losses
%Marc Casanovas
%June 2021
clc; clear all
%% inputs

%Minimum allowed misspointing loss [dB]
min_loss=2;

%Transmitter antenna diameter [m]
D=0.22;

%Wavelength [m]
lambda=1550e-9;

%obscuration ratio[-]
gamma=0:0.1:0.4;

%Adimensional parameter: X=k*a*sin(Theta) [-]
X=linspace(-20,20,1000);

%Pointing angle [rad]
theta=asin(lambda*X/(D*pi));

%                f0         f2             f4           f6
coef_matrix  =  [0.569797 -0.113420  0.0503535 -0.0292921;   %gamma=0
                 0.566373 -0.1153270 0.0513655 -0.0299359;   %gamma=0.1
                 0.555645 -0.1204570 0.0542465 -0.0317773;   %gamma=0.2
                 0.535571 -0.1269920 0.0584271 -0.0344978;   %gamma=0.3
                 0.50138  -0.1317770 0.0626752 -0.0374276 ]; %gamma=0.4

%%
```

```
for i=1:length(gamma)

   %aperture to beamwidth ratio
   alpha_opt=1.12 -1.30*gamma(i)^2 + 2.12*gamma(i)^4;
   syms u
    for j=1:length(X)
        fun = @(u)(exp(-u*alpha_opt^2)).*besselj(0, X(j)*sqrt(u));
        inte = integral(fun, gamma(i)^2, 1);
        gT(i,j)=10*log10(2*alpha_opt^2*(inte)^2);

    end
end

pointing_error=abs(find_pointing_error(gT,theta,min_loss));
variance=abs(0.25*pointing_error);
mean=abs(0.25*pointing_error);

scope=0:1e-8:4e-6;
for i=1:length(scope)
    %Rice distribution
    pdf(i)= (scope(i)/ variance^2)*exp(-0.5 * (scope(i)^2 + mean^2)/ ...
        variance^2)*...
         besseli(0, scope(i)*mean/ variance^2);
         % besseli(0, ...) is the zeroth order modified Bessel function of
         % the first kind.
end

%Probability induced fade (PIF)
func_1= @(x)(x./ variance^2).*exp(-0.5 * (x.^2 + mean^2)/ variance^2).*...
       besseli(0, x.*mean/ variance^2);
PIF= integral(func_1, pointing_error, 100e-6);


for i=1:length(gamma)
    %Coefficiens for gamma=0 ("Psyche study")
    f0=coef_matrix(i,1);
    f2=coef_matrix(i,2);
    f4=coef_matrix(i,3);
    f6=coef_matrix(i,4);

    %Instantaneous pointing loss
    func_2= @(x) ((1/f0^2)*(f0 +  ...
        ((f2*(pi*(D/lambda)*x).^2)/factorial(2))  + ...
        ((f4*(pi*(D/lambda)*x).^4)/factorial(4))...
            + ((f6*(pi*(D/lambda)*x).^6)/factorial(6)) ).^2 ) .*...
            (x./ variance^2).*exp(-0.5 * (x.^2 + mean^2)/ variance^2).*...
           besseli(0, x.*mean/ variance^2);

    %Transmitter efficiency
    eff_Tx(i)= integral(func_2, 0, 200e-6);
end

```

```
82
83  %% PLOTS
84
85  %(1)
86  figure()
87  %Off-Gain axis plot
88  G=(pi*D/lambda)^2;
89  Gdb=10*log10(G);
90  plot(theta,gT(1,:)+Gdb);
91  hold on
92  %plot(theta, gT(2,:));
93  plot(theta, gT(3,:)+Gdb);
94  %plot(theta, gT(4,:));
95  plot(theta, gT(5,:)+Gdb);
96  axis([min(theta) max(theta) 0 max(Gdb)])
97
98  grid minor
99  title('Off-axis Gain')
100 ylabel(' Off-axis Gain [dB]')
101 xlabel('Off-axis angle \theta_1 [rad]')
102 legend('\gamma=0','\gamma=0.2','\gamma=0.4')
103
104 %(2)
105 figure()
106
107 %Mispointing loss
108 plot(theta,gT(1,:)- max(gT(1,:))  );
109 hold on
110 %plot(theta, gT(2,:));
111 plot(theta, gT(3,:)- max(gT(3,:)));
112 %plot(theta, gT(4,:));
113 plot(theta, gT(5,:)- max(gT(5,:)));
114
115 grid minor
116 title('Mispointing Loss')
117 ylabel('Mispointing loss [dB]')
118 xlabel('Off-axis angle \theta_1 [rad]')
119 axis([0 4.5e-6 -3 0])
120
121 %(3)
122
123 figure()
124 plot(scope,pdf)
125 grid minor
126 title('Probability density function (PDF)')
127 ylabel(' Probability density [-]')
128 xlabel('Mispointing angle \theta_1 [rad]')
```

```
1  function[pointing_error]=find_pointing_error(gT,theta,min_loss)
2  %% FUNCTION: finding_pointing_error()
3  % Marc Casanovas
```

```
% June 2021
%
% This function returns the frontier pointing angle that causes
% a  fading loss equal to the maximum  assumable  pointing loss
% predetermined  by the user.
%
% Inputs:
%  - gT(i,:): (float) Gain efficiency Factor [dB].
%     i=1 --> Obscuration ratio = 0
%     i=2 --> Obscuration ratio = 0.1
%     i=3 --> Obscuration ratio = 0.2
%     i=4 --> Obscuration ratio = 0.3
%     i=5 --> Obscuration ratio = 0.4
%
%  - theta: (float array) mispointing angle [rad]
%  - min_loss: (float) maximum assumable system pointing loss [dB].
%
% Output:
%  - pointing_error (float) mispointing error angle [rad].
%
    mis_loss_vec=gT(1,:)- max(gT(1,:)); % NOTE: Obscuration ratio = 0.
    min_loss=abs(min_loss);
    value=min( abs( mis_loss_vec + min_loss ) );
    find=false;
    counter=1;

    while( counter<=length(mis_loss_vec)  && ~find)
        if( (mis_loss_vec(counter)<=-min_loss-value+1e-4) && ...
            (mis_loss_vec(counter)>=-min_loss-value-1e-4) )
         find=true;
        end
        counter=counter+1;
    end
    pointing_error=theta(counter-1);

end
```

```
%Scinitillation and turbulence loss Andrew's Model
%Marc Casanovas
%June 2021

clc; clear all;

%% Inputs
%wavelength
lambda= [0.67, 1.064, 1.55]; %[micrometers]

%Zenit angle
zenit_angle= deg2rad(0:1:70); %[rad]

%Satellite height
```

```
H=2000000;%[m]

%Transmiter/Receiver height
h0=0; %[m]

%Threshold probability
p_thr=1e-5;%[-]

%Transmiter/Receiver diameter
D=5; %[m]

%% H-V 5/7 Model
w=21; %Wind Velocity [m/s]
A= 1.7e-14; %m^(-2/3)
func_0= @(h) (0.00594*(w/27)^2)*((h*10^(-5)).^10).*(exp(-h/1000)) + ( ...
    (2.7*10^(-16))*(exp(-h/1500)) ) + ( A*exp(-h/100) );
func_1= @(h) (0.00594*(w/27)^2)*((h*10^(-5)).^10).*(exp(-h/1000)) + ( ...
    (2.7*10^(-16))*(exp(-h/1500)) ) + ( A*exp(-h/100) ).* (h-h0./H-h0).^(5/6);
func_2= @(h) (0.00594*(w/27)^2)*((h*10^(-5)).^10).*(exp(-h/1000)) + ( ...
    (2.7*10^(-16))*(exp(-h/1500)) ) + ( A*exp(-h/100) ).* (h-h0).^(2);
func_3= @(h) (0.00594*(w/27)^2)*((h*10^(-5)).^10).*(exp(-h/1000)) + ( ...
    (2.7*10^(-16))*(exp(-h/1500)) ) + ( A*exp(-h/100) ).* (h-h0).^(5/6);

%Moments
mu_0= integral(func_0, h0, H);
mu_1= integral(func_1, h0, H);
mu_2= integral(func_1, h0, H);
mu_3= integral(func_1, h0, H);
mu_4=mu_1*mu_3;

%Turbulence scale height
hs=(mu_2/mu_3)^(6/7);

for index=1:length(lambda)

    % wavenumber
    k= (2*pi)/lambda(index); %[rad/m]

    for i=1:length(zenit_angle)

        sigma_1(i,index)=2.25*mu_1*(k^(7/6))*((H-h0)^(5/6))*...
        (sec(zenit_angle(i))^(11/6));

        T1(i,index)= ...
            (0.49*sigma_1(i,index))/(1+1.11*sigma_1(i,index)^6/5)^7/6;
        T2(i,index)= ...
            (0.51*sigma_1(i,index))/(1+0.69*sigma_1(i,index)^6/5)^5/6;
        T3(i,index)= T1(i,index)+ T2(i,index);

        %Scintillation index [-]
        sigma_scint(i,index)= 10^(2.5)*(exp(T3(i,index)) - 1);

```

```
61          %Aperture Averaging [-]
62          AA(i,index)=(1+ ...
                1.11*(D^2/(lambda(index)*hs*cos(zenit_angle(i))))^(7/6) )^(-1);
63
64          %Power scintillation index [-]
65          sigma_P(i,index)=AA(i,index)*sigma_scint(i,index);
66
67          %Turbulence Loss [dB]
68          L_turb(i,index)= ...
                4.343*(erfinv(2*p_thr-1)*sqrt(2*log(sigma_P(i,index)+1)) ...
                -0.5*log(sigma_P(i,index)+1));
69
70      end
71
72  end
73
74  %% PLOTS
75  plot(rad2deg(zenit_angle), L_turb(:,1) )
76  hold on
77  plot(rad2deg(zenit_angle), L_turb(:,2) )
78  plot(rad2deg(zenit_angle), L_turb(:,3) )
79  grid minor
80
81  xlabel('zenit angle ($\varphi$) [deg]', 'Interpreter','latex')
82  ylabel('L_{turb} [dB]')
83  legend("\lambda=670nm (Dye: Ti:sapphire)", "\lambda = 1064 nm (Solid: Nd: ...
        YAG)"...
84       ,"\lambda = 1550 nm (SemiConductor:  InGaAsP)")
```

```
1  % Define the meta-kernel
2  METAKR = {'https://naif.jpl.nasa.gov/pub/naif/CASSINI/kernels/lsk/
3  naif0012.tls','naif0012.tls',...
4  'https://naif.jpl.nasa.gov/pub/naif/MSL/kernels/fk/msl.tf','msl.tf',...
5  'https://naif.jpl.nasa.gov/pub/naif/generic_kernels/pck/
6  earth_720101_070426.bpc','earth_720101_070426.bpc',...
7  'https://naif.jpl.nasa.gov/pub/naif/generic_kernels/pck/
8  earth_200101_990628_predict.bpc','earth_200101_990628_predict.bpc',...
9  'https://naif.jpl.nasa.gov/pub/naif/generic_kernels/fk/stations/
10 earth_topo_201023.tf','earth_topo_201023.tf',...
11 'https://naif.jpl.nasa.gov/pub/naif/generic_kernels/pck/
12 earth_latest_high_prec.bpc','earth_latest_high_prec.bpc',...
13 'https://naif.jpl.nasa.gov/pub/naif/generic_kernels/pck/
14 earth_fixed.tf','earth_fixed.tf',...
15 'https://naif.jpl.nasa.gov/pub/naif/MSL/kernels/spk/
16 de425s.bsp','de425s.bsp',...
17 'https://naif.jpl.nasa.gov/pub/naif/MSL/kernels/spk/
18 mar085s.bsp','mar085s.bsp',...
19 'https://naif.jpl.nasa.gov/pub/naif/PSYCHE/kernels/pck/pck00010.tpc',...
20 'https://naif.jpl.nasa.gov/pub/naif/PSYCHE/kernels/spk/de421.bsp', ...
       'de440s.bsp',...
21 'https://naif.jpl.nasa.gov/pub/naif/PSYCHE/kernels/spk/psyche_v01.bsp'
```

```
};
```

```
%% EARTH-MARS ASTRODYNAMICS PARAMETERS

%Marc Casanovas
%June 2021

% Plot Earth and Mars position during 8 years days from 2022-01-01
clc;
close all;
clear all;

addpath('../RESSlib'); % Robotic Exploration of the Solar System lib

% List of the kernels URL:
input_kernels;

initSPICEv(fullK(METAKR)); % Init SPICE and load the kernels, if needed

% time interval
TW_str(1,:) = '2022 AUG 22 00:00:00'; TW_str(2,:) = '2024 AUG 03 00:00:00';
TW = cspice_wninsd(cspice_str2et(TW_str(1,:)),cspice_str2et(TW_str(2,:)));

et0 = cspice_str2et ( TW_str(1,:) ); % Call SPICE to convert it to ET
Nintervals = 200;
et= linspace(TW(1),TW(2),Nintervals); % Vector of instants
frame = 'ECLIPJ2000'; % Referece frames
abcorr = 'NONE'; % No corrections
%observer = '3'; % Earth System barycenter
%observer = '4'; % Earth System barycenter
observer = '0'; % Solar System barycenter Try this
[dearth,~] = cspice_spkezr('399',et,frame,abcorr,observer); % Earth state ...
    (km,km/s)
[dmars,~] = cspice_spkezr('499',et,frame,abcorr,observer); % Mars state ...
    (km,km/s)

%Uncomment this line for the Psyche study, and comment the line loctated
%above.

%[dmars,~] = cspice_spkezr('PSYCHE',et,frame,abcorr,observer); % Psyche ...
    state (km,km/s)


%% EARTH - MARS DISTANCE, ANGLES AND RELATIVE VELOCITY
d1=dmars(1,:)+dearth(1,:); %Position x-component of dearth-dmars vector
d2=dmars(2,:)+dearth(2,:); %Position y-component of dearth-dmars vector
d3=dmars(3,:)+dearth(3,:); %Position z-component of dearth-dmars vector

v1=dearth(4,:)+dmars(4,:); %Velocity x-component of dearth-dmars vector
v2=dearth(5,:)+dmars(5,:); %Velocity y-component of dearth-dmars vector
v3=dearth(6,:)+dmars(6,:); %Velocity z-component of dearth-dmars vector
```

```
47
48 dEminusdM_vec=[d1; d2;d3]';    %dearth-dmars vector
49
50 dearth_trans=dearth';
51 dmars_trans=dmars';
52 Dist_earth_vec=dearth_trans(:,1:3);
53 Dist_mars_vec=dmars_trans(:,1:3);
54
55  for i=1:length(dEminusdM_vec)
56
57   E_M_dist(i,:)= norm(dEminusdM_vec(i,:));  %Earth-Mars distance
58   E_dist(i,:)=norm(Dist_mars_vec(i,:));     %Earth-sun distance
59   M_dist(i,:)=norm(Dist_mars_vec(i,:));     %Mars sun distance
60
61   %SEP SOLAR-EARTH-PROBE ANGLE
62   SEP_angle(i,:)=atan2(norm(cross(dEminusdM_vec(i,:),
63   Dist_earth_vec(i,:))), dot(dEminusdM_vec(i,:),Dist_earth_vec(i,:)));
64
65   %SPE SOLAR-PROBE-EARTH- ANGLE
66   SPE_angle(i,:)=atan2(norm(cross(dEminusdM_vec(i,:),Dist_mars_vec(i,:))), ...
       dot(dEminusdM_vec(i,:),Dist_mars_vec(i,:)));
67  end
68
69  %Earth-Mars distance in UA (1UA = 1.496e8 km)
70  E_M_dist=E_M_dist/1.496e8;
71
72  %SEP angle in deg
73  SEP_angle=SEP_angle*(360/(2*pi));
74
75  %SPE angle in deg
76  SPE_angle=SPE_angle*(360/(2*pi));
77
78  %time=cspice_etcal( et );
79  etplot= linspace(TW(1),TW(2),10);
80  etstr  = ...
       string(datetime(etplot,'convertfrom','epochtime','Epoch','01-Jan-2000 ...
       11:58:55.816','Format','yyyy-MM-dd'));
81
82  %% PLOTS
83
84 % 1- Earth-Mars distance plot
85 figure()
86 subplot(2,1,1);
87 plot(et, E_M_dist,'b','linewidth',2)
88 hold on; box on; grid minor;
89 xlim([TW(1) TW(2)])
90 ylim([0 3])
91 xticks(etplot)
92 xticklabels(etstr)
93 xtickangle(20)
94 %set(gca,'YTick',0.5:1:3)
95 %set(gca,'YTickLabel',0.5:1:3)
```

```
96  ylabel('Range [AU]')
97  set(gca,'FontSize',10)
98
99
100 % 2 - SEP & SPE angles
101 %figure()
102 subplot(2,1,2);
103 plot(et,SEP_angle,'b','linewidth',2)
104 hold on; box on; grid minor;
105 plot(et,SPE_angle,'r','linewidth',2)
106 xlim([TW(1) TW(2)])
107 xticks(etplot)
108 xticklabels(etstr)
109 xtickangle(45)
110 set(gca,'FontSize',10)
111 ylabel('Sun angle [deg]')
112 legend({'SEP','SPE'});
113
114
115 %3 - Earth-Mars trajectory
116 figure()
117 plot3(dearth(1,:),dearth(2,:),dearth(3,:),'r') % Do the plot
118 hold on
119 plot3(dmars(1,:),dmars(2,:),dmars(3,:),'g')
120 axis tight
121 axis('equal');
122 set(findall(gcf,'-property','FontSize'),'FontSize',12)
123 xlabel('km');
124 ylabel('km');
125 zlabel('km');
126 title('Planet trajectory from solar system barycenter')
127 legend({'Earth','Mars'});
128
129 % 4 - Radial, transverseal and total velocity
130
131 figure()
132 Mars_norm_vel=sqrt(dmars(4,:).^2+ dmars(5,:).^2+dmars(6,:).^2);
133 Earth_norm_vel=sqrt(dearth(4,:).^2 + dearth(5,:).^2+dearth(6,:).^2);
134 Difference_norm = Mars_norm_vel-Earth_norm_vel;
135 plot(et,Difference_norm)
136 xlim([TW(1) TW(2)])
137 hold on
138 plot(et,v1)
139 plot(et,v2)
140 xticks(etplot)
141 xticklabels(etstr)
142 xtickangle(45)
143 set(gca,'FontSize',10)
144 ylabel('Velocity [km/s]')
145 legend({'Orbital','Transverse','Radial'});
146 grid minor
147
```

```
% 5 - point ahead angle
figure()
c=  299792.458; %[km/s]
%Pointing ahead-angle
PA=2*abs(v1)/c; %[rad]
plot(et,PA)
xlim([TW(1) TW(2)])
xticks(etplot)
xticklabels(etstr)
xtickangle(45)
set(gca,'FontSize',10)
ylabel('Point Ahead angle \Theta [rad]')
grid minor


% 6 - Doppler
figure()
%light speed
%transmiter wavelength
lambda=1064e-9; %[m]
%frecuency
f=c/lambda;%[HZ]
%Wavelength shift
delta_lambda= lambda*v2/c; %[rad]
plot(et,delta_lambda)
xlim([TW(1) TW(2)])
xticks(etplot)
xticklabels(etstr)
xtickangle(45)
set(gca,'FontSize',10)
ylabel('\Delta \lambda_d [m]')
grid minor


endSPICE; % Unload the kernels
```

LINK BUDGET			
	lineal	Db	
Prx [W]	4	6.02059991	
Gtx	8.11E+11	119.090162	
gr	0.814	-0.89375595	
SL	0.673	-1.71984936	
eta_tx	0.7	-1.5490196	
eta_tp	0.9214	-0.35551792	
Ltrans	0.95	-0.22276395	
Lturb	0.845	-0.73143291	-0.95419686
Grx	2.18E+14	143.383565	
gr	0.96	-0.17728767	
Lpol	0.933	-0.30118356	
eta_rp	1	0	
eta_lambda	0.7	-1.5490196	
eta_rx	0.7	-1.5490196	
	8.80132E+25		

Dtx[m]	0.305							
Drx [m]	5							
R (AU)	0.3	0.6	1	1.3	1.6	2	2.3	2.7
Space Loss	3.56E-36	8.90E-37	3.20E-37	1.90E-37	1.25E-37	8.01E-38	6.06E-38	4.39E-38
R (m)	4.49E+10	8.98E+10	1.50E+11	1.94E+11	2.39E+11	2.99E+11	3.44E+11	4.04E+11
wavelength [m]	1.06E-06							
Space Loss(dB)	-3.54E+02	-3.61E+02	-3.65E+02	-3.67E+02	-3.69E+02	-3.71E+02	-3.72E+02	-3.74E+02
Gtx	8.11E+11							
Grx	2.18E+14							
obsc. Ratio	0.2							

R [AU]	Prx (lineal)	Prx(dB)	margin	Prmin(dB)	Prmin(lineal)
0	inf	-	-	-	-
0.3	3.55E-07	-6.45E+01	-6.5	-7.10E+01	7.94E-08
0.6	8.87E-08	-7.05E+01	-6	-7.65E+01	2.23E-08
1	3.19E-08	-7.50E+01	-6	-8.10E+01	8.02E-09
1.3	1.89E-08	-7.72E+01	-6	-8.32E+01	4.75E-09
1.6	1.25E-08	-7.90E+01	-6	-8.50E+01	3.13E-09
2	7.98E-09	-8.10E+01	-6	-8.70E+01	2.01E-09
2.3	6.04E-09	-8.22E+01	-6	-8.82E+01	1.52E-09
2.7	4.38E-09	-8.36E+01	-6	-8.96E+01	1.10E-09

Link equation excel sheet.

```
%NOISE-SIGNAL FLUX and CAPACITY STUDY
%June 2021
%Marc Casanovas
clc;clear all;

%% Inputs
%Rx antenna diameter
D_rx=5; %m

```

```
%obscuration ratio
gamma=0.2;


%Range in [AU]
R=[0.3, 0.6, 1, 1.3, 1.6,  2, 2.3, 2.7];

%Received and detected Received signal (Values from Link equation "Excel ...
    sheet"))
Prx=[2.66E-10, 6.66E-11, 2.40E-11, 1.42E-11, 9.36E-12, 5.99E-12, ...
    4.53E-12, 3.29E-12]; %W
Ps= [6.69E-11, 1.67E-11, 6.02E-12, 3.56E-12, 2.35E-12, 1.50E-12, ...
    1.14E-12, 8.26E-13]; %W

%Wavelength
lambda= 1064e-9;%m

%Planck constant
h=6.62607015e-34; %J*s

%Speed of light
c=299792458; %m/s

%Receiver efficiency lineal
eta_rx=0.65;

%Receiver efficiency dB
eta_rx_dB=10*log10(eta_rx);

%Polarization loss dB
L_pol_dB= -0.3; %dB

%Narrow band filter efficiency
eta_nbf=0.6; %[-]

%Narrow band filter bandwidth

delta_nbf= 2.5; %Amstrong

%Quantum detector efficiency
eta_det=0.6; %[-]

%Solar flux at 1UA @1064nm
H=0.0669; %W*m^-2*Amstrong^-1;

%Distance Mars Sun
R_mars_sun= 1.52359; %UA

%Mars radius
R_mars=3389.5;%km

%Mars albedo
```

```
alb=0.25;

%Atmosphere losses
L_atm=0.80275;

%SEP angle
SEP=3; %[deg]

%Dark noise
n_dark=1000; %[photons/s]

%Field of view
FOV= 0.5e-6; %rad

%% Equation parameters
%Modified receiver efficiency
eta_rx_ast_dB= eta_rx_dB + L_pol_dB + 3; %dB
eta_rx_ast=10^(eta_rx_ast_dB/10);

%Effective Area
Aeff= (pi*D_rx^2)/4; %m^2

%Solid angle
Omega=(pi*FOV^2)/4; %sr

%Radiance "L(lambda)" @ 1064nm
Radiance_Modtran=0.0065; %W*m^-2*Amstrong^-1*sr^1;

%Rx Gain efficiency factor
gr=1-gamma^2;

%Correction Factor
F=0.0003*SEP^2 -0.0275*SEP + 1.1846;

for i=1:length(Ps)
    %% Photon signal and noise fluxes
    %Received signal flux (photons/s)
    lambda_s(i)= Prx(i)*(lambda/(h*c));

    %Background noise sources:

    %1.Extended noise flux

    %Background noise extended power
    Pb_ext = eta_rx_ast*Aeff*gr*Omega*delta_nbf
    *Radiance_Modtran*eta_nbf*eta_det; %[W]
    %Extended flux
    lambda_ext= Pb_ext*(lambda/(h*c)); %[photons/s]

    %2.Point noise flux
    %Earth-Mars distance
    Z(i)=R(i)*1.496e8; %km
```

```
111
112     %Irradiance from Mars incident to Earth
113     I(i)=(H/(R_mars_sun^2))*((R_mars/Z(i))^2);
114
115     %Background point noise power
116     Pb_Mars(i)=eta_rx_ast*Aeff*gr*delta_nbf
117     *I(i)*alb*F*L_atm*eta_nbf*eta_det; %[W]
118
119     %Point flux
120     lambda_point(i)=Pb_Mars(i)*(lambda/(h*c)); %[photons/s]
121
122     %Total background flux
123     lambda_b(i)=lambda_ext+lambda_point(i);%[photons/s]
124
125
126     %% Capacity
127
128     Pn(i)=lambda_b(i)*h*c/lambda;%W
129     M=8;
130     E= h*c/lambda;
131     tau_s=1e-9;%s
132
133     A1(i)= Ps(i)*(1/log(M));
134     A2(i)= Pn(i)*( 2/(M-1) );
135     A3(i)= Ps(i)^2*((M*tau_s)/(log(M)*E));
136     AT(i)=A1(i)+A2(i)+A3(i);
137     C_nasa(i)= (1/(log(2)*E))*(  Ps(i)^2/AT(i) );
138
139 end
140
141 %% PLOT
142 semilogy(R, C_nasa/10^6)
143 grid minor
144 ylabel('Capacity [Mbits/s]')
145 xlabel('Range [AU]')
```